Nanocrystals of lead chalcohalides : a series of kinetically trapped metastable nanostructures

Nanocrystals of Lead Chalcohalides: A Series of Kinetically Trapped Metastable Nanostructures

Stefano Toso[†,Δ,▽], Quinten A. Akkerman[†,Φ,▽], Beatriz Martín-García[†,Γ,▽], Mirko Prato[Σ], Juliette Zito[†], Ivan Infante[†,§,*], Zhiya Dang[†,Θ], Anna Moliterni[‡,*], Cinzia Giannini[‡], Eva Bladt[⧖,┼], Ivan Lobato[⧖,┼], Julien Ramade[⧖,┼], Sara Bals[⧖,┼,*], Joka Buha[†], Davide Spirito[†,ϟ], Enrico Mugnaioli[⊥], Mauro Gemmi[⊥,*], Liberato Manna[†,*]

[†] Department of Nanochemistry, [Σ] Materials Characterization Facility, Istituto Italiano di Tecnologia, Via Morego 30, 16163 Genova, Italy

[Δ] Dipartimento di Matematica e Fisica and Interdisciplinary Laboratories for Advanced Materials Physics, Università Cattolica del Sacro Cuore, via Musei 41, I-25121 Brescia, Italy

[§] Department of Theoretical Chemistry, Faculty of Science, Vrije Universiteit Amsterdam, de Boelelaan 1083, 1081 HV Amsterdam, The Netherlands

[‡] Istituto di Cristallografia - Consiglio Nazionale delle Ricerche (IC-CNR), via Amendola 122/O, I-70126 Bari, Italy

[⧖] Electron Microscopy for Materials Science (EMAT), University of Antwerp, Groenenborgerlaan 171, 2020 Antwerp, Belgium

[┼] NANOlab Center of Excellence, University of Antwerp, Belgium

[⊥] Center for Nanotechnology Innovation@NEST, Istituto Italiano di Tecnologia, Piazza San Silvestro, 12, 56127, Pisa, Italy

Supporting Information Placeholder

ABSTRACT: We report the colloidal synthesis of a series of surfactant-stabilized lead chalcohalide nanocrystals. Our work is mainly focused on $Pb_4S_3Br_2$, a chalco-halide phase unknown to date that does not belong to the ambient-pressure PbS – $PbBr_2$ phase diagram. The $Pb_4S_3Br_2$ nanocrystals herein feature a remarkably narrow size distribution (with a size dispersion as low as 5%) a good size tunability (from 7 to ~30 nm), an indirect bandgap, photoconductivity (responsivity = 4 ± 1 mA/W) and stability for months under air. A crystal structure is proposed for this new material by combining the information from 3D electron diffraction and electron tomography of a single nanocrystal, X-Ray powder diffraction and density functional theory calculations. Such a structure is closely related to that of the recently discovered high-pressure chalcohalide $Pb_4S_3I_2$ phase, and indeed we were able to extend our synthesis scheme to $Pb_4S_3I_2$ colloidal nanocrystals, whose structure matches the one that has been published for the bulk. Finally, we could also prepare nanocrystals of $Pb_3S_2Cl_2$, which proved to be a structural analogue of the recently reported bulk $Pb_3Se_2Br_2$ phase. It is remarkable that one high-pressure structure (for $Pb_4S_3I_2$) and two metastable structures that had not yet been reported (for $Pb_4S_3Br_2$ and $Pb_3S_2Cl_2$) can be prepared on the nanoscale by wet-chemical approaches. This highlights the important role of colloidal chemistry in the discovery of new materials and motivates further exploration into metal chalcohalides nanocrystals.

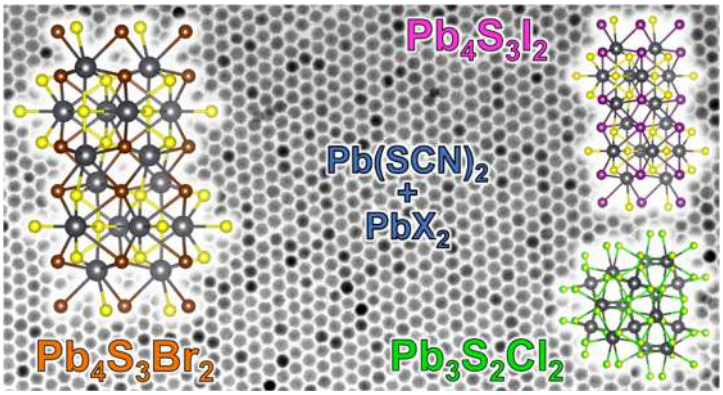

INTRODUCTION

Over the last decade, lead chalcogenides first and lead-halide perovskites later have been among the cornerstone materials in nanocrystal (NC) research.[1–3] Nowadays, many fundamental questions on these materials have been answered, and as interest in them is progressively shifting towards their applications, the quest for new a generation of inorganic NCs with appealing optoelectronic properties is becoming more compelling. An interesting class of compounds, which has hardly been explored on the nanoscale to date, is that of metal chalcohalides.[4–7] These materials offer a rich solid-state chemistry[8] and structural diversity,[9,10] and they have proven to be useful for applications ranging from solar energy conversion to thermoelectrics, hard radiation detection, and superconductivity.[11–14] Among them, lead chalcohalides have been investigated in the past,

up to the complete determination of the atmospheric pressure PbY–PbX_2 binary phase diagrams (Y = S, Se ; X = Cl, Br, I),[8] a search that led to the discovery and structural characterization of two stable ($Pb_5S_2I_6$ and $Pb_7S_2Br_{10}$) as well as some metastable chalco-halide structures (Pb_4SCl_6 and Pb_4SeBr_6).[15,16] For the PbS-$PbBr_2$ system, a few additional tentative stoichiometries have been identified.[16–19] In various works, different compositions such as $(PbBr)_2S$[17,18], "2PbS-$PbCl_2$" and "2PbS-$PbBr_2$"[16,19] have been reported and even partially characterized, with Rabenau *et al.* demonstrating that "2PbS-$PbBr_2$" thermally decomposes into a mixture of $Pb_7S_2Br_{10}$ and PbS.[16] However, in the case of those latter phases the crystal structures were not determined, therefore precluding further investigations and leaving the door open to the possibility of identifying new lead chalcohalides. Indeed, Ni *et. al.* recently synthesized in bulk two high-pressure phases, namely $Pb_4S_3I_2$ and $Pb_3Se_2Br_2$, by means of a high-pressure solid-state reaction.[20,21]

In our attempt to synthesize colloidal lead sulphobromide NCs, we have discovered a phase that has not yet been reported, namely $Pb_4S_3Br_2$. We could prepare NCs of this material, which were roughly spherical in shape and had narrow size distributions, with an average size that was tunable from 7 to ~30 nm. The NCs always exhibited an absorption onset at around 650 nm, which is compatible with the calculated bandgap of 1.98 eV (~630 nm). We have been able to propose a structural model for this new material, based on single NC 3-dimensional electron diffraction (3D-ED)[22–25] and on X-Ray powder diffraction (XRPD) data. Our findings were further supported by high angle annular dark field scanning transmission electron microscopy (HAADF-STEM) tomography of an individual NC. Density functional theory (DFT) calculations confirmed an indirect bandgap, which explains the absence of an excitonic peak in the experimental optical absorption spectrum.

The structure we propose for the $Pb_4S_3Br_2$ NCs shares close similarities with that of the recently published high-pressure (4 GPa) $Pb_4S_3I_2$ phase, [21] featuring the same space group and a comparable atomic layout. Differently from lead halide perovskites, and more akin to the case of lead chalcogenides, our $Pb_4S_3Br_2$ NCs were colloidally stable under air and at room temperature for at least 2 months, a time span during which they did not undergo any structural, compositional or optical changes. On the other hand, they thermally decomposed at temperatures above ~250°C, by forming a mixture of the thermodynamically stable PbS and $Pb_7S_2Br_{10}$, which is consistent with what already reported for other phases in the PbS-$PbBr_2$ system.[16] We also tested our $Pb_4S_3Br_2$ NCs in photodetectors and solar cells, proving that they are indeed capable of both photo-response and energy harvesting, even if with low efficiency in these initial attempts.

We could further extend our synthetic protocol to $Pb_4S_3I_2$ and $Pb_3S_2Cl_2$ NCs. The structure of the iodine-based NCs matches that of high-pressure bulk $Pb_4S_3I_2$.[21] The chloride-based NCs appear instead to be compatible with the stoichiometry and tentative X-ray pattern reported in 1969 by Rabenau *et. al.* for a phase called "2PbS + $PbCl_2$" which, according to their report, they could neither purify nor fully characterize.[16] Thanks to these clues, we discovered that the structure of our chlorine-based NCs closely resembles that of bulk $Pb_3Se_2Br_2$, recently reported by Ni *et. al.* as well,[20] and we were able to adapt it in order to Rietveld fit our XRPD data.

We point out that none of these structures ($Pb_3S_2Cl_2$, $Pb_4S_3Br_2$, $Pb_4S_3I_2$) belongs to the ambient-pressure PbS – PbX_2 phase diagrams.[16] Hence, we find it remarkable that a colloidal chemistry approach has enabled us to prepare stable NCs of an entirely new group of metastable structures which in the bulk were only obtained under high-pressure conditions ($Pb_4S_3I_2$), in traces ($Pb_3S_2Cl_2$), or that were never obtained at all to date ($Pb_4S_3Br_2$).

EXPERIMENTAL SECTION

Chemicals. Lead thiocyanate ($Pb(SCN)_2$, 99.5%), lead bromide ($PbBr_2$, ≥98%), lead iodide (PbI_2, 99%), lead chloride ($PbCl_2$, 98%), oleylamine (OLAM, 70%), oleic acid (OA, 90%), 1-octadecene (ODE, 90%), NH_4SCN (≥97.5%), $Zn(CH_3COO)_2{\cdot}2H_2O$ (≥99%), $Al(NO_3)_3{\cdot}9H_2O$ (≥98%), 1-Ethyl-3-methylimidazolium iodide (EMII, 97%), methanol (MeOH, anhydrous, 99.8%), ethanol (≥99.5%) and toluene (TOL, anhydrous, 99.8%) were purchased from Sigma-Aldrich. All chemicals were used without further purification (lead salts were stored under nitrogen).

Synthesis of $Pb_4S_3Br_2$ NCs. All the syntheses of $Pb_4S_3Br_2$ NCs were performed in air, without pre-drying chemicals or solvents, *via* a heat-up synthetic approach similar to the one developed by us for the synthesis of ultrathin PbS nanosheets.[26] Briefly, 0.2 mmol of $PbBr_2$ and 0.2 mmol of $Pb(SCN)_2$ where dissolved in a mixture of 10 mL ODE and 250 μL of OLAM and OA at 120°C in a 25 mL three-necked flask. Then, the solution was quickly heated (~20°C/min) and started turning from light-yellow to bloody red above 150°C while the NCs nucleated and grew. The reaction was quenched by cooling the flask in a water bath; size control was achieved by varying the maximum temperature reached before quenching. Additionally, the NCs could be grown further by dropwise addition of a solution of precursor over several hours at a constant temperature of 170°C, as described in the discussion. Depending on their size, the NCs were recovered by simple centrifugation or by ethyl-acetate assisted precipitation followed by centrifugation (6000 rpm for 5 min in both cases). Additional details on the synthesis are provided in the Supporting Information (SI, section S.a).

Synthesis of $Pb_4S_3I_2$ and $Pb_3S_2Cl_2$ NCs. The $Pb_4S_3I_2$ and $Pb_4S_2Cl_2$ NCs were prepared by adapting the synthetic protocol developed for $Pb_4S_3Br_2$. Simply, $PbBr_2$ was replaced with an equimolar amount of the desired lead halide. For the synthesis of $Pb_4S_3I_2$, since PbI_2 was more soluble than $PbBr_2$ in the reaction mixture, the synthesis could proceed as in the $Pb_4S_3Br_2$ NCs case without any further modification. However, a crystalline impurity, most likely PbI_2 nanosheets or flakes, formed together with $Pb_4S_3I_2$ NCs and could not be removed from the final product. For the synthesis of $Pb_3S_2Cl_2$, as $PbCl_2$ was less soluble than $PbBr_2$ in the reaction mixture, longer times were needed for the solubilization (up to 1h). We also performed a filtration with a 0.2 μm PTFE filter (Sartorius®) to remove any undissolved residual before performing the heat-up step. The product was often contaminated by large-size PbS NCs, which could be removed by simple centrifugation, while the smaller $Pb_3S_2Cl_2$ NCs remained suspended in the reaction batch and could be later recovered by ethyl-acetate assisted precipitation, as described for the $Pb_4S_3Br_2$ NCs case. Additional details on the syntheses are provided in the SI (sections S.c-d).

Preliminary characterization of the NCs. Absorption spectra from colloidal suspensions of NCs in toluene or hexane were

recorded using a Cary300 spectrophotometer. The absence of any photoluminescence (PL) in the VIS-IR region was probed using an Edinburgh FLS920 spectrofluorometer equipped with a Xe lamp and VIS-PMT (up to 850 nm) and NIR-PMTs detectors (liquid N_2 cooled housing, up to 1700 nm) by exciting at 400 – 450 – 500 nm. Low-magnification transmission electron microscopy (TEM) images were acquired on a JEOL JEM-1011 microscope equipped with a thermionic gun at an accelerating voltage of 100 kV. The samples were prepared by drop-casting diluted NC suspensions onto 200 mesh carbon-coated copper grids. High resolution high angle annular dark field scanning TEM (HAADF-STEM) images were acquired with a probe-corrected Thermo Fisher Titan microscope operating at 300 kV, with a semi-convergence angle of 20 mrad. Thermogravimetric analysis (TGA) was carried out on a TA Instruments TGA Q500 in inert atmosphere (N_2, 50 mL/min), first equilibrating the sample at 30°C for 5 min and then heating at a constant rate of 10 °C/min up to 900°C. Energy dispersive X-Ray spectroscopy (EDX) was performed on a JEOL JSM-6490LA scanning electron microscope (SEM). The NCs were washed in ethyl acetate to remove the excess of organics and unreacted precursors and drop-cast on a silicon wafer. TEM – energy dispersive X-ray spectroscopy (TEM-EDX) compositional analysis was performed on a Zeiss Libra TEM operating at 120 kV equipped with a Bruker XFlash6T-60 detector.

3D electron diffraction (3D-ED) experiments on individual NCs and *ab initio* structure solution. 3D-ED[22,23] data were collected on a Zeiss Libra TEM operating at 120 kV and equipped with a LaB_6 source. Data acquisitions were performed in STEM mode after defocusing the beam to achieve a parallel illumination of the sample. A beam size of about 150 nm in diameter was obtained by inserting a 5 μm C2 condenser aperture. An extremely mild illumination was adopted to avoid any alteration or amorphization of the sample and to slow down the accumulation of organic contaminants. 3D-ED data were recorded with an ASI Timepix detector,[27] which is able to register the arrival of single electrons and deliver a pattern that is virtually background-free. The camera length was 180 mm, with a theoretical resolution limit of 0.75 Å. 3D-ED data were taken from three roughly spherical NCs of ~30 nm in diameter and four platelet-shaped NCs with lateral sizes of ~30 × 80 nm. Both morphologies were found in the same synthetic batch (see details in the results and discussion section). 3D-ED data from the NCs were collected with a stationary electron beam, while the sample was tilted in fixed steps of 1° for a total range up to 115°. Diffraction data acquired when the electron beam was precessed were blurred and therefore were not suitable for the 3D reconstruction. 3D-ED data from nanoplatelets were instead collected with a precessing beam obtained by a Nanomegas DIGISTAR P1000 device, while the sample was tilted in fixed steps of 1° for a total range up to 70°.[28,29] The data were analyzed using ADT3D[30] and PETS[31] for cell and space group determination. The intensity integration for the structure determination was performed with PETS, using the standard integration and interpolation options. The *ab initio* structure solution was obtained using direct methods implemented in the software SIR2014.[32] Data were treated within the kinematical approximation: $I_{hkl} \propto F^2_{hkl}$.

Real space atomic resolution electron tomography of a single NC. A tilt series of atomically resolved projection images was acquired on a single NC from -70° to +70°, with a tilt increment of 2°, using a Thermo Fisher Titan microscope operating at 300 kV with a semi-convergence angle of 20 mrad. To minimize the drift and compensate for scanning distortions during the acquisition, a series of images with a short dwell time was acquired at each tilt angle. Therefore, data restoration and registration were necessary before the tilt series could be aligned with respect to a common tilt axis. The first step in the calculation of the projection image was restoring the individual images of the time series by using a convolutional neural network.[33] Next, these images were used as an input for a rigid and nonrigid average registration procedure.[33] After an iterative alignment based on the phase correlation method, the tilt series was reconstructed using the simultaneous iterative reconstruction technique (SIRT) algorithm.[34] The so-obtained reconstruction yielded atomic resolution data which were converted into a 3D representation of the reciprocal space by calculating a Fourier transform (FT). From this 3D-FT, a 3D mask matching with the 3D-ED diffraction pattern corresponding to the NC was built, from which the unit cell parameters were extracted.

X-Ray Powder Diffraction (XRPD): data collection, *ab initio* structure solution, Rietveld refinement. XRPD analysis was performed in θ:2θ scan mode on a Panalytical Empyrean diffractometer, equipped with a 1.8kW Cu-K_α ceramic anode working at 45 kV-40mA and a PIXcel^{3D} detector. XRPD data were acquired on samples in the form of dry powders; the measurements were carried out in air at room temperature using a zero-diffraction silicon substrate. The *ab initio* structure solution by powder diffraction data was carried out using EXPO2014,[35] a package able to perform all the necessary steps of the process, *i.e.,* indexing, space group determination, full pattern decomposition, structure solution and structure model optimization. Due to the broadening of peaks in the powder diffraction pattern, some of the above steps (*i.e.*, indexing and space group determination) were carried out taking into account the information provided by 3D electron diffraction data. The indexing was performed using the software *N*-TREOR09,[36] which is implemented in EXPO2014. The full pattern decomposition process in EXPO2014 alternates the application of the Le Bail algorithm to least-squares cycles that minimize the residual between the calculated and experimental profiles; the unit cell parameters belong to the set of refined variables. To reduce the errors on the integrated intensities estimates, a non-default full pattern decomposition process was applied, exploiting the prior information on the positivity of the Patterson function. The integrated intensities were automatically supplied to Direct Methods(DM)[37] to carry out the structure solution step, and an automatic procedure able to explore all the twenty stored DM set of phases was executed, providing the corresponding twenty candidate structure models. Among them, the most plausible one, *i.e.* the one satisfying the main crystallochemical rules, was recognized by visual inspection *via* the user-friendly graphical tools of EXPO2014, allowing an easy check of the local chemical environment of the Pb atoms and of the crystal packing. Once the most reliable structural model had been identified and selected, it was further improved *via* the EXPO2014 graphic tools. Additional details concerning the *ab initio* structure solution steps by XRPD are provided in the SI (section S.k).

Rietveld fits of the XRPD profiles were performed with the FULLPROF suite;[38] the peak shape was described with a

Thompson-Cox-Hastings pseudo-Voigt profile. The refined parameters were (according to the need of each fit): scale factor, multiple points linear interpolation background, unit cell parameters, isotropic or anisotropic crystallite size (spherical harmonics), atomic coordinates, and thermal factors (isotropic normally, anisotropic if needed). The instrumental resolution function for the diffractometer was obtained by fitting the XRPD pattern of a LaB_6 standard.[39]

Density Functional Theory (DFT) Calculations. Band structure calculations were performed using the VASP package.[40] The exchange-correlation potential was approximated by the PBE exchange-correlation functional,[41] with the further inclusion of the spin-orbit coupling within the non-collinear approximation. We used a k mesh grid of 4x4x4 for the Brillouin zone integration. The atomic positions were relaxed until the forces were smaller than 0.001 Hartree/Angstrom. We used a kinetic energy cutoff of 400 eV.

3D representation of crystal structures. All the visual representations of crystal structures in this work were created with the software EXPO2014,[35] VESTA,[42] or Mercury.[43]

X-ray and Ultraviolet Photoelectron Spectroscopy (XPS and UPS). Samples for XPS and UPS investigations were prepared onto Au-coated (50 nm) silicon substrates, by either drop-casting or following the same layer-by-layer method described later for the devices fabrication (by spin-coating and solid ligand exchange procedures) in a N_2- filled glovebox. Measurements were performed with a Kratos Axis Ultra^{DLD} spectrometer. For XPS analysis, high-resolution spectra were acquired at a pass energy of 10 eV using a monochromatic Al Kα source (15 kV, 20 mA). The UPS measurements were performed using a He I (21.22 eV) discharge lamp, on an area of 55 μm in diameter, at a pass energy of 5 eV and with a dwell time of 100ms. The work function (namely, the position of the Fermi level with respect to the vacuum level) was measured from the threshold energy for the emission of secondary electrons during He I excitation. A -9.0 V bias was applied to the sample to precisely determine the low-kinetic-energy cutoff, as discussed by Helander *et. al.*[44] Then, the position of the valence band maximum (VBM) versus the vacuum level was estimated by measuring its distance from the Fermi level.[45]

Fourier Transform Infrared spectroscopy (FTIR). We carried out Attenuated Total Reflection – FTIR (ATR-FTIR) measurements under vacuum in a Bruker Vertex® 70v on a 4000-550 cm^{-1} range and 100 repetition scans in order to evaluate the ligands present at the NC surface and their removal for the device fabrication. We performed the measurements by drop-casting 10 μL of NCs colloidal suspensions directly on the diamond crystal. We analyzed both the suspensions in toluene originally used for the devices preparation and that obtained from the redispersion in toluene of the scratched ligand-exchanged NC films (3 layers, see also the following section on device preparation).

Photodetector and solar cell fabrication and characterization. The silicon/SiO_2 (300 nm thermally grown, University wafer®) or the ITO/glass substrates (Ossila – 14-16 Ω/square) were first cleaned in an ultrasonic bath with acetone followed by isopropanol (8 min each step), and finally dried by N_2 flow. Then, N_2 plasma treatment was carried out at 100W for 2 min. The films (thickness ~90 nm for the photodetectors, ~160 nm for the solar cells, measured by a Veeco Dektak® profilometer), were prepared *via* layer-by-layer deposition in 4 and 7 consecutive steps, respectively. Each layer was deposited by spin-coating and ligand exchange procedures in a N_2-filled glovebox. The removal of ligands from the surface of the NCs was evaluated by ATR-FTIR measurements (see SI, Figure S35). For each deposition step, the NCs dispersion (50 mg/mL in toluene, filtered with a 0.2 μm PTFE Sartorius® filter membrane) was spin-coated at 2500 rpm for 20 s (5 s ramp). Then, the substrate was dipped in a NH_4SCN (1.2 mg/mL, for photodetectors), or a 1-Ethyl-3-methylimidazolium iodide (EMII, 7 mg/mL, for solar cells) solution in MeOH for 20 s and rinsed by dipping in a beaker with MeOH before spin-coating again at 2500 rpm for 20 s for drying. To ensure the complete solvent evaporation, we stored the films in a N_2-filled box overnight before carrying out the buffer layers or contacts evaporation. For the solar cell, the buffer layer (MoO_3, 12 nm, from Puratronic® - 99.9995%, Alfa Aesar) and the Au top-metal contacts (80 nm, from EvoChem – 99.99%) were deposited onto the film by using a thermal evaporator inside a glovebox (rate 0.5 Å/s) with the help of a shadow mask (0.03 cm^2 circular pads). The Al-doped zinc oxide (AZO) electron transporting layer was prepared in a two-step procedure by spin-coating at 2500 rpm for 30 s (5 s ramp) and subsequent annealing (140 °C for 10 min, 1h ramp in a Nabertherm P330 furnace) of a precursor solution in ethanol. This step was carried out twice to reach a final AZO compact layer with a thickness of ~50 nm. The precursor solution was prepared adapting an established protocol.[46] Briefly, 1g of $Zn(CH_3COO)_2{\cdot}2H_2O$ and 18 mg of $Al(NO_3)_3{\cdot}9H_2O$ were mixed in 8 mL of ethanol at 80°C during 2.5h and subsequently, still warm, filtered through a 0.2 μm PTFE filter membrane (Sartorius®). The precursor solution was again filtered through a 0.2 μm PTFE filter membrane just before the spin-coating. For the photoconductor, the NC film was spin-coated onto a SiO_2/Si substrate with pre-interdigitated electrodes (Ti/Au, 10/50 nm). The electrodes were prepared *via* standard photolithography and had an inter-electrode gap of 1 μm.

SEM imaging of the films and devices was performed on a Helios Nanolab® 600 DualBeam microscope (Thermo Fisher), using 5kV and 0.2 nA as measurement parameters. Focused ion beam (FIB) was used to prepare cross-section of the solar cell samples for evaluating the thickness of the layers forming the stack.

Photoconductivity measurements. The photoelectrical characterization was performed in air, using a Keithley 2612 source meter connected to a KarlSuss – Microtech probe station in a two-probe configuration. As a light source, we used a mounted 9-array matrix of white light emitting diodes (LEDs, ILH-ON09-VA) from Intelligent LED Solutions® with emission wavelength in the 400-750 nm range with a power density of 100 mW/cm^2. Current-voltage and current-time (at fixed voltage) measurements were acquired during on/off light cycles.

Solar cell characterization. Current density-voltage (J-V) curves were recorded in air without device encapsulation using a Keithley 2400 source meter under 100 mW/cm^2 (AM1.5G) illumination, provided by a LOT-Oriel LSH601/LSZ163 solar simulator. The light intensity was calibrated with a Newport 91150V reference cell. To test the shelf-life, we stored the solar cells in the dark under ambient atmosphere.

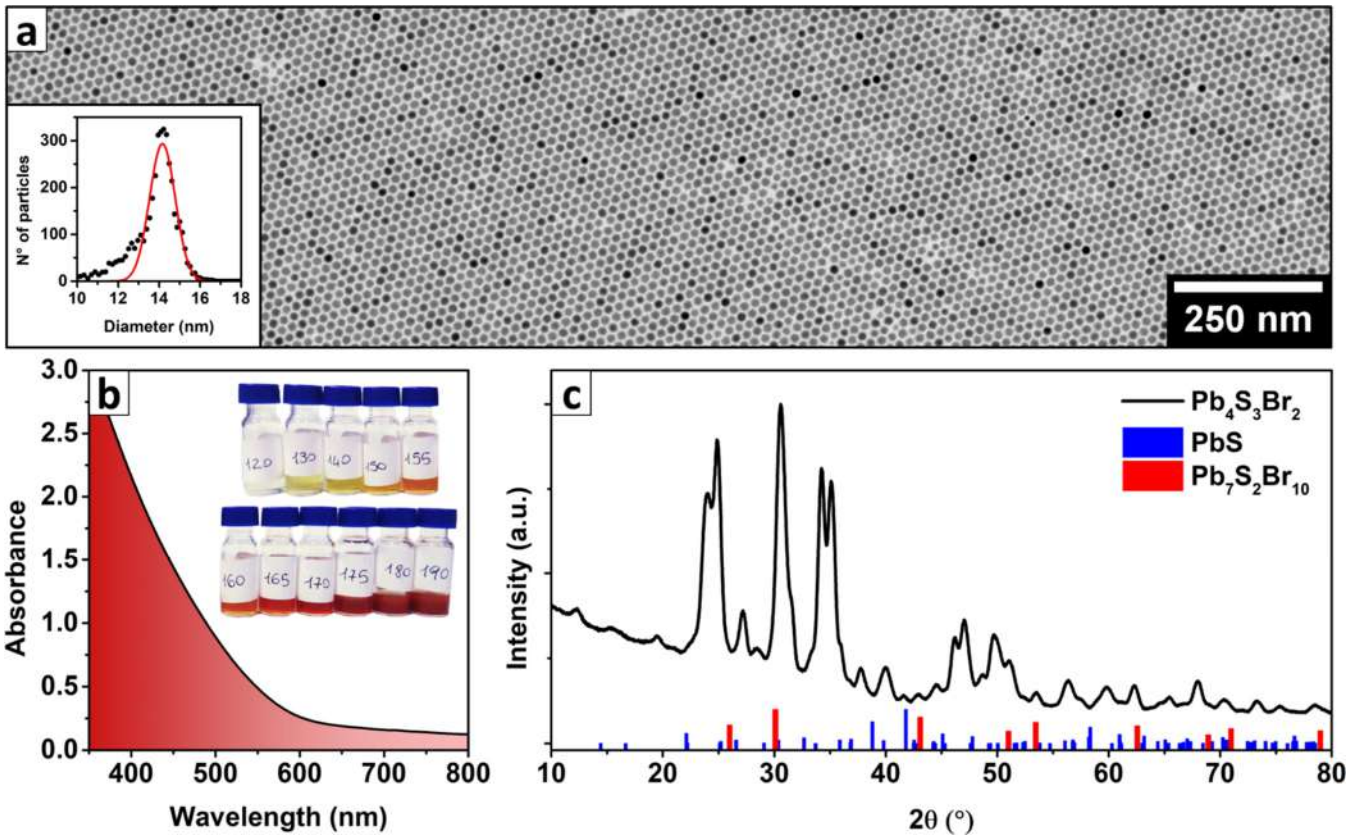

Figure 1. Synthesis and characterization of $Pb_4S_3Br_2$ NCs. a) TEM image of $Pb_4S_3Br_2$ NCs prepared by quenching the synthesis at 180°C (Gaussian fit of their size distribution: 14.2±0.7 nm, inset on the left); b) Absorption spectrum of the sample reported in Figure 1a, along with a photograph of several aliquots of the same synthetic batch quenched at increasing temperatures (inset, T reported on labels in °C). As shown in Figure S3, the spectral profile is not dependent on the particles size and the color difference only depends on the concentration increment; c) XRPD pattern of $Pb_4S_3Br_2$ NCs compared with that of PbS (ICSD - 38293) and $Pb_7S_2Br_{10}$ (ICSD – 21041), evidencing that there is no match with these most obvious candidates.

RESULTS AND DISCUSSION

Synthesis and size control of NCs. The $Pb_4S_3Br_2$ NCs were prepared by modifying the heat-up synthetic approach described in our previous work on PbS nanosheets, which relies on the thermal decomposition of SCN^- ions as a source of S^{2-}, in the presence of Pb^{2+} and Br^- ions.[26] Our approach yielded nearly monodisperse polyhedral (roughly spherical) NCs, with an average diameter that was tunable between 7 and 16 nm. We were able to control the diameter by varying the maximum temperature reached before quenching the reaction (up to the limit of 190°C). For example, quenching at 180°C produced 14.2 ± 0.7 nm particles (Figure 1a and related inset). During the reaction, the originally formed nuclei grew as more and more S^{2-} was released by the SCN^- decomposition. The progress of the reaction could be tracked through monitoring any changes in the color of the solution or by examining the evolution of the absorption spectrum: the growth kinetics were explored by quenching several aliquots of the reaction batch at different temperatures and measuring the absorption spectra and particle size for each aliquot (Figure 1b, see also Figures S1-4 and Table S1 of the SI). Above 190°C, the unreacted $PbBr_2$ started to become insoluble, contaminating the product. It was still possible to obtain larger particles and avoid the $PbBr_2$ precipitation, while also retaining a narrow size distribution, by further accreting a smaller batch of NCs at a lower temperature. Briefly, the crude reaction mixture of a synthesis quenched at 170°C was reheated to the same constant temperature, and a $PbBr_2$ + $Pb(SCN)_2$ solution (prepared as in a standard heat-up synthesis) was added dropwise at a rate of 5 mL/h with a syringe pump. This enabled us to grow particles up to ~30 nm in diameter (Figure S5), which were used for the 3D-electron diffraction (3D-ED) experiments. However, nanoplatelets with essentially the same composition, as determined by EDX analysis, appeared as a side product, eventually becoming a consistent fraction (Figure S6 and Table S2). Most of them could be removed by decanting the reaction product in 40 mL of toluene and disposing the nanoplatelets-rich supernatant multiple times until the sample purity was satisfactory.

Compositional and structural characterization. We first determined the stoichiometry of our material *via* XPS, which yielded an elemental ratio of Pb:S:Br = 43:32:25. This was consistent with the proposed $Pb_4S_3Br_2$ stoichiometry (Pb:S:Br = 44.4:33.4:22.4) after the instrumental errors and crystal termination effects had been considered (Figure S11 and Table S5). A similar stoichiometry was also measured on a film of NCs *via* SEM-EDX analysis (Pb:S:Br = 43:30:27, see Table S6, and Figure S12a-b). We also verified that Pb, S, and Br were uniformly distributed in the NCs through STEM-EDX analysis (Figure S12c-f). Until now, no compound with such a stoichiometry has been reported, and the XRPD pattern could not be assigned to any known structure (Figure 1c): this was the first hint that we had obtained a new crystalline phase. To gain a better insight into the stoichiometry of this new material, we investigated our NCs by a combination of thermogravimetry and XRPD analyses. A sample that had been washed with ethyl acetate to remove the

excess of ligands and unreacted precursors was decomposed in an N_2 atmosphere on a 10°C/min thermal ramp up to 900°C, evidencing three mass losses at around 250°C, 500°C and 800°C (Figure 2a).

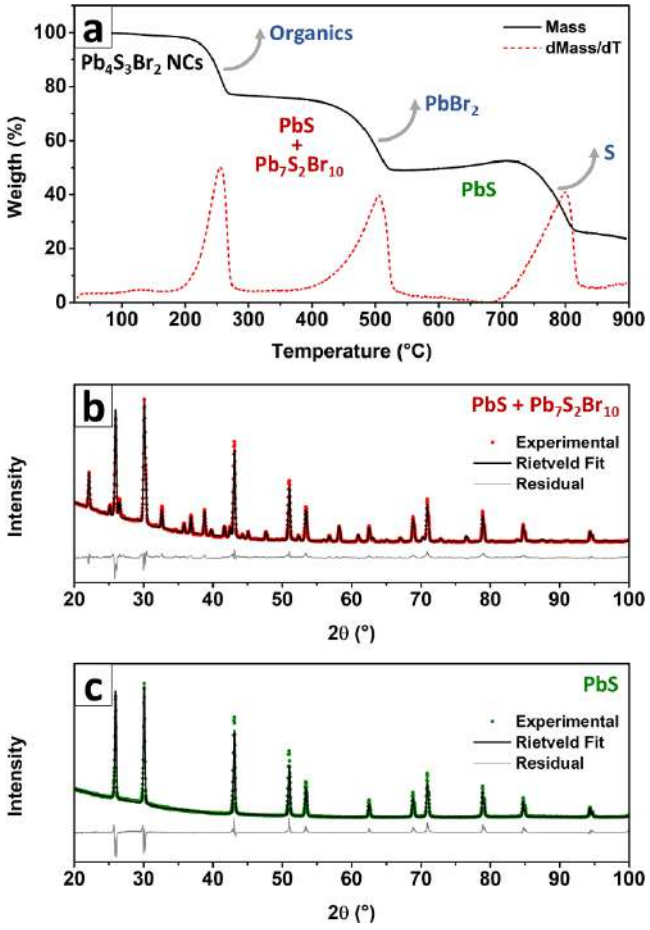

Figure 2. Thermal stability and decomposition of $Pb_4S_3Br_2$ NCs. a) TGA curve of a $Pb_4S_3Br_2$ NCs sample, showing the three distinct weight losses that the material undergoes upon heating. b) Rietveld fit of the product of the first mass loss (≈350°C), demonstrating that what is left after this step is a mixture of PbS and $Pb_7S_2Br_{10}$. c) Rietveld fit of the XRPD pattern for product of the second mass loss (≈600°C), demonstrating that only PbS is left.

XRPD patterns were acquired before the analysis and after the first two mass loss steps, demonstrating that the sample first decomposed to a mixture of $Pb_7S_2Br_{10}$ and PbS (Figure 2b), then further degraded to pure PbS (Figure 2c). The first step was found to be heavily sample-dependent in terms of mass loss, and occurred in a temperature range (up to ~250°C in Figure 2a) that was compatible with the desorption of organic molecules (solvent and ligands, see SI section S.g).[47] Concomitantly with this organic mass loss, the inorganic fraction recrystallized into a mixture of $Pb_7S_2Br_{10}$ and PbS. The second mass loss (up to 500°C), instead, occurred due to the loss of $PbBr_2$, which is known to be a rather volatile compound in its molecular form.[48,49] This is consistent with the fact that the only product left after the second mass loss was PbS (Figure 2c). Hence, in this second step, the following decomposition reaction took place:

$$Pb_7S_2Br_{10(s)} \rightarrow 2\ PbS_{(s)} + 5\ PbBr_{2(g)}$$

We exploited the results from TGA and XRPD to calculate the initial composition of our material, and obtained elemental ratios for Pb:S:Br equal to 44.5:33.5:22.1 (based on 4 TGA analyses on four different NC samples, see Table S7). These ratios are in excellent agreement with the XPS measurements and with the proposed $Pb_4S_3Br_2$ stoichiometry (see SI section S.g, Figures S13-S15 and Table S7 for details). Finally, the third mass loss (Figure 2a) is compatible with the decomposition of PbS and sublimation of S.[50]

We inspected some individual NCs *via* high resolution high angle annular dark field STEM (HAADF-STEM) imaging (Figure 4a). The NCs proved to be single-crystalline and homogeneous, with no evident differences between the core and the surface regions. Neither the STEM images nor their corresponding Fourier transforms (FT)s could be matched with known phases, reinforcing the idea that our NCs had a structure that was unknown to date. During the analysis, some degree of electron beam damage was observed upon scanning: the outer surface of the NCs amorphized. Furthermore, several high contrast crystalline particles (~5 nm), which were identified as Pb and PbS, based on their crystal structure, were formed (Figure S16). The nucleation and growth of metallic Pb clusters upon beam-induced halide sublimation is not surprising, as it has been observed before when investigating lead halide perovskite NCs.[51,52] On the other hand, the presence of PbS is consistent with our observations on the decomposition of this metastable material through the TGA-XRPD analysis discussed earlier.

In order to gain insight on this new crystal structure, we performed 3D-ED experiments on the largest polyhedral NCs that we could synthesize (~30 nm, Figure 3a-d). We identified an orthorhombic cell with parameters a = 8.2(2) Å, b = 14.6(3) Å, c = 8.1(2) Å. Unfortunately, our experimental setting cannot collect precession data from NCs smaller than 50 nm, therefore we could not directly acquire robust information about the symmetry and the atomic positions.[53] Precession 3D-ED data could instead be obtained from the nanoplatelets (Figure S17) that were found as byproducts in the same batch, and these delivered slightly different cell parameters a = 8.0(2) Å, b = 15.5(3) Å, c = 7.9(2) Å. The crystallographic c axis was found to be always parallel to the main direction of growth of the platelets, while the b axis was orthogonal to the main platelet facet. The space group was unambiguously determined as *Pnma* (#62) *via* systematic extinctions analysis, and the structure could be reliably solved *ab initio* on the base of 3D-ED data (Table S8). Assuming the same space group for the spherical NCs, a tentative yet comparable *ab initio* structure was also obtained with non-precessed data collected from the spherical NCs, suggesting a very close structural resemblance between the two types of NC morphologies (namely, the roughly spherical NCs and the nanoplatelets, Figure S18). Consequently, we assumed as a first description of the NCs structure a hybrid cell, featuring the unit cell parameters of the spherical NC and the atomic coordinates of the nanoplatelets (Figure 4c).

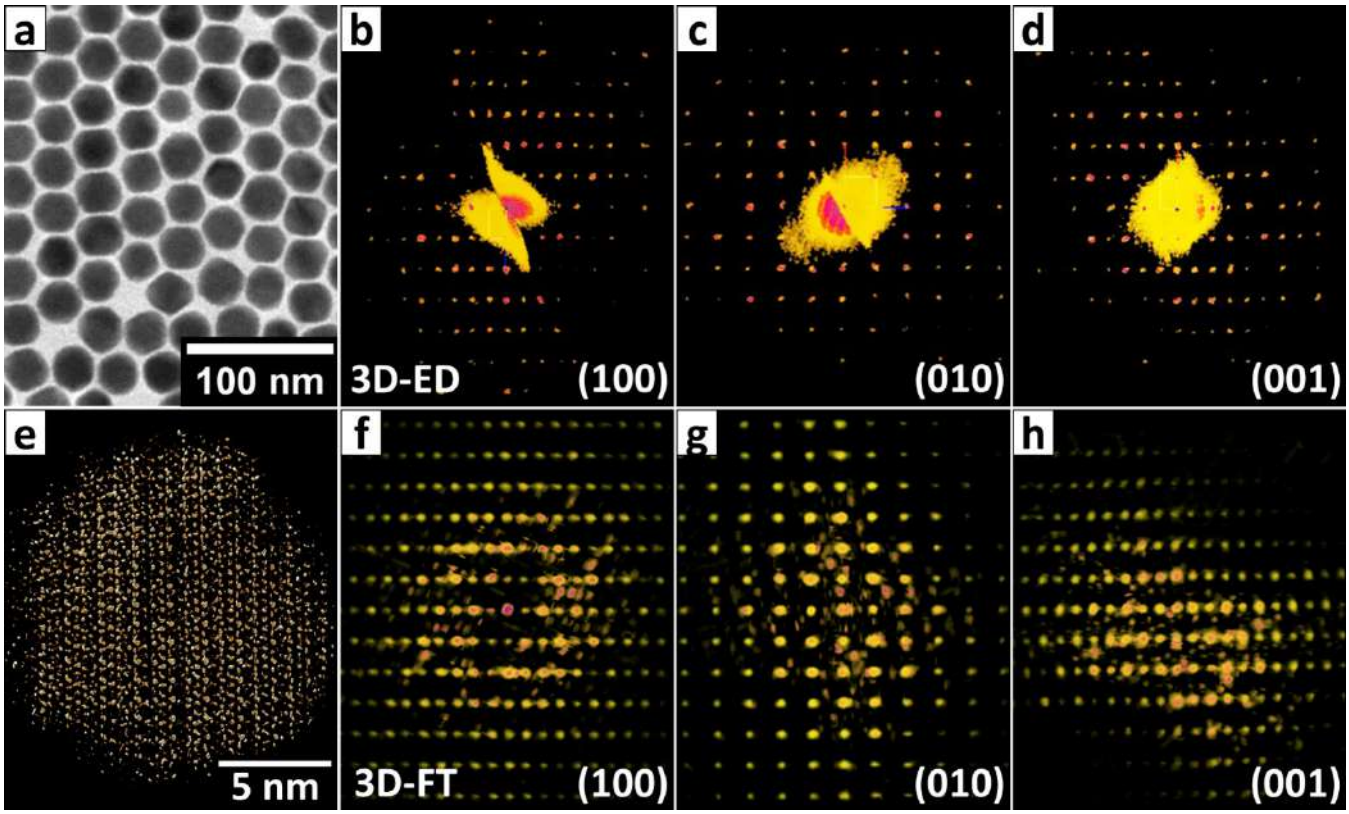

Figure 3. 3D-ED and 3D-FT on $Pb_4S_3Br_2$ NCs. a) TEM image of the $Pb_4S_3Br_2$ NCs investigated *via* 3D-ED and b-d) electron diffraction patterns of a NC oriented along different zone axes. e) 3D electron tomography reconstruction of one spherical $Pb_4S_3Br_2$ NC and f-h) the corresponding 3D-FT projected along different zone axes (before application of the mask, see details in the text).

In the attempt to confirm the structural model obtained from the 3D-ED data, we acquired the direct-space atomic resolution 3D tomography of a single ≈16 nm spherical NC. Upon the acquisition of the first HAADF-STEM images, we again observed immediate electron beam damage and amorphization at the outer atomic layers of the NC. However, during the rest of the experiment the damage did not progress further, and consequently the inner part of the 3D reconstruction could be used for further analyses (Figure 3e and S19, Movie_S1). We did not succeed in extracting the atomic coordinates from the tomography data, due to the high structural complexity and most likely also due to the beam damage. However, we could compute its 3D-Fourier transform (3D-FT, Figure 3b), which produced a 3D map of the NC reciprocal space which is comparable to that obtained by 3D-ED (Figure 3f-h). The data were cleaned from noise and interferences by applying a mask built on the base of the proposed unit cell (Figures 4b and S20, Movies_S2 and S3), which correctly fitted the data and allowed us to extract an orthorhombic cell with lattice parameters a = 8.3 Å, b = 15,1 Å, c = 8.2 Å, in close agreement with that from the 3D-ED.

Hence, by combining data from 3D-ED and 3D-FT we could confirm the unit cell of the spherical NCs. In order to check the atomic coordinates as well, we attempted an independent *ab initio* structure solution from X-Ray powder diffraction data (XRPD) using the software EXPO2014.[35] The first and most critical step of the XRPD-based structural solution, especially in the case of nanomaterials, is the indexing process. The broad and largely overlapped peaks characteristic of NC XRPD prevented the indexing procedure from identifying the cell parameters with high confidence and by a default run (see SI).[54] For the same reason, the automatic space group determination failed due to the unavoidable errors on the integrated intensities. The selection of the unit cell was therefore guided by the information provided by the analysis of 3D-ED, and the space group *Pnma* was considered for carrying out the *ab initio* structure solution. At the end of the solution process, the structural model determined on NCs by XRPD (SI section S.k, Figure S21 and Table S9) was found to be very similar to the one determined by 3D-ED. The two structures are characterized by a root mean square deviation (RMSD) equal to 0.534 Å, where $RMSD=\mathrm{sqrt}(\Sigma_i d_i^2/N_{au})$, *i.e.*, the square root of the averaged squared distances between couples of corresponding atoms in the two compared models, with N_{au} the number of atoms in the asymmetric unit (Figure S22). The unit cell parameters refined from XRPD by EXPO2014 (a = 8.22592 Å, b = 14.70843 Å, c = 8.13988 Å) were in good agreement with the ones of 3D-ED procedure as well. In order to further confirm the equivalence of models obtained independently by 3D-ED and XRPD, we relied on DFT calculations to relax both structures, by minimizing the interatomic forces. We kept the cell parameters fixed to the more precise values extracted from the XRPD data. The two structures relaxed to the same model: this confirmed that they are equivalent, and, since they came from independent datasets and techniques, we consider this agreement a good proof of their reliability (Figure 4c, see also Figure S23). It is also worth noting that the 3D-ED derived model was the one closer to the relaxed structure.

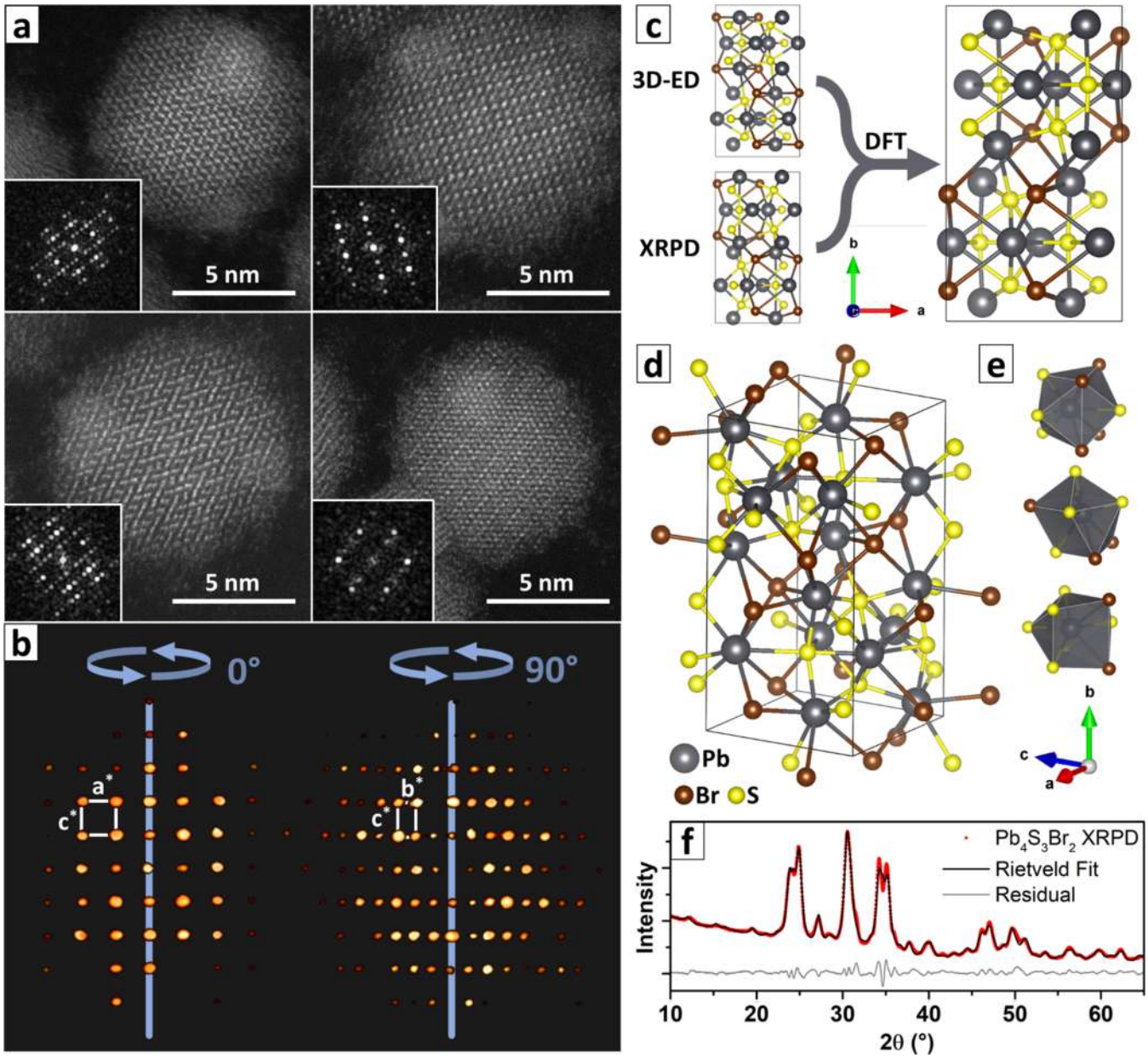

Figure 4. HAADF-STEM and 3D-FT of NCs; 3D-ED and XRPD structural models for $Pb_4S_3Br_2$. a) Atomic resolution images of $Pb_4S_3Br_2$ NCs evidencing their single-crystalline nature. Insets: corresponding FT. b) Two projections of the calculated 3D-FT, oriented so that the reciprocal cell base vectors are clearly recognizable. c) The models obtained from 3D-ED and from XRPD converge to the same structure upon DFT relaxation. d) The $Pb_4S_3Br_2$ NCs crystal structure as obtained at the end of the workflow described in the main text, together with e) the coordination polyhedra for the three non-equivalent lead crystallographic sites. f) Rietveld refinement of the XRPD pattern based on the structure shown in panel d.

The structure we propose for $Pb_4S_3Br_2$ at the end of this multiple-technique workflow (Figures 4d-e, see also Figure S26b) is orthorhombic, it belongs to the *Pnma* (#62) space group, and has unit cell parameters a = 8.226 Å, b = 14.708 Å, c = 8.140 Å. Lead atoms are involved in three different coordination environments. Every lead atom is octa-coordinated, with two Pb sites surrounded by 4 S + 4 Br and one Pb site surrounded by 6 S + 2 Br. Sulfur is found in two non-equivalent crystallographic sites, both with a distorted octahedral coordination (as found in PbS), while bromine occupies an epta-coordinated pentagonal bipyramidal site. We want to point out that the unit cell parameters were independently confirmed by three different techniques (3D-ED, XRPD, atomic resolution electron tomography) and are most likely correct. The Rietveld refinement of the structure based on the XRPD pattern confirmed the values (a = 8.202 Å, b = 14.707 Å, c = 8.165 Å, Figure 4f, SI section S.n, Figure S27), and had a minor impact on the atomic coordinates almost unchanged as well. The residual curve however highlights some minor discrepancies, probably arising from a combination of factors, such as the struggle of the Rietveld method to correctly fit the many broad overlapping reflections and the presence of strain or distortions.

There are striking similarities between the $Pb_4S_3Br_2$ phase we propose for our NCs and the recently discovered $Pb_4S_3I_2$, which was obtained at high pressures and temperatures (4 GPa, 600°C) in the form of bulk crystals.[21] Both phases have the same $Pb_4S_3X_2$ stoichiometry, crystallize in the same space group and have an equivalent atomic layout (Figure S26). For example, in both structures the Pb

atoms form layers along the *b* axis, while the anions are alternated in sulfur-only and mixed sulfur-bromine layers.[18] These evidences confirm that we have discovered a structural variation in a yet underexplored family of compounds: our hypothesis is that $Pb_4S_3Br_2$ is a kinetically-trapped high-pressure metastable structure as well. First, the reader should be reminded that the room pressure pseudo-binary phase diagram PbS-$PbBr_2$ contemplates only PbS, $PbBr_2$ and $Pb_7S_2Br_{10}$ as stable phases.[16] This is consistent with what we observed in our TGA-XRPD experiments: thermally annealing the NCs at temperatures above 250°C causes their transition into a mixture of the thermodynamically stable PbS and $Pb_7S_2Br_{10}$ phases. Second, if compared to the published $Pb_4S_3I_2$ model the $Pb_4S_3Br_2$ structure appears to be contracted along the *b* axis (- 5.5 %), while the *a* and *c* axes retain basically the same length (*a* = +1.2; *c* = -0.5 %), suggesting some sort of anisotropic structural relaxation. Furthermore, the hypothesis of $Pb_4S_3Br_2$ being itself a metastable high-pressure phase is consistent with the morphology-dependent structural relaxation that we observed in our samples. We discussed above that NCs and nanoplatelets feature closely related structures, distinguished only by the length of the *b* parameter and by a minor rearrangement of the atomic positions.

To gain insight on this peculiar behavior, we again relaxed our 3D-ED and XRPD structural models by DFT calculations, this time letting the unit cell parameters *a*, *b*, and *c* free to vary. Remarkably, both models converged to a structure that was close to that obtained *ab initio* from 3D-ED data for the nanoplatelets, especially in terms of unit cell parameters (3D-ED *a* = 8.0 Å, *b* = 15.5 Å, *c* = 7.9 Å; DFT *a* = 8.14 Å, *b* = 15.42 Å, *c*= 8.08 Å, Figure S24). This suggests that the latter represents the relaxed form of the otherwise kinetically trapped high-pressure phase found in the spherical NCs. It is worth noting that the *b* axis, which is the one varying the most from nanoplatelets to NCs, is perpendicular to the nanoplatelets surface, a possible indication that the relaxation prevents the accretion of the crystal in the relaxed direction, while at the same time allowing the lateral growth (along the *a* and *c* directions). The different cell parameters observed for the two nanoparticle morphologies, and the impossibility of growing pseudospherical NCs larger than ~30 nm in diameter, suggests a critical size transition in cell parameters. We hypothesize therefore that a sort of high-pressure phase is possible only for the smaller NCs, most likely as a result of an overall energy balance in which the surface energy term plays an important role.

Optoelectronic properties. $Pb_4S_3Br_2$ NCs feature a strong absorption in the visible, starting from an intermediate region between that of the white wide-bandgap lead bromide (≈4 eV in bulk)[55] and of the black small-bandgap lead sulphide (0.59 eV for 10 nm NCs, 0.41 eV in bulk).[56,57] The absorption decreases towards lower energies and becomes negligible after ≈ 650 nm (1.91 eV), causing the material to appear red in a concentrated solution (Figure 1b). Interestingly, we observed that the absorption spectrum remains unchanged while varying the size of NCs in our tunability range (7 – 16 nm), thus suggesting that quantum confinement effects are negligible for $Pb_4S_3Br_2$ (Figure S3). Also, no photoluminescence was detected in the range 500 – 1700 nm. The observed spectral features are consistent with that predicted by computing the band structure: calculations were performed at the DFT/PBE level of theory, which included spin–orbit coupling (SOC), on both the cell-relaxed and the cell-fixed structures (respectively corresponding to the spherical $Pb_4S_3Br_2$ NCs and nanoplatelets). Noteworthily, the results of the simulations do not change drastically, as in both cases an indirect band gap of ≈1.5 eV is predicted (Figures 5a, see also Figure S23). However, the PBE functional is known to underestimate the bandgap for extended systems, due to a strongly localized hole.[58] In this case, the spin-free bandgap value for lead sulfide systems is a better approximation to the experimental bandgap as a consequence of error cancellation.[59] For comparison, we thus computed the bandgap without SOC (Figure S23), which lies at 1.98 eV, closer to the absorption onset of 1.91 eV (650 nm) estimated from the experimental spectrum. The density of states calculation highlights that the two elements, Pb and S, mainly contribute to the band-edge states, while the Br-related states are mainly located deeper below the valence band edge (Figure 5b).

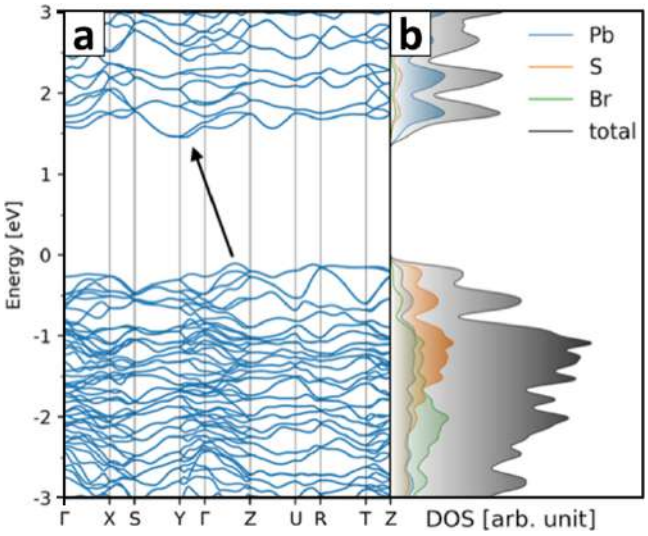

Figure 5. $Pb_4S_3Br_2$ NCs band structure. The band structure was calculated at DFT/PBE+SOC level of theory on the model shown in Figure 4d. The band structure features an indirect bandgap. The density of states diagram shows that the elements mostly contributing to the band-edge states are S for the valence and Pb for the conduction band, while Br-related states fall deeper in the valence band.

Stability, ligand exchange and testing of $Pb_4S_3Br_2$ NCs in devices. The electronic structure of this material, together with its chemical affinity with the optically active lead-bromide perovskites and lead chalcogenides, suggest a potential exploitation of $Pb_4S_3Br_2$ NCs as an active layer in photosensitive devices. In the perspective of applications, we performed basic temporal stability tests. NCs were stored at room temperature in the dark both as a diluted colloidal suspension in toluene and as dry powder. The absorption spectra and XRPD patterns were compared with that of the fresh samples after two months, and no difference was found (Figure S28). Encouraged by these results, we fabricated both photodetector and solar cell test devices. The $Pb_4S_3Br_2$ NCs for the devices fabrication were prepared by quenching the reaction at 170°C, centrifuging at 6000 rpm for 5 min, discarding the precipitate and then recovering the NCs in the supernatant *via* ethyl-acetate assisted precipitation, which also partially washed the excess of organics from the synthesis.

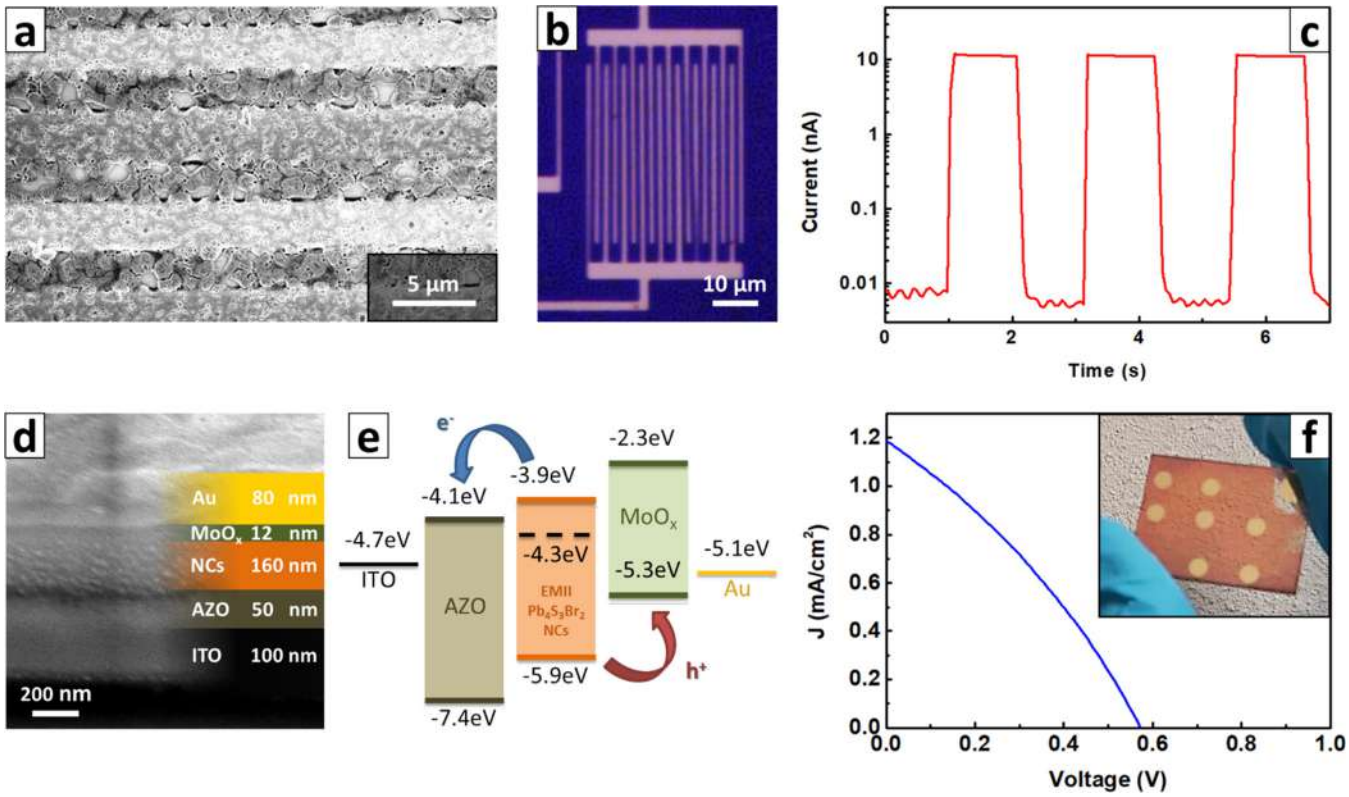

Figure 6. $Pb_4S_3Br_2$ photoconductor and solar cell characterization. a) Section of the $Pb_4S_3Br_2$ NC film on a photodetector (SEM). b) Optical microscope image of the photodetector with interdigitated electrodes. c) Current response during light on/light off cycles of a device with interdigitated electrodes. d) SEM image of a solar cell stack cross-section. e) Energy level alignment in the stack ($Pb_4S_3Br_2$ values measured by UPS; ITO, AZO, MoO_x and Au values from the literature, see refs. [46,60–63] respectively). f) Current-voltage curve under AM1.5G illumination for a solar cell with the stack shown in panel c. Inset: photo of a representative sample.

Prior to the device fabrication, we tested two ligand exchange procedures directly on NCs films, in order to replace the long molecules on the NC surface with shorter ligands and thus improve the film conductivity (additional details can be found in the experimental section). In the FTIR spectrum of the as-prepared NCs (Figure S35, top spectrum) one can observe main bands located at 2953/2924/2853 cm^{-1} together with features at 1466/1412 cm^{-1} which corresponds respectively to the CH_3 and CH_2 stretching and CH_2 bending of the alkyl chains from oleic acid and/or oleylamine.[26,64] Moreover, the appearance of a band at 1520 cm^{-1} corresponding to the C=O stretching confirms the presence of Pb-bound oleate at the NC surface.[64] A broad band at 2040 cm^{-1} (S=C=N stretching) and features at 1312/1266 cm^{-1} (C-N stretching), which can be attributed to SCN^- and to oleylamine attached at the NC surface respectively, were present as well.[26,65] Hence, we concluded that the surface passivation of the as-synthesized NCs comprises various ligand molecules. However, after ligand exchange using NH_4SCN or EMII all the long-chain ligands coming from the synthesis were removed, as indicated by the disappearance of the corresponding FTIR bands (Figure S35, middle and bottom spectra) and confirmed by XPS analysis, where the peaks related to carbon and oxygen were absent after the exchange (Figure S31).

We tested the response of $Pb_4S_3Br_2$ NCs in a photoconductor device fabricated by layer-by-layer spin-coating the NC dispersion onto Si/SiO_2 substrates with pre-patterned interdigitated electrodes (Figure 6a-b). The layer-by-layer deposition, followed by ligand exchange with thiocyanate (using NH_4SCN as a SCN^- source) was repeated 4 times to produce a compact film (thickness ~90 nm, Figure 6a). When measured in the dark, the devices produced low current (< pA at 20 V). Then, under white light (400-750 nm, 100 mW/cm^2), the device immediately responded, with a current of ~10 nA, as shown in Figure 6c.

The responsivity $R = I_{photo}/P_{opt}$ (I_{photo} = photocurrent, P_{opt} = optical power on the device) was measured on 4 different devices to be R = 4±1 mA/W (best device 5 mA/W), The detectivity was $(3\pm1)\times10^8$ Jones, estimated from the noise power density spectrum of a time trace acquired in the dark (Figure S30).[66] We also evaluated the normalized photocurrent to dark current ratio NPDR = R/I_{dark} (I_{dark} = dark current), a suitable figure of merit in the case of devices with very low dark current.[67] In our case, we measured NPDR = $(8.5 \pm 2.8)\times10^5$ mW^{-1}. For the solar cell tests, we prepared a layered stack on ITO/glass substrate comprising AZO (as electron transport layer – ETL), the photoactive $Pb_4S_3Br_2$ NCs layer, MoO_x as buffer layer, and Au as top contact (Figure 6d). In order to make the $Pb_4S_3Br_2$ NCs layer conductive, a -ligand exchange was performed with iodine (using EMII as a I^- source), as described earlier. The suitability of the energy level alignment resulting from the ligand exchange in the layered stack was verified by UPS measurements see Figure 6e and SI section S.q, Figures S32 and S33, for further details regarding to XPS and UPS analyses). With this configuration, the non-encapsulated best solar cell showed a PCE of 0.21±0.02%% (average from 4 different devices), J_{sc} = 1.2 mA cm^{-2} (1.09 ± 0.07 mA/cm^2) and V_{oc} = 0.57 V (0.58 ± 0.03 V) under a standard AM1.5G illumination in air

(Figure 6f). The solar cells demonstrated a good long-term stability under ambient atmosphere, retaining 60% of the PCE after more than 2 months of storage (Figure S29). The performance showed by our devices (R = 4 ± 1 mA/W or PCE = 0.22 %), in comparison with state-of-the-art for NCs based devices, is not reaching the common figures of merit of responsivity or PCE. Responsivity in photoconductors built with lead-halide perovskites exceeds 10^6 A/W, and even early results with CdX (X = S, Se, Te) reached 200 mA/W (see, e.g., refs.[68–70]).

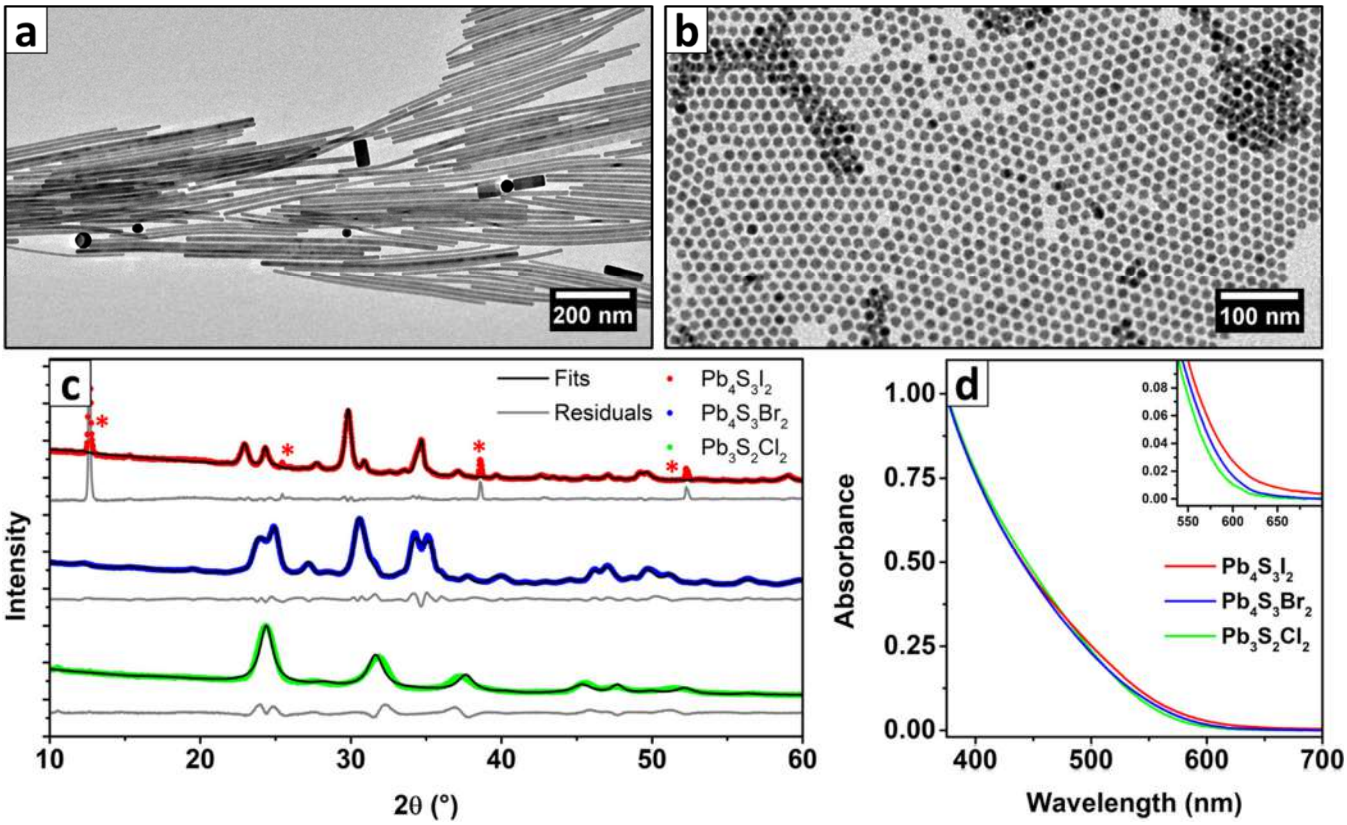

Figure 7. Characterization of $Pb_4S_3I_2$ and $Pb_3S_2Cl_2$ NCs. TEM images of a) $Pb_4S_3I_2$ and b) $Pb_3S_2Cl_2$ NCs. c) XRPD patterns of the three NC samples ($Pb_4S_3I_2$, $Pb_4S_3Br_2$, $Pb_3S_2Cl_2$) and related Rietveld fits (Tables S3, S4 and S9). The red asterisks in the $Pb_4S_3I_2$ pattern highlights the peaks coming from an impurity, most likely PbI_2 nanosheets or flakes. d) Optical absorption spectra of the three samples. The almost perfect overlap suggests that, despite the different composition, stoichiometry and structure, the halides play a very minor role in the optical properties of this class of nanomaterials. The only appreciable trend is visible at the onset of the spectrum (inset).

We compared the NPDR of our photodetectors with that of metal/semiconductor/metal devices, and found that our system performs well in comparison, e.g., with semiconductor/CNT[71] or semiconductor/graphene[72] systems, typically featuring values of ~10^4 mW^{-1}, or nanostructured silicon[73] (~10^4 mW^{-1}), and is comparable with nanomembrane-enhanced Ge detectors[74]; our configuration offers nonetheless a simpler fabrication protocol. We could reach these results thanks to the very low dark current, which also suggests that these devices can operate with low power consumption. Instead, regarding the performance of solar cell and comparing it with systems absorbing in the visible range, the PCE obtained is far from the results achieved with or $CsPbI_3$ (13.4%)[75], or CdTe quantum dot (11.6%).[76] Considering the results from the photoconductor and solar cell, we could envision for our material a role in multi-layer stacks operating as charge transport layer with some additional photogeneration[62,63] rather than as the main active layer, whose band alignment can be favorably tuned by surface chemistry (SI section S.q). In fact, our material reaches a responsivity comparable to polymers (0.2-0.7 mA/W),[54] which are commonly used as charge transport layers.

Preliminary investigation of Iodide and Chloride-based NCs. Driven by the strong analogy between the structure of our NCs and that of the reported high-pressure phase $Pb_4S_3I_2$, we tried to prepare NCs of other chalcohalides by using PbI_2 and PCl_2 in place of $PbBr_2$ as halide precursors in the synthesis: in both attempts we obtained colloidal nanoparticles. In the case of $Pb_4S_3I_2$, the NCs were larger than for the $Pb_4S_3Br_2$ case discussed above (up to hundreds of nm, and polydisperse), and had the shape of elongated prisms or rods (Figure 7a, see also Figure S7). The color was slightly different from that of $Pb_4S_3Br_2$, tending to brown, most probably due to the scattering caused by the large size of obtained NCs. We confirmed the crystal structure by Rietveld fitting the XRPD pattern on the base of the structure published by Ni *et. al.*,[21] discovering at the same time the presence of an byproduct identified by some residual peaks (Figure 7c, top pattern), which we suspect to be PbI_2 nanosheets or flakes on the base of the match with published XRDP data (see also Figure S8).[77,78] We take the remarkable resemblances between the XRPD patterns of $Pb_4S_3I_2$ and $Pb_4S_3Br_2$ as an additional proof of the close similarity of the two structures.

The chlorine based NCs we prepared were instead smaller than the $Pb_4S_3Br_2$ NCs prepared under comparable conditions (7.0 ± 0.8

nm when quenched at 170°C), but they featured a very similar shape (roughly spherical, Figure 7b and Figure S9a). The synthesis often produced PbS NCs as a byproduct, which could however be removed by simple centrifugation due to their larger size (see Figure S9b). The color of the purified product was almost identical to that of $Pb_4S_3Br_2$ NCs. Thus, we were surprised to discover that the XRPD pattern of the two phases, namely, the Cl-based NCs (Figure 7c, green pattern) and the $Pb_4S_3Br_2$ NCs (Figure 7c, blue pattern) were remarkably different. A close match with the XRPD lines reported in 1969 by Rabenau *et. al.* for the tentative "2PbS + $PbCl_2$" phase first made us suspect that we had obtained the same compound.[16] By XPS compositional analysis we measured Pb:S:Cl ratios corresponding to 42.5:23.9:33.6, which are consistent with the proposed $Pb_3S_2Cl_2$ stoichiometry (Pb:S:Cl = 42.9:28.6:28.6) if measurement errors and crystal termination effects are considered. Driven by this finding, we searched the literature for comparable structures and found that Ni *et. al.* recently reported the bulk synthesis (4 GPa, 700°C) and complete structural characterization of the high-pressure phase $Pb_3Se_2Br_2$.[20] Given the resemblances of stoichiometries and XRPD patterns, our hypothesis was that we had found an isostructural compound: to confirm it, we Rietveld fitted the XRPD pattern of $Pb_3S_2Cl_2$ NC with a model adapted from that published by Ni *et. al.* by replacing Se with S and Br with Cl, and we found a good match (Figure S10). The slight misplacement of the peaks is probably due to a slight deformation of the originally cubic unit cell, but the excessive broadening of the reflections due to the small size of NCs prevented us from gaining a better insight of the material structure. We plan to investigate this aspect in further, more focused studies. We found it remarkable that atoms in $Pb_3S_2Cl_2$ show the same coordination environment found in the other two isostructural materials we reported (Pb = octacoordinated, Cl,S = deformed octahedral) suggesting that the structural variety in this class of lead chalcohalides may arise mainly from a different arrangement of the fundamental structural unities (Figure S26).

Surprisingly, despite the major compositional and structural differences between the three stoichiometries, their absorption spectra are almost identical. The only appreciable trend regards the onset of the spectra, which exhibits a weak redshift in going from the chloride to the bromide and then to the iodide based NCs, suggesting a slightly variable bandgap. Another key element to understand the electronic properties of this class of materials is, as we already mentioned, the absence of size-dependency in the optical spectra of $Pb_4S_3Br_2$ NCs. The same is likely true also for $Pb_4S_3I_2$ and $Pb_3Cl_2Cl_2$, as the remarkable overlap of the three spectra would be an astonishing coincidence otherwise. Finally, we observed that the contribution of the halide to the band-edges states of $Pb_4S_3Br_2$ is negligible (Figure 5b). A very similar trend was predicted, through DFT calculations, also for $Pb_4S_3I_2$ and $Pb_3S_2Cl_2$ (Figure S34). The calculations additionally confirmed the halide-dependent shift of the bandgap ($Pb_3S_2Cl_2$ = 2.02 eV, $Pb_4S_3Br_2$ = 1.98 eV, $Pb_4S_3I_2$ = 1.76 eV), indirect for all of them, which is in good agreement with the experiments. Considering all these observations, our conclusion is that the optical properties of these materials are probably dominated by localized Pb-S interactions. The main effect of the halides is to cause this localization: PbS has an exciton Bohr radius of 18 nm, and most of our NCs are well below this size threshold.[79,80] The mild, halide-dependent shift in the absorption onset is probably due to the local alteration of the electron density surrounding the lead atoms.

As a conclusion, we want to highlight that the formation of these lead chalcohalide phases must be taken into account when performing the synthesis of PbS NCs, as they often exploit lead halide salts as precursors and are normally conducted under conditions similar to that we reported.[81,82] Furthermore, recent work has demonstrated that PbS NCs synthesized from $PbCl_2$ have a $PbCl_2$ rich surface, leading to improved photoluminescence quantum yield and chemical stability, which might be related to the passivation by a layer of the hereby reported $Pb_3S_2Cl_2$ phase.[83–85] This hypothesis may stimulate further studies aiming at a more detailed characterization of those systems.

CONCLUSIONS

In conclusion, we have reported the synthesis of colloidal NCs of a previously unknown, metastable phase belonging to the PbS-$PbBr_2$ system, namely $Pb_4S_3Br_2$. Our synthetic protocol delivers NCs with a narrow size distribution and size tunability over the range 7 – ~30 nm. We were able to solve its structure by a combination of 3D electron diffraction, high resolution HAADF-STEM tomography and powder XRD diffraction, demonstrating that $Pb_4S_3Br_2$ is a metastable structural analogue of the recently reported high-pressure $Pb_4S_3I_2$ phase. Our material is an indirect 1.98 eV bandgap semiconductor and exhibits photo-response and photo-harvesting capabilities, which were tested in a photodetector and a solar cell. Finally, we applied the same synthetic protocol to prepare NCs of the high-pressure $Pb_4S_3I_2$ phase and of a new $Pb_3S_3Cl_2$ chalcohalide phases. Both are indirect bandgap semiconductors (1.76 and 2.02 eV respectively). We expect that the discovery of these new lead chalcohalide NCs will encourage the exploration of other metal chalcohalides, a group of materials that to date has been vastly untapped at the nanoscale.

ASSOCIATED CONTENT

Supporting Information.

The Supporting Information is available free of charge on the ACS Publications website at DOI:

Crystal structure of $Pb_4S_3Br_2$ NCs as obtained from 3D-ED/XRPD + DFT relaxation (Pb4S3Br2_DFT.cif) and after Rietveld refinement (Pb4S3Br2_Rietveld.cif). Crystal structure of $Pb_3S_2Cl_2$ (adapted from the published $Pb_3Se_2Br_2$) after Rietveld fit (Pb3S2Cl2_Rietveld.cif).

Graphical representations of the 3D electron tomography of one $Pb_4S_3Br_2$ NC (Movie_S1) and its computed 3D-FT before (Movie_2) and after (Movie_3) the application of a 3D-ED based mask.

Experimental procedures for the synthesis of $Pb_4S_3Br_2$, $Pb_4S_3I_2$ and $Pb_3S_2Cl_2$ NCs; XPS, EDX, TGA, UPS, FTIR, HAADF-STEM analyses on $Pb_4S_3Br_2$ NCs; 3D electron tomography and 3F-FT of $Pb_4S_3Br_2$ NCs; 3D-ED and XRPD based structure solution for $Pb_4S_3Br_2$ NCs; proposed crystal structures for $Pb_4S_3Br_2$, $Pb_4S_3I_2$ and $Pb_3S_2Cl_2$ NCs; Rietveld fits of $Pb_4S_3Br_2$, $Pb_4S_3I_2$ and $Pb_4S_3Cl_2$ NC XRPD patterns; DFT relaxation of $Pb_4S_3Br_2$ NC structural models; DFT calculations of $Pb_4S_3Br_2$, $Pb_4S_3I_2$ and $Pb_3S_2Cl_2$ NCs band structures; temporal stability tests on $Pb_4S_3Br_2$ NCs; complementary characterization for $Pb_4S_3Br_2$ NC based devices.

AUTHOR INFORMATION

Corresponding Author

ivan.infante@iit.it, annagrazia.moliterni@ic.cnr.it, sara.bals@uantwerpen.be, mauro.gemmi@iit.it, liberato.manna@iit.it,

Present Address

[Φ] Department of Chemistry and Applied Biosciences, ETH Zürich, Vladimir Prelog Weg 1, CH-8093 Zürich, Switzerland

[Γ] CIC nanoGUNE, Tolosa Hiribidea, 76, E-20018 Donostia – San Sebastian, Spain

[⊠] IHP–Leibniz-Institut für innovative Mikroelektronik, Material Research Semiconductor Optoelectronics, Frankfurt (Oder), Germany

[Θ] School of Materials, Sun Yat-sen University, Guangzhou, 510275, China

Author Contributions

[▽] These authors contributed equally.

ACKNOWLEDGMENTS

We would like to thank to Dr. A. Toma for the access to the IIT clean room facilities SEM/FIB and evaporators, the Smart Materials group (IIT) for the access to the ATR-FTIR equipment, S. Marras for the support during XRPD measurements, G. Pugliese for help with the TGA measurements, M. Campolucci for help with the experiments of NCs growth kinetics, S. Lauciello for help with the SEM-EDX analyses and D. Baranov and R. Brescia for the helpful discussions. We also acknowledge funding from the programme for research and Innovation Horizon 2020 (2014-2020) under the Marie Skłodowska-Curie Grant Agreement COMPASS No. 691185. Ivan Infante acknowledges the Dutch NWO for financial support under the Vidi scheme (Grant n. 723.013.002). S.B. acknowledges support by means of the ERC Consolidator Grant No. 815128 REALNANO. E.M. and M.G acknowledge the Regione Toscana for funding the purchase of the Timepix detector through the FELIX project (Por CREO FESR 2014-2020 action).

REFERENCES

(1) Akkerman, Q. A.; Rainò, G.; Kovalenko, M. V.; Manna, L. Genesis, Challenges and Opportunities for Colloidal Lead Halide Perovskite Nanocrystals. *Nat. Mater.* **2018**, *17* (5), 394–405. https://doi.org/10.1038/s41563-018-0018-4.

(2) Lu, H.; Carroll, G. M.; Neale, N. R.; Beard, M. C. Infrared Quantum Dots: Progress, Challenges, and Opportunities. *ACS Nano*. American Chemical Society February 26, 2019, pp 939–953. https://doi.org/10.1021/acsnano.8b09815.

(3) Mcdonald, S. A.; Konstantatos, G.; Zhang, S.; Cyr, P. W.; Klem, E. J. D.; Levina, L.; Sargent, E. H. Solution-Processed PbS Quantum Dot Infrared Photodetectors and Photovoltaics. *Nat. Mater.* **2005**, *4* (2), 138–142. https://doi.org/10.1038/nmat1299.

(4) Mihailovic, D. Inorganic Molecular Wires: Physical and Functional Properties of Transition Metal Chalco-Halide Polymers. *Progress in Materials Science*. Pergamon May 1, 2009, pp 309–350. https://doi.org/10.1016/j.pmatsci.2008.09.001.

(5) Wlaźlak, E.; Blachecki, A.; Bisztyga-Szklarz, M.; Klejna, S.; Mazur, T.; Mech, K.; Pilarczyk, K.; Przyczyna, D.; Suchecki, M.; Zawal, P.; et al. Heavy Pnictogen Chalcohalides: The Synthesis, Structure and Properties of These Rediscovered Semiconductors. *Chem. Commun.* **2018**, *54* (86), 12133–12162. https://doi.org/10.1039/c8cc05149f.

(6) Nowak, M.; Jesionek, M.; Mistewicz, K. Fabrication Techniques of Group 15 Ternary Chalcohalide Nanomaterials. In *Nanomaterials Synthesis*; Elsevier, 2019; pp 337–384. https://doi.org/10.1016/b978-0-12-815751-0.00010-9.

(7) Kunioku, H.; Higashi, M.; Abe, R. Lowerature Synthesis of Bismuth Chalcohalides: Candidate Photovoltaic Materials with Easily, Continuously Controllable Band Gap. *Sci. Rep.* **2016**, *6* (1), 1–7. https://doi.org/10.1038/srep32664.

(8) Fenner, J.; Rabenau, A.; Trageser, G. Solid-State Chemistry of Thio-, Seleno-, and Tellurohalides of Representative and Transition Elements. *Adv. Inorg. Chem. Radiochem.* **1980**, *23* (C), 329–425. https://doi.org/10.1016/S0065-2792(08)60096-5.

(9) Davies, D. W.; Butler, K. T.; Skelton, J. M.; Xie, C.; Oganov, A. R.; Walsh, A. Computer-Aided Design of Metal Chalcohalide Semiconductors: From Chemical Composition to Crystal Structure. *Chem. Sci.* **2018**, *9* (4), 1022–1030. https://doi.org/10.1039/c7sc03961a.

(10) Xiao, J. R.; Yang, S. H.; Feng, F.; Xue, H. G.; Guo, S. P. A Review of the Structural Chemistry and Physical Properties of Metal Chalcogenide Halides. *Coordination Chemistry Reviews*. Elsevier B.V. September 15, 2017, pp 23–47. https://doi.org/10.1016/j.ccr.2017.06.010.

(11) Johnsen, S.; Liu, Z.; Peters, J. A.; Song, J. H.; Nguyen, S.; Malliakas, C. D.; Jin, H.; Freeman, A. J.; Wessels, B. W.; Kanatzidis, M. G. Thallium Chalcohalides for X-Ray and γ-Ray Detection. *J. Am. Chem. Soc.* **2011**, *133* (26), 10030–10033. https://doi.org/10.1021/ja202540t.

(12) Shi, H.; Ming, W.; Du, M. H. Bismuth Chalcohalides and Oxyhalides as Optoelectronic Materials. *Phys. Rev. B* **2016**, *93* (10). https://doi.org/10.1103/PhysRevB.93.104108.

(13) Li, C.; Feng, K.; Tu, H.; Yao, J.; Wu, Y. Four New Chalcohalides, NaBa2SnS4Cl, KBa2SnS4Cl, KBa2SnS4Br and CsBa2SnS4Cl: Syntheses, Crystal Structures and Optical Properties. *J. Solid State Chem.* **2015**, *227*, 104–109. https://doi.org/10.1016/j.jssc.2015.03.013.

(14) Khan, W.; Hussain, S.; Minar, J.; Azam, S. Electronic and Thermoelectric Properties of Ternary Chalcohalide Semiconductors: First Principles Study. *J. Electron. Mater.* **2018**, *47* (2), 1131–1139. https://doi.org/10.1007/s11664-017-5884-z.

(15) Krebs, B. Die Kristallstrukturen von Pb4SeBr6, Pb5S2J6 Und Pb7S2Br10. *ZAAC - J. Inorg. Gen. Chem.* **1973**, *396* (2), 137–151. https://doi.org/10.1002/zaac.19733960203.

(16) Rabenau, A.; Rau, H. Über Sulfidhalogenide Des Bleis Und Das Pb4SeBr6. *ZAAC - J. Inorg. Gen. Chem.* **1969**, *369* (3–6), 295–305. https://doi.org/10.1002/zaac.19693690319.

(17) Karaoglanov, Z. Ursachen Für Die Verunreinigung von Niederschlägen. II. Fällungsvorgänge, an Denen Sich Bleiverbindungen Beteiligen. *Fresenius' Zeitschrift für Anal. ChemieZeitschrift für Anal. Chemie* **1936**, *106* (7–8), 262–272. https://doi.org/10.1007/bf01395088.

(18) Karaoglanov, Z. Empfindlichkeit Des Nachweises von Blei- Und Sulfid-Ion Als Bleisulfobromid [(PbBr)2S]. *Zeitschrift für Anal. Chemie* **1939**, *118* (9–10), 311–322. https://doi.org/10.1007/BF01358439.

(19) Victor Lenher, B. *The Sulphohalides Of Lead*; Vol. 7.

(20) Ni, D.; Guo, S.; Powderly, K. M.; Zhong, R.; Cava, R. J. A High-Pressure Phase with a Non-Centrosymmetric Crystal Structure in the PbSe–PbBr2 System. *J. Solid State Chem.* **2019**, *280*. https://doi.org/10.1016/j.jssc.2019.120982.

(21) Ni, D.; Guo, S.; Yang, Z. S.; Powderly, K. M.; Cava, R. J. Pb 4 S 3 I 2 –A High-Pressure Phase in the PbS-PbI 2 System. *Solid State Sci.* **2019**, *91*, 49–53. https://doi.org/10.1016/j.solidstatesciences.2019.03.012.

(22) Yun, Y.; Zou, X.; Hovmöller, S.; Wan, W. Three-Dimensional Electron Diffraction as a Complementary Technique to Powder X-Ray Diffraction for Phase Identification and Structure Solution of Powders. *IUCrJ* **2015**, *2*, 267–282. https://doi.org/10.1107/S2052252514028188.

(23) Gemmi, M.; Mugnaioli, E.; Gorelik, T. E.; Kolb, U.; Palatinus, L.; Boullay, P.; Hovmöller, S.; Abrahams, J. P. 3D Electron Diffraction: The Nanocrystallography Revolution. *ACS Cent. Sci.* **2019**, *5* (8), 1315–1329. https://doi.org/10.1021/acscentsci.9b00394.

(24) Kaiukov, R.; Almeida, G.; Marras, S.; Dang, Z.; Baranov, D.; Petralanda, U.; Infante, I.; Mugnaioli, E.; Griesi, A.; De Trizio, L.; et al. Cs3Cu4In2Cl13 Nanocrystals: A Perovskite-Related Structure with Inorganic Clusters at A Sites. *Inorg. Chem.* **2019**, *59* (1), 548–554.

https://doi.org/10.1021/acs.inorgchem.9b02834.

(25) Mugnaioli, E.; Gemmi, M.; Tu, R.; David, J.; Bertoni, G.; Gaspari, R.; De Trizio, L.; Manna, L. Ab Initio Structure Determination of Cu2- XTe Plasmonic Nanocrystals by Precession-Assisted Electron Diffraction Tomography and HAADF-STEM Imaging. *Inorg. Chem.* **2018**, *57* (16), 10241–10248. https://doi.org/10.1021/acs.inorgchem.8b01445.

(26) Akkerman, Q. A.; García, B. M.; Buha, J.; Almeida, G.; Toso, S.; Marras, S.; Bonaccorso, F.; Petralanda, U.; Infante, I.; Manna, L. Ultrathin Orthorhombic PbS Nanosheets. *Chem. Mater.* **2019**. https://doi.org/10.1021/acs.chemmater.9b02914.

(27) Gemmi, M.; Lanza, A. E. 3D Electron Diffraction Techniques. *Acta Crystallogr. Sect. B Struct. Sci. Cryst. Eng. Mater.* **2019**, *75* (4), 495–504. https://doi.org/10.1107/S2052520619007510.

(28) Vincent, R.; Midgley, P. A. Double Conical Beam-Rocking System for Measurement of Integrated Electron Diffraction Intensities. *Ultramicroscopy* **1994**, *53* (3), 271–282. https://doi.org/10.1016/0304-3991(94)90039-6.

(29) Mugnaioli, E.; Gorelik, T.; Kolb, U. "Ab Initio" Structure Solution from Electron Diffraction Data Obtained by a Combination of Automated Diffraction Tomography and Precession Technique. *Ultramicroscopy* **2009**, *109* (6), 758–765. https://doi.org/10.1016/j.ultramic.2009.01.011.

(30) Kolb, U.; Krysiak, Y.; Plana-Ruiz, S. Automated Electron Diffraction Tomography - Development and Applications. *Acta Crystallogr. Sect. B Struct. Sci. Cryst. Eng. Mater.* **2019**, *75* (4), 463–474. https://doi.org/10.1107/S2052520619006711.

(31) Palatinus, L.; Brázda, P.; Jelínek, M.; Hrdá, J.; Steciuk, G.; Klementová, M. Specifics of the Data Processing of Precession Electron Diffraction Tomography Data and Their Implementation in the Program PETS2.0. *Acta Crystallogr. Sect. B Struct. Sci. Cryst. Eng. Mater.* **2019**, *75* (4), 512–522. https://doi.org/10.1107/S2052520619007534.

(32) Burla, M. C.; Caliandro, R.; Carrozzini, B.; Cascarano, G. L.; Cuocci, C.; Giacovazzo, C.; Mallamo, M.; Mazzone, A.; Polidori, G. Crystal Structure Determination and Refinement via SIR2014. *J. Appl. Crystallogr.* **2015**, *48* (1), 306–309. https://doi.org/10.1107/S1600576715001132.

(33) Altantzis, T.; Lobato, I.; De Backer, A.; Béché, A.; Zhang, Y.; Basak, S.; Porcu, M.; Xu, Q.; Sánchez-Iglesias, A.; Liz-Marzán, L. M.; et al. Three-Dimensional Quantification of the Facet Evolution of Pt Nanoparticles in a Variable Gaseous Environment. *Nano Lett.* **2019**, *19* (1), 477–481. https://doi.org/10.1021/acs.nanolett.8b04303.

(34) Gilbert, P. Iterative Methods for the Three-Dimensional Reconstruction of an Object from Projections. *J. Theor. Biol.* **1972**, *36* (1), 105–117. https://doi.org/10.1016/0022-5193(72)90180-4.

(35) Altomare, A.; Cuocci, C.; Giacovazzo, C.; Moliterni, A.; Rizzi, R.; Corriero, N.; Falcicchio, A. EXPO2013: A Kit of Tools for Phasing Crystal Structures from Powder Data. *J. Appl. Crystallogr.* **2013**, *46* (4), 1231–1235. https://doi.org/10.1107/S0021889813013113.

(36) Altomare, A.; Campi, G.; Cuocci, C.; Eriksson, L.; Giacovazzo, C.; Moliterni, A.; Rizzi, R.; Werner, P. E. Advances in Powder Diffraction Pattern Indexing: N-TREOR09. *J. Appl. Crystallogr.* **2009**, *42* (5), 768–775. https://doi.org/10.1107/S0021889809025503.

(37) Giacovazzo, C. *Phasing in Crystallography: A Modern Perspective*; Oxford University Press, 2014.

(38) Rodriguez-Carvajal J. Abstracts of the Satellite Meeting on Powder Diffraction of the XV Congress of the IUCr. In *A Program for rietveld refinement and pattern matching analysis*; 1990; pp 127–128.

(39) Giannini, C.; Ladisa, M.; Altamura, D.; Siliqi, D.; Sibillano, T.; De Caro, L. X-Ray Diffraction: A Powerful Technique for the Multiple-Length-Scale Structural Analysis of Nanomaterials. *Crystals*. MDPI AG August 4, 2016, p 87. https://doi.org/10.3390/cryst6080087.

(40) Kresse, G.; Furthmüller, J. Efficient Iterative Schemes for Ab Initio Total-Energy Calculations Using a Plane-Wave Basis Set. *Phys. Rev. B - Condens. Matter Mater. Phys.* **1996**, *54* (16), 11169–11186. https://doi.org/10.1103/PhysRevB.54.11169.

(41) Perdew, J. P.; Burke, K.; Ernzerhof, M. Generalized Gradient Approximation Made Simple. *Phys. Rev. Lett.* **1996**, *77* (18), 3865–3868. https://doi.org/10.1103/PhysRevLett.77.3865.

(42) Momma, K.; Izumi, F. VESTA: A Three-Dimensional Visualization System for Electronic and Structural Analysis. *J. Appl. Crystallogr.* **2008**, *41* (3), 653–658. https://doi.org/10.1107/S0021889808012016.

(43) MacRae, C. F.; Sovago, I.; Cottrell, S. J.; Galek, P. T. A.; McCabe, P.; Pidcock, E.; Platings, M.; Shields, G. P.; Stevens, J. S.; Towler, M.; et al. Mercury 4.0: From Visualization to Analysis, Design and Prediction. *J. Appl. Crystallogr.* **2020**, *53* (1), 226–235. https://doi.org/10.1107/S1600576719014092.

(44) Helander, M. G.; Greiner, M. T.; Wang, Z. B.; Lu, Z. H. Pitfalls in Measuring Work Function Using Photoelectron Spectroscopy. *Appl. Surf. Sci.* **2010**, *256* (8), 2602–2605. https://doi.org/10.1016/j.apsusc.2009.11.002.

(45) Calloni, A.; Abate, A.; Bussetti, G.; Berti, G.; Yivlialin, R.; Ciccacci, F.; Duò, L. Stability of Organic Cations in Solution-Processed CH3NH3PbI3 Perovskites: Formation of Modified Surface Layers. *J. Phys. Chem. C* **2015**, *119* (37), 21329–21335. https://doi.org/10.1021/acs.jpcc.5b05422.

(46) Stubhan, T.; Litzov, I.; Li, N.; Salinas, M.; Steidl, M.; Sauer, G.; Forberich, K.; Matt, G. J.; Halik, M.; Brabec, C. J. Overcoming Interface Losses in Organic Solar Cells by Applying Low Temperature, Solution Processed Aluminum-Doped Zinc Oxide Electron Extraction Layers. *J. Mater. Chem. A* **2013**, *1* (19), 6004–6009. https://doi.org/10.1039/c3ta10987a.

(47) Palazon, F.; Dogan, S.; Marras, S.; Locardi, F.; Nelli, I.; Rastogi, P.; Ferretti, M.; Prato, M.; Krahne, R.; Manna, L. From CsPbBr3 Nano-Inks to Sintered CsPbBr3-CsPb2Br5 Films via Thermal Annealing: Implications on Optoelectronic Properties. *J. Phys. Chem. C* **2017**, *121* (21), 11956–11961. https://doi.org/10.1021/acs.jpcc.7b03389.

(48) Knowles, L. M. Thermal Analysis of the System PbBr2-PbO. *J. Chem. Phys.* **1951**, *19* (9), 1128–1130. https://doi.org/10.1063/1.1748489.

(49) Iizuka, A.; Shibata, E.; Sato, M.; Nakamura, T. Vapor Pressure Measurements of PbBr2 by the Knudsen Effusion Method and Identification of Its Vapor Species. *Thermochim. Acta* **2015**, *622*, 103–106. https://doi.org/10.1016/j.tca.2015.10.014.

(50) Nafees, M.; Ikram, M.; Ali, S. Thermal Stability of Lead Sulfide and Lead Oxide Nano-Crystalline Materials. *Appl. Nanosci.* **2017**, *7* (7), 399–406. https://doi.org/10.1007/s13204-017-0578-7.

(51) Tong, Y.; Bladt, E.; Aygüler, M. F.; Manzi, A.; Milowska, K. Z.; Hintermayr, V. A.; Docampo, P.; Bals, S.; Urban, A. S.; Polavarapu, L.; et al. Highly Luminescent Cesium Lead Halide Perovskite Nanocrystals with Tunable Composition and Thickness by Ultrasonication. *Angew. Chemie - Int. Ed.* **2016**, *55* (44), 13887–13892. https://doi.org/10.1002/anie.201605909.

(52) Dang, Z.; Shamsi, J.; Palazon, F.; Imran, M.; Akkerman, Q. A.; Park, S.; Bertoni, G.; Prato, M.; Brescia, R.; Manna, L. In Situ Transmission Electron Microscopy Study of Electron Beam-Induced Transformations in Colloidal Cesium Lead Halide Perovskite Nanocrystals. *ACS Nano* **2017**, *11* (2), 2124–2132. https://doi.org/10.1021/acsnano.6b08324.

(53) Palatinus, L.; Corrêa, C. A.; Steciuk, G.; Jacob, D.; Roussel, P.; Boullay, P.; Klementová, M.; Gemmi, M.; Kopeček, J.; Domeneghetti, M. C.; et al. Structure Refinement Using Precession Electron Diffraction Tomography and Dynamical Diffraction: Tests on Experimental Data. *Acta Crystallogr. Sect. B Struct. Sci. Cryst. Eng. Mater.* **2015**, *71* (6), 740–751. https://doi.org/10.1107/S2052520615017023.

(54) Giannini, C.; Holy, V.; De Caro, L.; Mino, L.; Lamberti, C. Watching Nanomaterials with X-Ray Eyes: Probing Different Length Scales by Combining Scattering with Spectroscopy. *Prog. Mater. Sci.* **2020**, 100667. https://doi.org/10.1016/j.pmatsci.2020.100667.

(55) Plekhanov, V. G. Investigation of the Reflectance Spectra of PbCl2 and PbBr2 Single Crystals with Orthorhombic Structure. *Phys. status solidi* **1975**, *68* (1), K35–K38. https://doi.org/10.1002/pssb.2220680155.

(56) Saran, R.; Curry, R. J. Lead Sulphide Nanocrystal Photodetector Technologies. *Nature Photonics*. Nature Publishing Group February 1, 2016, pp 81–92. https://doi.org/10.1038/nphoton.2015.280.

(57) Moreels, I.; Justo, Y.; De Geyter, B.; Haustraete, K.; Martins, J. C.; Hens, Z. Size-Tunable, Bright, and Stable PbS Quantum Dots: A Surface Chemistry Study. *ACS Nano* **2011**, *5* (3), 2004–2012. https://doi.org/10.1021/nn103050w.

(58) Baerends, E. J. Density Functional Approximations for Orbital Energies and Total Energies of Molecules and Solids. *J. Chem. Phys.* **2018**, *149* (5), 054105. https://doi.org/10.1063/1.5026951.

(59) Giansante, C.; Infante, I.; Fabiano, E.; Grisorio, R.; Suranna, G. P.; Gigli, G. "darker-than-Black" PbS Quantum Dots: Enhancing Optical Absorption of Colloidal Semiconductor Nanocrystals via Short Conjugated

Ligands. *J. Am. Chem. Soc.* **2015**, *137* (5), 1875–1886. https://doi.org/10.1021/ja510739q.

(60) Brown, P. R.; Kim, D.; Lunt, R. R.; Zhao, N.; Bawendi, M. G.; Grossman, J. C.; Bulović, V. Energy Level Modification in Lead Sulfide Quantum Dot Thin Films through Ligand Exchange. *ACS Nano* **2014**, *8* (6), 5863–5872. https://doi.org/10.1021/nn500897c.

(61) Brown, P. R.; Lunt, R. R.; Zhao, N.; Osedach, T. P.; Wanger, D. D.; Chang, L. Y.; Bawendi, M. G.; Bulović, V. Improved Current Extraction from ZnO/PbS Quantum Dot Heterojunction Photovoltaics Using a MoO3 Interfacial Layer. *Nano Lett.* **2011**, *11* (7), 2955–2961. https://doi.org/10.1021/nl201472u.

(62) Bi, Y.; Pradhan, S.; Akgul, M. Z.; Gupta, S.; Stavrinadis, A.; Wang, J.; Konstantatos, G. Colloidal Quantum Dot Tandem Solar Cells Using Chemical Vapor Deposited Graphene as an Atomically Thin Intermediate Recombination Layer. *ACS Energy Lett.* **2018**, *3* (7), 1753–1759. https://doi.org/10.1021/acsenergylett.8b00675.

(63) Liu, F.; Shao, S.; Guo, X.; Zhao, Y.; Xie, Z. Efficient Polymer Photovoltaic Cells Using Solution-Processed MoO3 as Anode Buffer Layer. *Sol. Energy Mater. Sol. Cells* **2010**, *94* (5), 842–845. https://doi.org/10.1016/j.solmat.2010.01.004.

(64) Bala, T.; Prasad, B. L. V.; Sastry, M.; Kahaly, M. U.; Waghmare, U. V. Interaction of Different Metal Ions with Carboxylic Acid Group: A Quantitative Study. *J. Phys. Chem. A* **2007**, *111* (28), 6183–6190. https://doi.org/10.1021/jp067906x.

(65) Koh, W. K.; Saudari, S. R.; Fafarman, A. T.; Kagan, C. R.; Murray, C. B. Thiocyanate-Capped PbS Nanocubes: Ambipolar Transport Enables Quantum Dot Based Circuits on a Flexible Substrate. *Nano Lett.* **2011**, *11* (11), 4764–4767. https://doi.org/10.1021/nl202578g.

(66) Rosina, I.; Martin-Garcìa, B.; Davide, S.; Dang, Z.; Gariano, G.; Marras, S.; Prato, M.; Krahne, R.; De Trizio, L.; Manna, L. Metastable CdTe@HgTe Core@shell Nanostructures Obtained by Partial Cation Exchange Evolve into Sintered CdTe Films Upon Annealing, under Revision in Chemistry of Materials. *Chem. Mater.* **2020**, acs.chemmater.9b05281. https://doi.org/10.1021/acs.chemmater.9b05281.

(67) Chui, C. O.; Okyay, A. K.; Saraswat, K. C. Effective Dark Current Suppression with Asymmetric MSM Photodetectors in Group IV Semiconductors. *IEEE Photonics Technol. Lett.* **2003**, *15* (11), 1585–1587. https://doi.org/10.1109/LPT.2003.818683.

(68) Wang, H.; Kim, D. H. Perovskite-Based Photodetectors: Materials and Devices. *Chemical Society Reviews*. Royal Society of Chemistry September 7, 2017, pp 5204–5236. https://doi.org/10.1039/c6cs00896h.

(69) García De Arquer, F. P.; Armin, A.; Meredith, P.; Sargent, E. H. Solution-Processed Semiconductors for next-Generation Photodetectors. *Nature Reviews Materials*. Nature Publishing Group January 24, 2017. https://doi.org/10.1038/natrevmats.2016.100.

(70) Wang, Y.; Song, L.; Chen, Y.; Huang, W. Emerging New-Generation Photodetectors Based on Low-Dimensional Halide Perovskites. *ACS Photonics* **2020**, *7* (1), 10–28. https://doi.org/10.1021/acsphotonics.9b01233.

(71) Behnam, A.; Johnson, J. L.; Choi, Y.; Ertosun, M. G.; Okyay, A. K.; Kapur, P.; Saraswat, K. C.; Ural, A. Experimental Characterization of Single-Walled Carbon Nanotube Film-Si Schottky Contacts Using Metal-Semiconductor-Metal Structures. *Appl. Phys. Lett.* **2008**, *92* (24). https://doi.org/10.1063/1.2945644.

(72) An, Y.; Behnam, A.; Pop, E.; Ural, A. Metal-Semiconductor-Metal Photodetectors Based on Graphene/p-Type Silicon Schottky Junctions. *Appl. Phys. Lett.* **2013**, *102* (1). https://doi.org/10.1063/1.4773992.

(73) Das, M.; Sarmah, S.; Sarkar, D. UV-Visible Optical Photo-Detection from Porous Silicon (PS) MSM Device. *Superlattices Microstruct.* **2017**, *101*, 228–235. https://doi.org/10.1016/j.spmi.2016.11.052.

(74) Xia, Z.; Song, H.; Kim, M.; Zhou, M.; Chang, T. H.; Liu, D.; Yin, X.; Xiong, K.; Mi, H.; Wang, X.; et al. Single-Crystalline Germanium Nanomembrane Photodetectors on Foreign Nanocavities. *Sci. Adv.* **2017**, *3* (7). https://doi.org/10.1126/sciadv.1602783.

(75) Sanehira, E. M.; Marshall, A. R.; Christians, J. A.; Harvey, S. P.; Ciesielski, P. N.; Wheeler, L. M.; Schulz, P.; Lin, L. Y.; Beard, M. C.; Luther, J. M. Enhanced Mobility CsPbI3 Quantum Dot Arrays for Record-Efficiency, High-Voltage Photovoltaic Cells. *Sci. Adv.* **2017**, *3* (10), eaao4204. https://doi.org/10.1126/sciadv.aao4204.

(76) Zhang, H.; Kurley, J. M.; Russell, J. C.; Jang, J.; Talapin, D. V. Solution-Processed, Ultrathin Solar Cells from CdCl3--Capped CdTe Nanocrystals: The Multiple Roles of CdCl3- Ligands. *J. Am. Chem. Soc.* **2016**, *138* (24), 7464–7467. https://doi.org/10.1021/jacs.6b03240.

(77) Lin, D. Y.; Guo, B. C.; Dai, Z. Y.; Lin, C. F.; Hsu, H. P. Pbi2 Single Crystal Growth and Its Optical Property Study. *Crystals* **2019**, *9* (11), 589. https://doi.org/10.3390/cryst9110589.

(78) Wang, R.; Li, S.; Wang, P.; Xiu, J.; Wei, G.; Sun, M.; Li, Z.; Liu, Y.; Zhong, M. PbI2 Nanosheets for Photodetectors via the Facile Cooling Thermal Supersaturation Solution Method. *J. Phys. Chem. C* **2019**, *123* (14), 9609–9616. https://doi.org/10.1021/acs.jpcc.9b01322.

(79) Kang, I.; Wise, F. W. Electronic Structure and Optical Properties of PbS and PbSe Quantum Dots. *J. Opt. Soc. Am. B* **1997**, *14* (7), 1632. https://doi.org/10.1364/josab.14.001632.

(80) Okuno, T.; Lipovskii, A. A.; Ogawa, T.; Amagai, I.; Masumoto, Y. Strong Confinement of PbSe and PbS Quantum Dots. *J. Lumin.* **2000**, *87*, 491–493. https://doi.org/10.1016/S0022-2313(99)00220-3.

(81) Yuan, L.; Patterson, R.; Cao, W.; Zhang, Z.; Zhang, Z.; Stride, J. A.; Reece, P.; Conibeer, G.; Huang, S. Air-Stable PbS Quantum Dots Synthesized with Slow Reaction Kinetics via a PbBr2 Precursor. *RSC Adv.* **2015**, *5* (84), 68579–68586. https://doi.org/10.1039/c5ra13499d.

(82) Zhang, J.; Gao, J.; Miller, E. M.; Luther, J. M.; Beard, M. C. Diffusion-Controlled Synthesis of PbS and PbSe Quantum Dots with in Situ Halide Passivation for Quantum Dot Solar Cells. *ACS Nano* **2014**, *8* (1), 614–622. https://doi.org/10.1021/nn405236k.

(83) Winslow, S. W.; Liu, Y.; Swan, J. W.; Tisdale, W. A. Quantification of a PbCl x Shell on the Surface of PbS Nanocrystals. *ACS Mater. Lett.* **2019**, *1* (2), 209–216. https://doi.org/10.1021/acsmaterialslett.9b00200.

(84) Green, P. B.; Li, Z.; Wilson, M. W. B. PbS Nanocrystals Made with Excess PbCl2 Have an Intrinsic Shell That Reduces Their Stokes Shift. *J. Phys. Chem. Lett.* **2019**, *10* (19), 5897–5901. https://doi.org/10.1021/acs.jpclett.9b01841.

(85) Brittman, S.; Colbert, A. E.; Brintlinger, T. H.; Cunningham, P. D.; Stewart, M. H.; Heuer, W. B.; Stroud, R. M.; Tischler, J. G.; Boercker, J. E. Effects of a Lead Chloride Shell on Lead Sulfide Quantum Dots. *J. Phys. Chem. Lett.* **2019**, *10* (8), 1914–1918. https://doi.org/10.1021/acs.jpclett.9b00786.

Supporting Information for:

Nanocrystals of Lead Chalcohalides: A Series of Kinetically-Trapped Metastable Nanostructures

Stefano Toso[†Δ,∇], Quinten A. Akkerman[†Φ,∇], Beatriz Martín-García[†Γ,∇], Mirko Prato[Σ], Juliette Zito[†], Ivan Infante[†§*], Zhiya Dang[†Θ], Anna Moliterni[‡*], Cinzia Giannini[‡], Eva Bladt[Ϫ┼], Ivan Lobato[Ϫ┼], Julien Ramade[Ϫ┼], Sara Bals[Ϫ┼*], Joka Buha[†], Davide Spirito[†ϟ], Enrico Mugnaioli[⊥], Mauro Gemmi[⊥*], Liberato Manna[†*]

[†] Department of Nanochemistry, [Σ] Materials Characterization Facility, Istituto Italiano di Tecnologia, Via Morego 30, 16163 Genova, Italy

[Δ] Dipartimento di Matematica e Fisica and Interdisciplinary Laboratories for Advanced Materials Physics, Università Cattolica del Sacro Cuore, via Musei 41, I-25121 Brescia, Italy

[§] Department of Theoretical Chemistry, Faculty of Science, Vrije Universiteit Amsterdam, de Boelelaan 1083, 1081 HV Amsterdam, The Netherlands

[‡] Istituto di Cristallografia - Consiglio Nazionale delle Ricerche (IC-CNR), via Amendola 122/O, I-70126 Bari, Italy

[Ϫ] Electron Microscopy for Materials Science (EMAT), University of Antwerp, Groenenborgerlaan 171, 2020 Antwerp, Belgium

[┼] NANOlab Center of Excellence, University of Antwerp, Belgium

[⊥] Center for Nanotechnology Innovation@NEST, Istituto Italiano di Tecnologia, Piazza San Silvestro, 12, 56127, Pisa, Italy

*E-mail: ivan.infante@iit.it, annagrazia.moliterni@ic.cnr.it, sara.bals@uantwerpen.be, mauro.gemmi@iit.it, liberato.manna@iit.it

Present Address:

[Φ] Department of Chemistry and Applied Biosciences, ETH Zürich, Vladimir Prelog Weg 1, CH-8093 Zürich, Switzerland

[Γ] CIC nanoGUNE, Tolosa Hiribidea, 76, E-20018 Donostia – San Sebastian, Spain

[ϟ] IHP–Leibniz-Institut für innovative Mikroelektronik, Material Research Semiconductor Optoelectronics, Frankfurt (Oder), Germany

[Θ] School of Materials, Sun Yat-sen University, Guangzhou, 510275, China

Contents:

Support Material

a) Direct synthesis of $Pb_4S_3Br_2$ NCs

The $Pb_4S_3Br_2$ nanocrystals (NCs) used in this work have been synthesized via a modification of the heat-up method previously published by our group.[1] In a standard synthesis, 0.2 mmol of $PbBr_2$ and 0.2 mmol of $Pb(SCN)_2$ were dissolved in a mixture of 10 mL ODE and 250 µL of OLAM and OA at 110°C in a 25 mL three-necked flask. This temperature was not exceeded during the solubilization, to avoid triggering the thermal decomposition of SCN^- ions. Once the two solids were completely dissolved the solution appeared clear and pale-yellow. At that point, the flask was lifted from the heating-mantle, which was overheated to an inner temperature of 250°C to grant the fast increase of temperature required for the synthesis. The flask, till that point kept at ≈110°C by hovering it at the rim of the mantle, was again inserted and as a result the solution quickly heated up (≈ 20°C / min), consequently turning from light-yellow to bloody red above 150°C. As reported in our previous paper, the following reaction is taking place:[1]

$$2\ SCN^- + 3O_2 \rightarrow S^{2-} + SO_2 + 2\ CO_2 + N_2$$

As a consequence, S^{2-} becomes suddenly available in the reaction system and co-precipitates with Pb^{2+} and Br^- forming the reported $Pb_4S_3Br_2$ phase.

Figure S1. Timeline of the reaction for the synthesis of $Pb_4S_3Br_2$ NCs by direct observation of aliquots collecting during the synthesis. Many aliquots of the reaction batch were taken using a syringe and immediately quenched by immersing the vial in a water bath. The quenching temperature increases from left to right, as reported in °C on each vial.

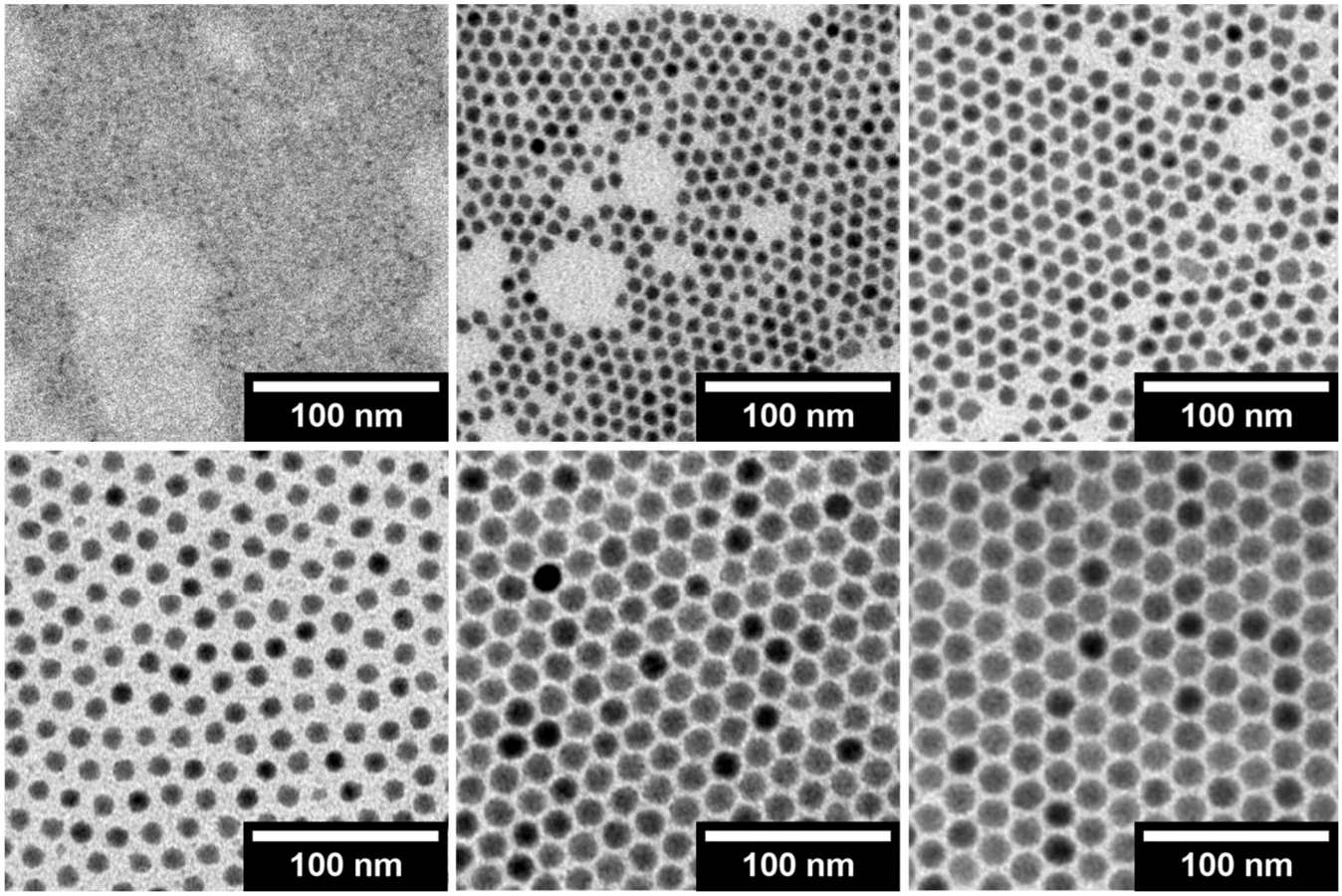

Figure S2. Timeline of the reaction for the synthesis of $Pb_4S_3Br_2$ NCs by TEM. The samples shown here come from the series in Figure S1. The quenching temperature increases from left to right and from top to bottom: 150 – 160 – 165 – 170 – 180 – 190°C.

Table S1. Timeline of the reaction by TEM. Table summarizing the size and size dispersion of $Pb_4S_3Br_2$ NCs obtained by quenching the reaction at different temperatures, together with the time elapsed between the start of sample heating and the quenching.

Quenching Temperature (°C)	Time after heating started (s)	Size ± distribution FWHM (nm)
120	0	no particles
130	28	no particles
140	50	no particles
150	75	no particles
155	88	not measured
160	102	7.8 ± 0.63
165	117	9.46 ± 0.44
170	148	11.54 ± 0.41
180	166	15.33 ± 0.59
190	182	15.99 ± 1.25

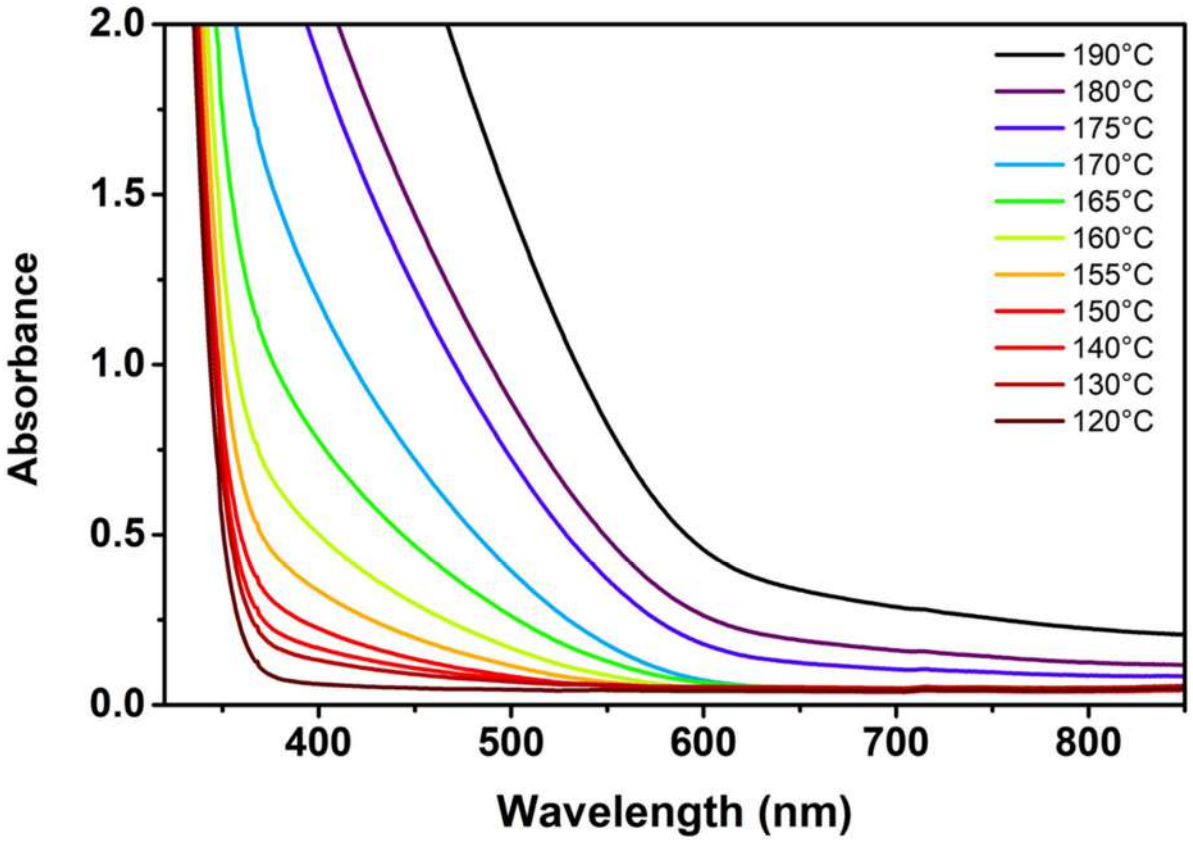

Figure S3. Timeline of the reaction for the synthesis of $Pb_4S_3Br_2$ NCs by optical absorption. Absorption spectra of the aliquots shown in Figure S1. The spectra were not normalized to give additional information on how the absorbance increases while the NCs nucleate and grow. All the samples were prepared by diluting 50 µL of the crude reaction batch in 900 µL of toluene inside a 10 mm-path cuvette. The spectra collected from 175 – 180 – 190°C aliquots show the characteristic effect of scattering, since particles grew too large to form a stable colloidal suspension in toluene once the samples cooled to room temperature and were diluted.

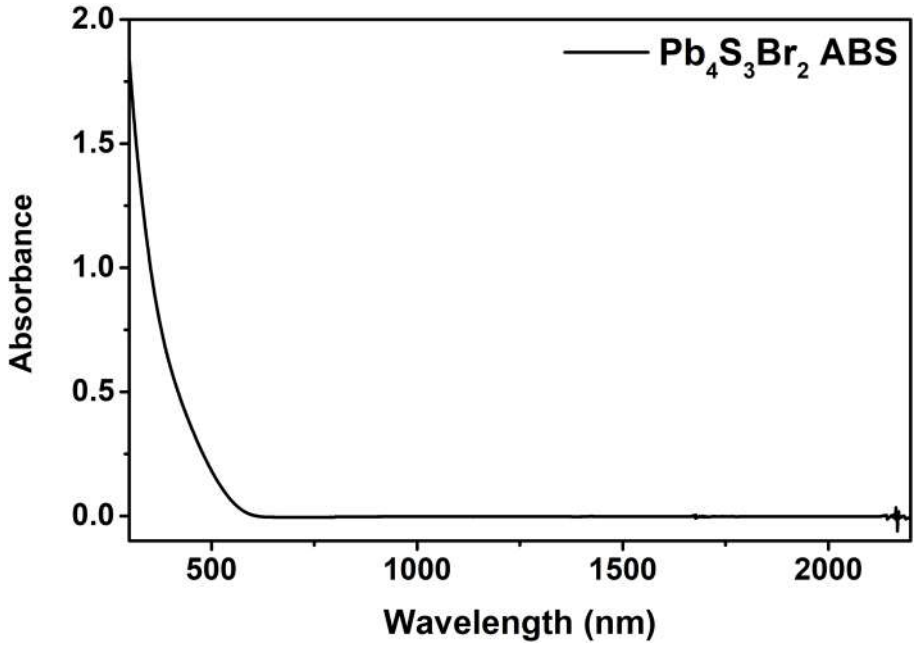

Figure S4. $Pb_4S_3Br_2$ NCs by absorption. Absorption spectrum of $Pb_4S_3Br_2$ NCs extended into the infrared region, demonstrating no absorption beyond ~650 nm.

b) Further accretion of $Pb_4S_3Br_2$ NCs

Large-size $Pb_4S_3Br_2$ NCs were needed to attempt an *ab initio* NC structure solution via single particle 3D-ED. A batch of NCs was synthesized according to the reported procedure, and the growth was quenched at 170°C. The particles were not recovered from the reaction batch; instead, the flask was re-heated to 170°C and kept stirring at this constant temperature. In a separated flask, 0.6 mmol of $PbBr_2$ and 0.6 mmol of $Pb(SCN)_2$ were dissolved in 30 mL of ODE, 750 µL OLAM and 750 µL OA (3× standard synthesis). The procedure was stopped before the heat-up step. Instead, the liquid was filtered with a 0.2 µm PTFE syringe filter and slowly added dropwise to the hot batch of NCs at a rate of 5 mL/h with a syringe pump. This procedure ensured a steady growth of the pre-existing NCs. In our experiment, the NCs grew from an original 13.1 ± 0.48 nm size (batch already hot and stable at 170°C, no further addition) to a final 27.1 ± 1.90 nm size (after 30 mL, 6 h addition).

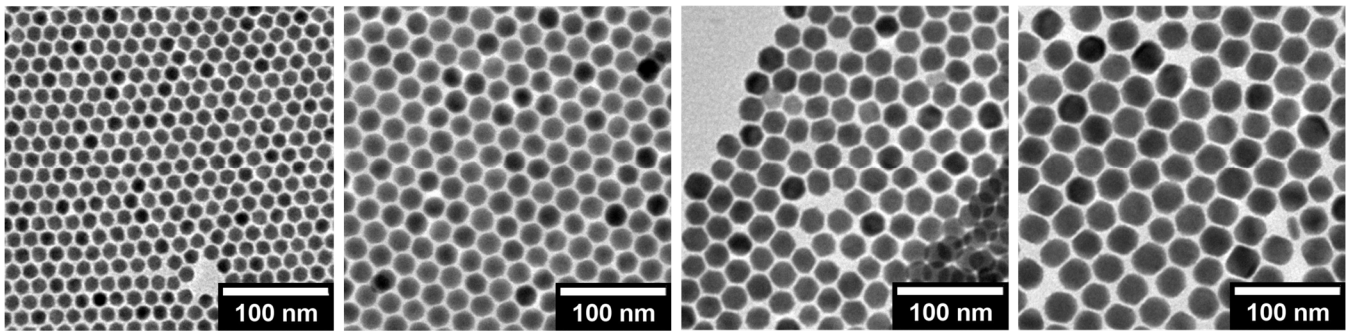

Figure S5. $Pb_4S_3Br_2$ accretion. $Pb_4S_3Br_2$ NCs at various stages of the accretion. From left to right: starting NCs originally quenched at 170°C; NCs after an addition of 7.5 mL; 22.5 mL; 30 mL of the accretion precursor solution.

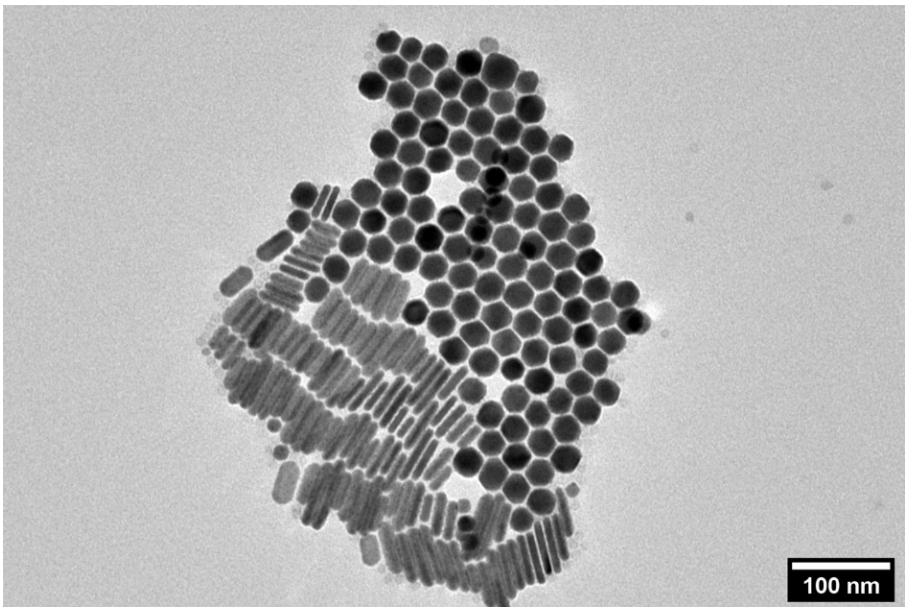

Figure S6. Different $Pb_4S_3Br_2$ morphologies. TEM image showing both the accreted $Pb_4S_3Br_2$ NCs and the $Pb_4S_3Br_2$ nano-platelets which formed as a side-product during the accretion process.

The compositions of both pseudospherical and platelet-shaped NCs were measured via TEM-EDX and were found in good agreement with each other, suggesting that NCs and nanoplatelets share the same stoichiometry. When comparing the two measurements, one must take into account that the two morphologies will be differently affected by the surface termination and preferential growth effects, thus making it unlikely that the overall elemental compositions will be identical for the two different NC morphologies.

Table S2. TEM-EDX on NCs and platelets. Compositional analysis by TEM-EXD for the pseudospherical and platelet-shaped NCs.

	Pb (at. %)	**S (at. %)**	**Br (at. %)**
$Pb_4S_3Br_2$ NCs	45.76 ± 8.85	28.89 ± 0.64	25.37 ± 1.63
$Pb_4S_3Br_2$ nanoplatelets	38.61 ± 8.36	35.20 ± 0.77	26.19 ± 1.80

c) Direct synthesis and structural characterization of $Pb_4S_3I_2$ NCs

Conditions similar to those described in paragraph S1.a where applied for the synthesis of $Pb_4S_3I_2$ NCs: 0.2 mmol of PbI_2 and 0.2 mmol of $Pb(SCN)_2$ where dissolved in a mixture of 10 mL ODE and 250 µL of OLAM and OA at 110°C in a 25 mL three-necked flask. The rest of the procedure remained unchanged. It is noteworthy that the dissolution of PbI_2 was faster than that of $PbBr_2$ and led to an intensely colored yellow solution. NCs formed upon heating up were generally larger than those of $Pb_4S_3Br_2$ (if compared at the same quench temperature, *e.g.* 180°C) and following the centrifugation they were completely recovered, leaving an almost colorless precipitate. The heat-up process causes the NCs to form, even if with the presence of a crystalline impurity which we identified as PbI_2 nanosheets or flakes based on reports in the literature.[2,3]

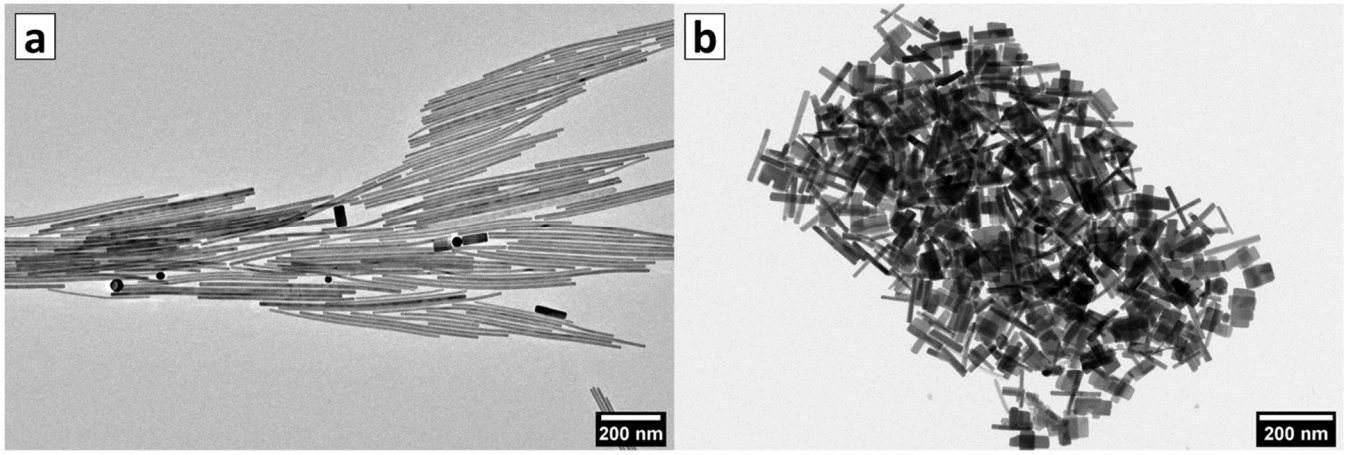

Figure S7. $Pb_4S_3I_2$ NCs. Two of the morphologies obtained for $Pb_4S_3I_2$ nanostructures. Even if the shape and size control was poor, the $Pb_4S_3I_2$ NCs appeared to grow in more anisotropic shapes and to reach larger sizes compared to the $Pb_4S_3Br_2$ NCs.

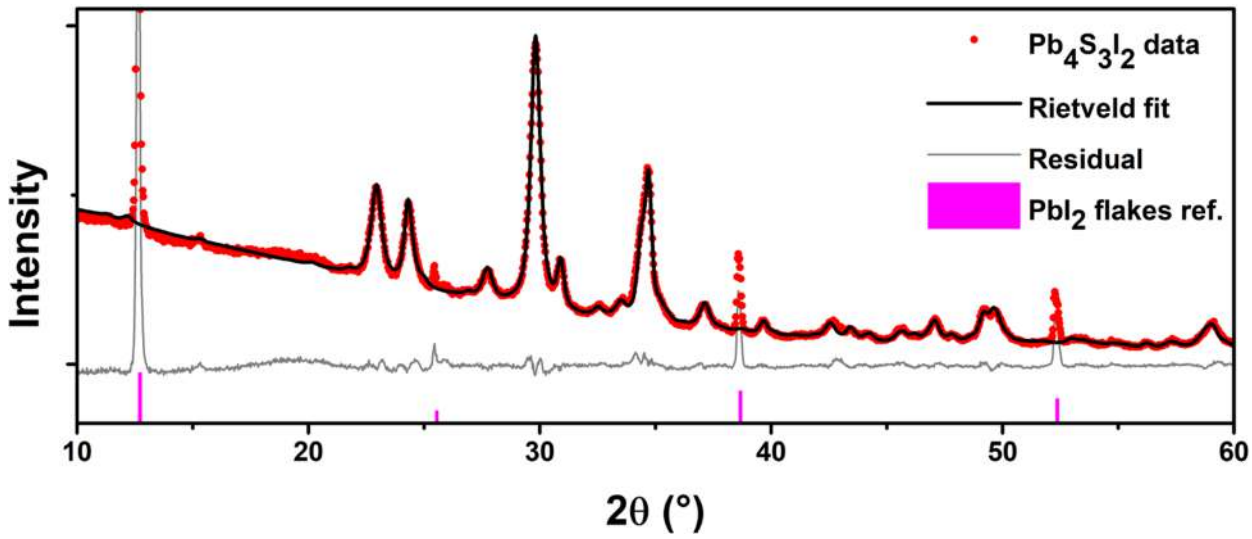

Figure S8. $Pb_4S_3I_2$ XRPD. Rietveld fit of the $Pb_4S_3I_2$ NCs XRPD pattern based on the structural model published by Ni *et. al*.[4] The good fit of the overall profile confirms that we obtained the expected phase, but evidences the presence of a crystalline impurity in non-negligible amounts, clearly indicated by the peaks found in the residual profile. A good match with the pattern of PbI_2 flakes is observed.[3]

Table S3. $Pb_4S_3I_2$ Rietveld fit. Outcome of the Rietveld fit based on the $Pb_4S_3I_2$ structural model published by Ni *et. al*.[4]

Space group	Pnma (no. 62)					
Unit cell parameters	**a (Å)**		**b (Å)**		**c (Å)**	
	8.169		15.648		8.201	
	α (°)		**β (°)**		**γ (°)**	
	90		90		90	
Atomic coordinates	**x**		**y**		**z**	
Pb 1	0.18269		0.06747		0.07378	
Pb 2	0.00957		0.250		0.31804	
Pb 3	0.34420		0.250		0.60805	
S 1	0.33767		0.11501		0.35901	
S 2	0.20698		0.25000		-0.00224	
I 1	0.00909		0.08462		0.65668	
Isotropic Thermal Factors	**B**					
Pb 1	8.67037					
Pb 2	4.40629					
Pb 3	5.75456					
S 1	4.19821					
S 2	0					
I 1	5.34747					
Anisotropic Lorentzian size broadening factors	Y00	Y20	Y22+	Y40	Y42+	Y44+
	5.78980	0.28502	-1.87900	0.31184	-0.79490	-1.95033
Goodness of Fit	9.9					

Note on the fit: the anisotropic broadening factors were included in order to take into account the anisotropic shape observed in NCs under the electron microscope. The relatively high Goodness of Fit parameter (lower is better) depends mainly on the presence of the non-fitted impurity peaks.

d) Direct synthesis and structural characterization of $Pb_3S_2Cl_2$ NCs

Conditions similar to those described in paragraph S1.a where applied for the synthesis of $Pb_3S_2Cl_2$ NCs: 0.2 mmol of PbI_2 and 0.2 mmol of $Pb(SCN)_2$ where dissolved in a mixture of 10 mL ODE and 250 µL of OLAM and OA at 110°C in a 25 mL three-necked flask. The dissolution of $PbCl_2$ was slower than that of $PbBr_2$ and sometimes was incomplete. Thus, we introduced an additional filtering step: we let the batch cool down to ~50°C, decanted it for a few seconds and then filtered the liquid with a 0.2 µm PTFE syringe filter. The clear liquid was then heated up again to 110°C and the procedure continued unchanged. NCs formed upon heating up were generally smaller than those of $Pb_4S_3Br_2$ (if compared at the same quench temperature, *e.g.* 170°C) and were recovered via ethyl-acetate assisted precipitation. One advantage of this approach is that we also eliminated the large PbS NCs that often formed during the synthesis and that were found in the precipitate.

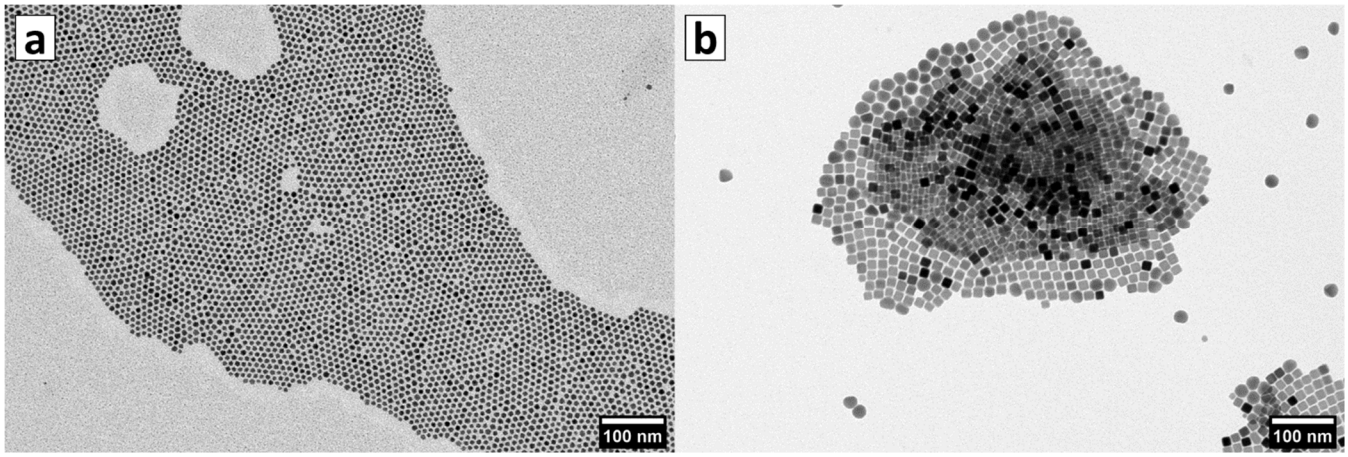

Figure S9. $Pb_3S_2Cl_2$ NCs. a) Smaller $Pb_3S_2Cl_2$ NCs obtained by quenching the reaction at 170°C and recovering the supernatant via ethyl-acetate assisted precipitation and b) rounded $Pb_3S_2Cl_2$ NCs found in the precipitate and heavily contaminated by cubic PbS NCs (both are visible in the image).

Differently from the case of $Pb_4S_3I_2$, no ternary Pb-S-Cl phases matching with our material could be found in crystal structure databases (COD, ICSD). However, an unexpected help in its identification came from the work of Rabenau *et. al.* (dated 1969), in which they reported two tentative new phases, named "2PbS + $PbBr_2$" and "2PbS + $PbCl_2$".[5] According to their report, the first phase was obtained pure in form of a precipitate by first dissolving PbS in concentrated HBr and subsequently diluting the solution with water. They measured its stoichiometry and collected the XRPD pattern but could not solve the structure. The second phase was obtained via a similar protocol, involving HCl instead of HBr, and produced a red precipitate which rapidly decomposed to form a black powder. Thus, they could not collect it pure; however, they measured the XRPD of the mixture, finding that it was mainly composed by PbS but also contained a residual which produced a pattern similar to that of "2PbS + $PbBr_2$". Hence, they hypothesized the existence of a "2PbS + $PbCl_2$" phase. Sixty-one years later, Ni *et. al.* reported the solid-state synthesis

of the high-pressure chalcohalide $Pb_3Se_2Br_2$ (4 GPa, 700°C), which features an equivalent stoichiometry and a pattern very close to that of our chlorine-based NCs[6] (after proper shifting of the peaks to take into account the different sizes of the cells). Figure S10 compares the XRPD we measured that reported for "2PbS + $PbCl_2$" and for $Pb_3Se_2Br_2$, suggesting that we obtained NCs of the $Pb_3S_2Cl_2$ phase that Rabenau *et. al.* hypothesized many years ago.

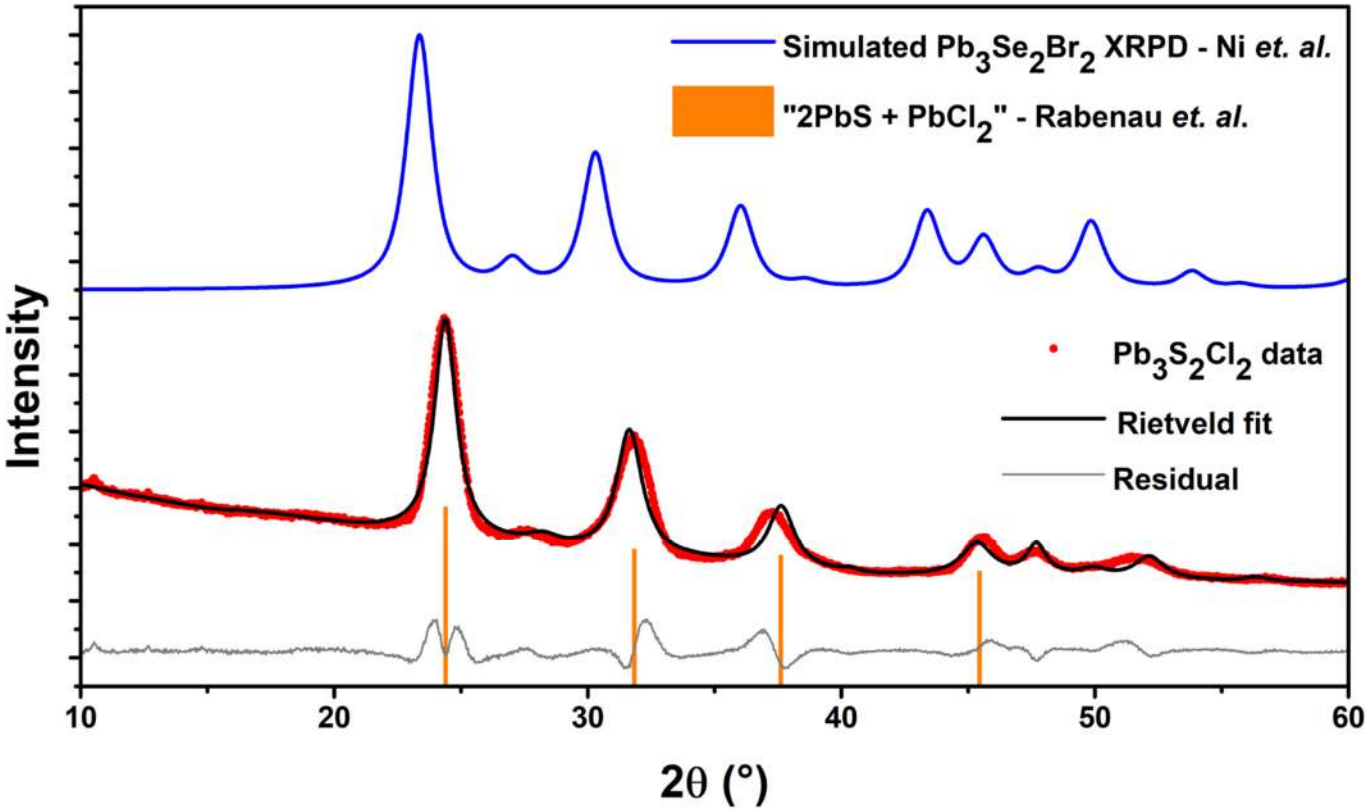

Figure S10. $Pb_3S_2Cl_2$ XRPD. XRPD data from $Pb_3S_2Cl_2$ NCs and corresponding Rietveld fit based on the structural model published by Ni *et.al*.[6] for the phase $Pb_3Se_2Br_2$ The simulated XRPD pattern for the latter and the XRPD lines reported by Rabenau *et.al* for the hypothesized "2PbS + $PbCl_2$" phase are shown for comparison.

Note on the fit: only the unit cell parameters and the scale factor were refined. All the remaining parameters were kept as originally determined by Ni *et.al.* in their work.[6] The overall fit match is good, but the residual indicates that the peaks are slightly misplaced. The cause is most likely a slight distortion from the original cubic symmetry. However, due to the peak broadening the information needed to address this deformation was lost, and we preferred to keep a pseudocubic description for the structure. We plan to investigate this aspect in further specific studies.

Table S4. $Pb_3S_2Cl_2$ Rietveld fit. Outcome of the Rietveld fit on the $Pb_3S_2Cl_2$ XRPD obtained by adapting the $Pb_3Se_2Br_2$ structural model published by Ni. *et. al*.[6]

Space group	Pnma (no. 62)		
Unit cell parameters	**a (Å)**	**b (Å)**	**c (Å)**
	8.202	14.707	8.165
	α (°)	**β (°)**	**γ (°)**
	90	90	90
Goodness of Fit	8.3		

e) XPS analysis on the $Pb_4S_3Br_2$ NCs as synthesized.

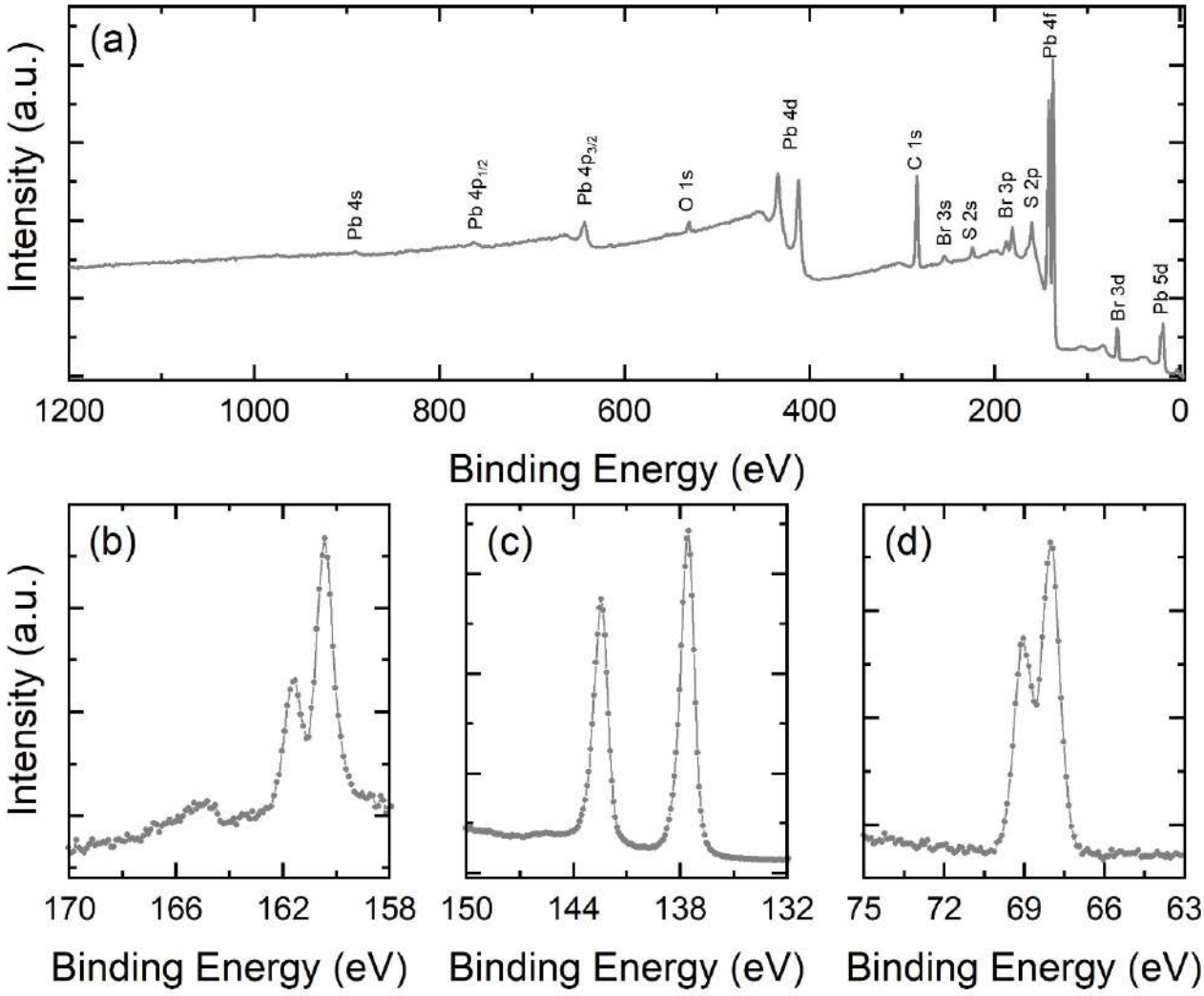

Figure S11. XPS analysis on the $Pb_4S_3Br_2$ NCs as synthesized. a) Wide scan, showing signals due to Pb, S, Br (from the inorganic core of the NCs) together with C and O ones, arising from the organic ligands and possibly also from environmental contaminations, which is common for on samples exposed to moist air. b-d) High resolution scans on the S 2p, Pb 4f and Br 3d energy regions.

Figure S11 reports the XPS data collected on a representative $Pb_4S_3Br_2$ sample. As shown in the wide scan of Figure S11, the sample is characterized by the presence of Pb, S and Br, together with C and O. These last two elements can be attributed to the organic ligand shell surrounding the inorganic core of the as-synthesized NCs. However, we cannot completely exclude the additional presence of environmental contaminations, due to exposure of the sample to moist air before the XPS data acquisition. Figure S11b-d show the high-resolution spectra for the main XPS lines of S, Pb and Br, respectively. The S 2p spectrum in Figure S11b is characterized by an intense doublet on the low binding energy side of the investigated

range (main component centered at 160.4 ± 0.2 eV) and by a low intensity signal in the 165 – 167 eV energy range. The main doublet is in a position close to that reported in literature for sulfides;[7] in particular, sulfur in PbS is typically reported having the main S 2p component at 160.6 ± 0.6 eV. The low intensity signal, instead, is at a position that has been reported for instance for elemental S or for S bound to C in organic molecules,[7] thus suggesting that it could be attributed to synthesis byproducts that were left with the sample after the washing procedure. The Pb 4f spectrum in panel (c) shows the presence of a single doublet, with the main component centered at 137.6 ± 0.2 eV. The position is typical of Pb(II) compounds, and in particular Pb in PbS is typically reported having the main Pb 4f component at 137.8 ± 0.4 eV.[7]The Br 3d spectrum in Figure S11d shows the presence of a single doublet, with the main component centered at 68.0 ± 0.2 eV. This position is typical of bromides.[7]

Similar results were obtained on all the investigated batches; the following table reports the results of the quantitative analysis.

Table S5. XPS analysis on four different batches of $Pb_4S_3Br_2$ NCs as synthesized.

Batch	Pb (at%)	S (at%)	Br (at%)
1	43.30	31.70	25.00
2	42.70	33.70	23.70
3	40.60	32.60	26.80
4	46.80	30.60	22.50
Average	43.35	32.15	24.50
St. dev.	2.23	1.14	1.60

The reported values, together with the oxidation states obtained for Pb, S and Br, point to a $Pb_4S_3Br_2$ stoichiometry for the obtained compound (Pb:S:Br = 44.4:33.4:22.4).

f) EDX analysis on as synthesized $Pb_4S_3Br_2$ NCs.

One of the NC suspensions used to prepare the solar cells was analyzed via SEM-EDX to measure the NCs composition. For the elemental analyses the Pb-L spectral line (10.551 eV) was used instead of the default Pb-M (2.34 eV), which overlaps with the S-K line (2.309 eV). This avoided the need for a deconvolution and produced results in line with those obtained by XPS, in good agreement with the expected $Pb_4S_3Br_2$ stoichiometry (Pb:S:Br = 44.4 : 33.3 : 22.2).

Table S6. SEM-EDX analysis on as synthesized $Pb_4S_3Br_2$ NCs.

Batch	Pb (at%)	S (at%)	Br (at%)
1	43.39	30.71	25.9
2	43.29	30.27	26.43
3	43.46	29.09	27.45
4	42.44	29.29	28.27
Average	43.16	29.84	27.013
St. dev.	0.48	0.78	1.06

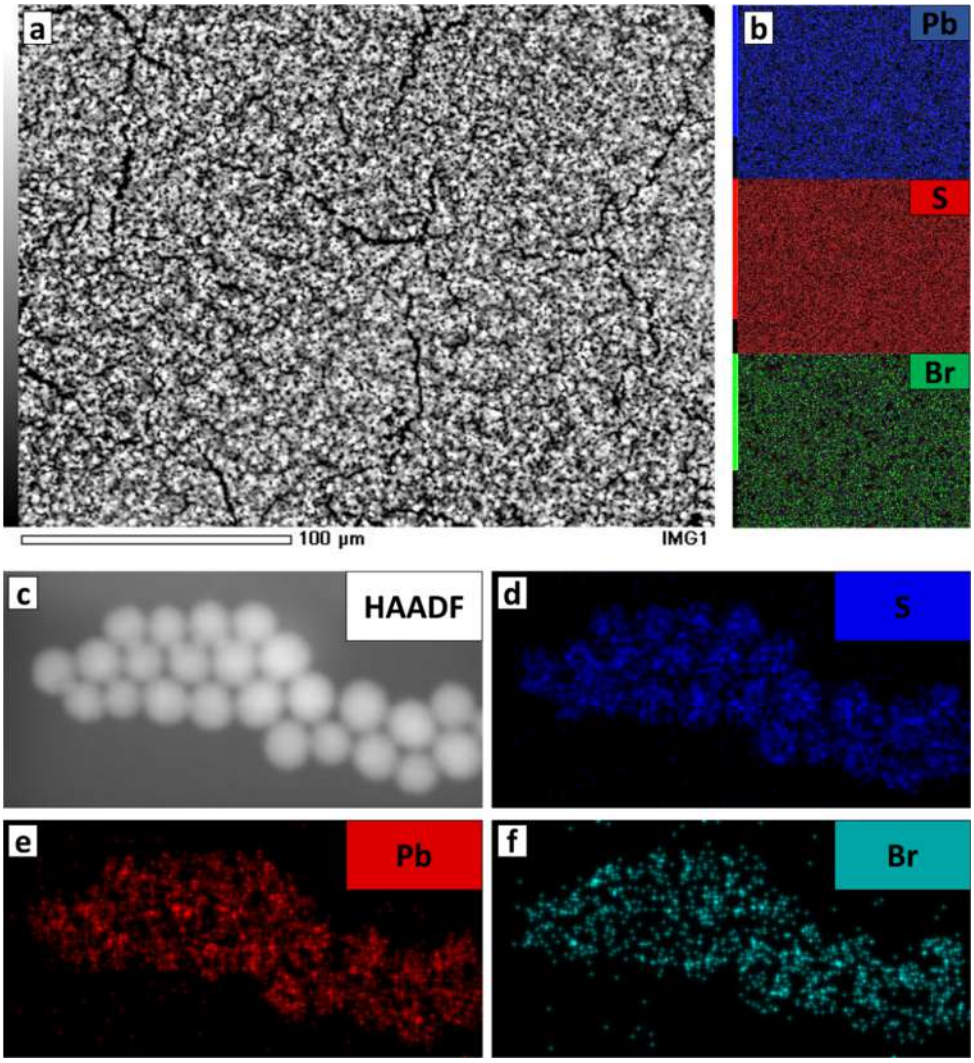

Figure S12. a) Backscattered electrons image of one area of the $Pb_4S_3Br_2$ NCs film prepared for the SEM-EDX elemental analysis, together with b) the corresponding elemental maps. c) HAADF-SEM imaging of a cluster of $Pb_4S_3Br_2$ NCs, together with d-f) the corresponding EDX compositional maps, showing that the elements are uniformly distributed in the NCs.

g) TGA analysis on $Pb_4S_3Br_2$ NCs.

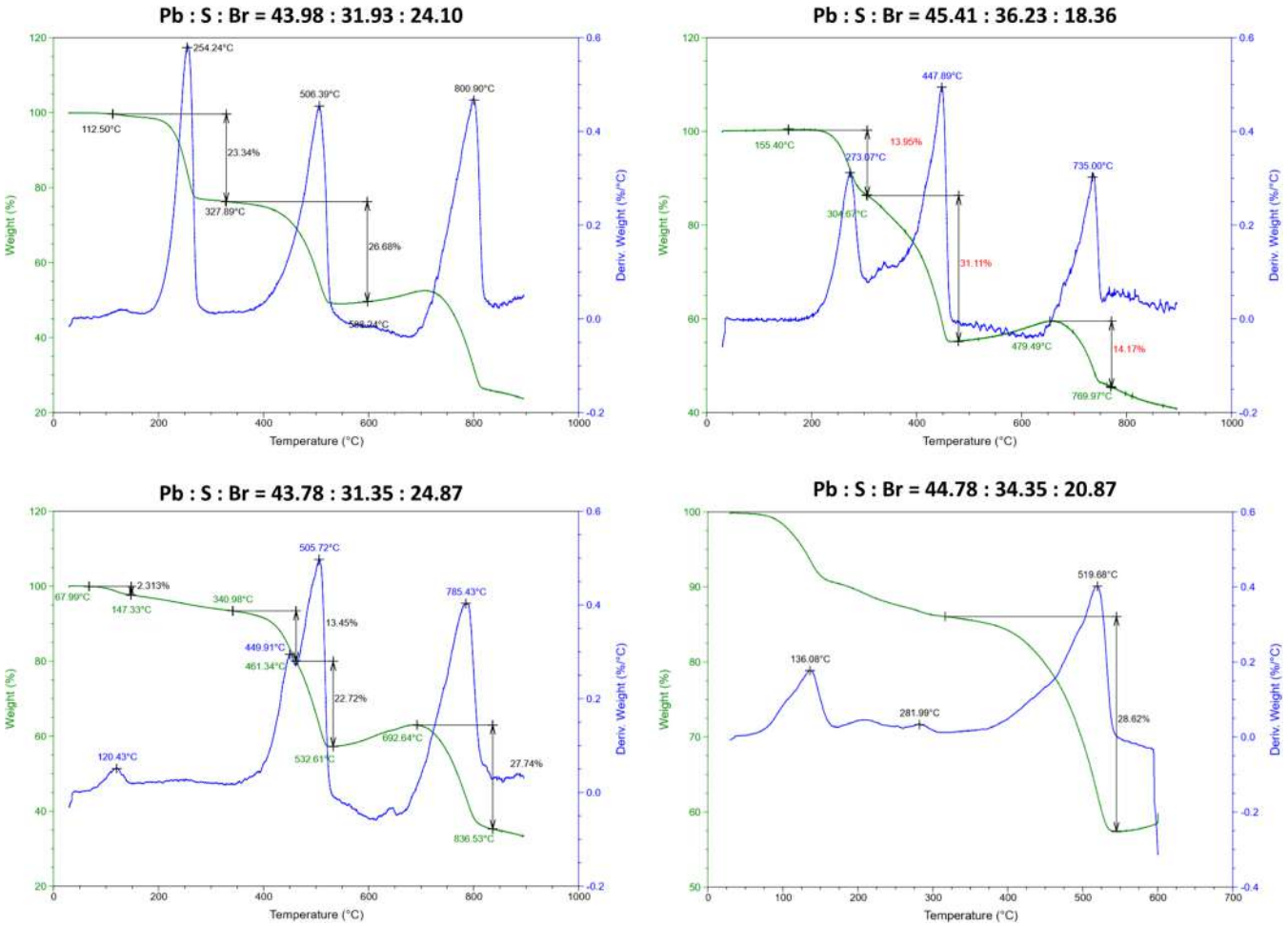

Figure S13. TGA analysis on $Pb_4S_3Br_2$ NCs. Four TGA ramps measured on four different samples, together with the composition extracted from each analysis.

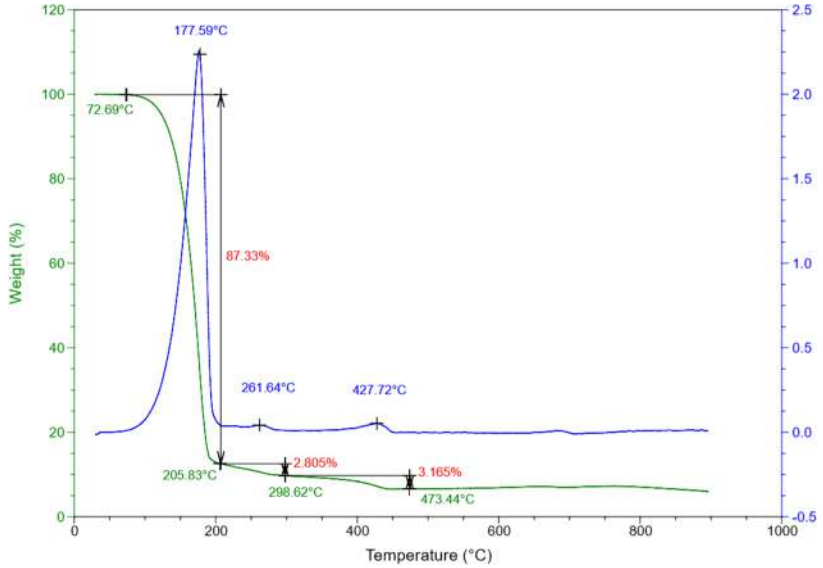

Figure S14. TGA analysis on a non-washed sample $Pb_4S_3Br_2$ NCs. TGA control experiment performed on a non-washed sample (therefore rich in the organic fraction) right after the synthesis. The huge mass loss in the temperature range 70 – 210 °C is due to the evaporation of high boiling point solvent and ligands (ODE, OLAM, OLAC, T_{eb} = 315 – 364 °C).

Figure S13 shows the outcome of the four TGA experiments we used to provide an estimate of the stoichiometry of the NCs based on a "bulk" measurement. We want to point out that the first mass loss, occurring in a temperature range of 110 – 300°C, represents the desorption/decomposition of the organic fraction in the sample (solvent, ligands) and is therefore heavily sample-dependent. For example, the sample in Figure S14 had not been washed, and the first mass loss accounted for a huge 87% of the total. The bottom left sample in figure S13 contained instead the largest particles that we were able to prepare (~30 nm diameter) and had been cleaned carefully. Indeed, the first mass loss in this case accounted for less than 10% of the total.

The second mass loss, combined with the XRD analyses of the sample after the first mass loss and after the second mass loss, carries the compositional information. The stoichiometry was measured from each dataset according to the following method. We first accurately determined the residual relative masses according to the graphical method shown in Figure S15.

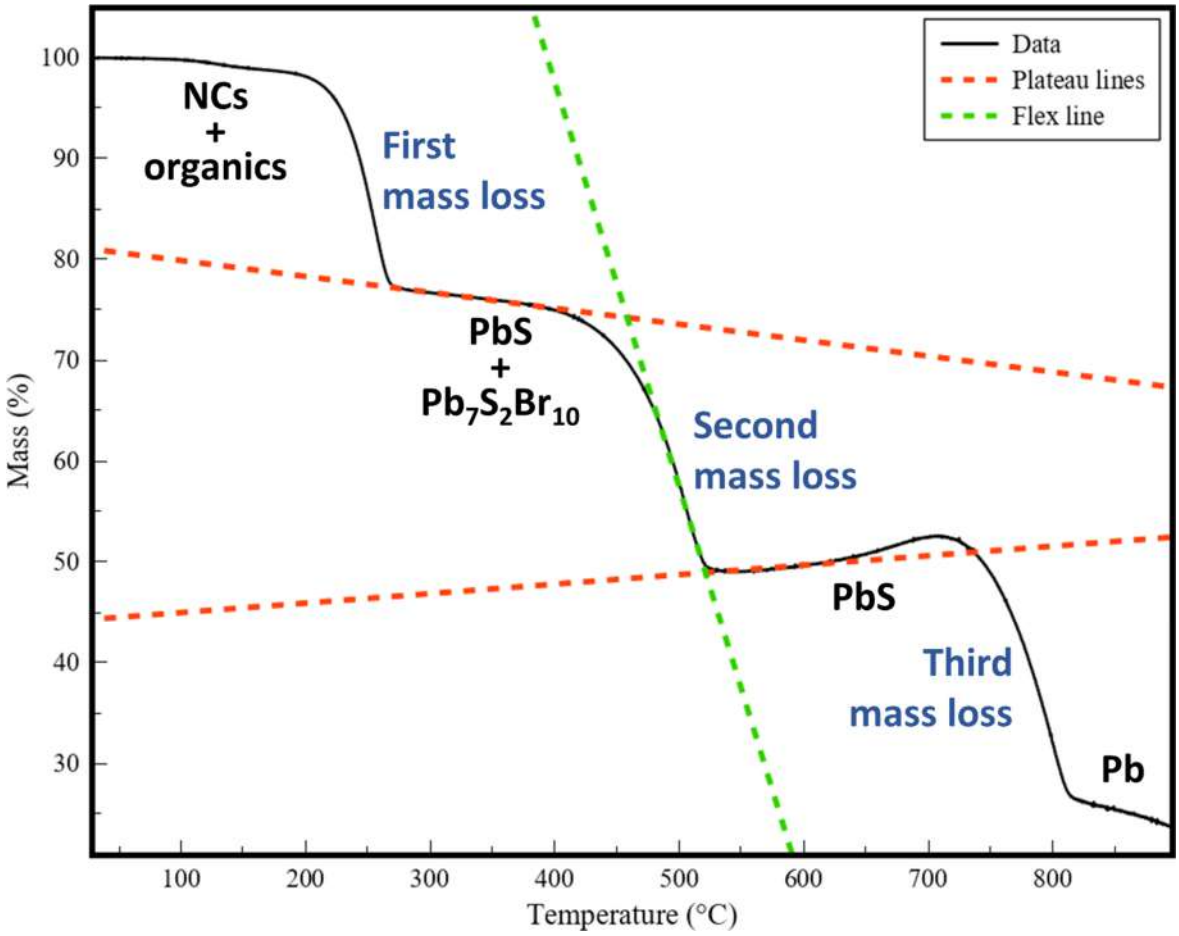

Figure S15. Accurate determination of the initial and final points of the mass loss step. The plateau regions before and after the mass loss were approximated as straight lines tangent to the plot (red lines) as well as the transition slope (green line). The residual relative masses before and after the weight loss were measured at the intersection points between the green and the red lines.

We know from XRPD that, after the first mass loss, the sample contains a mixture of PbS and $Pb_7S_2Br_{10}$, in an unknown molar ratio $x:y$, that is: $x\ PbS + y\ Pb_7S_2Br_{10}$

Assuming that in the first mass loss only the organic fraction is removed, the stoichiometry of our initial NCs, in terms of x and y, is: $Pb_{x+7y}S_{x+2y}Br_{10y}$

In the second mass loss, $Pb_7S_2Br_{10}$ decomposes to PbS and $PbBr_2$, with the latter sublimating, as the only final product left is PbS. The overall sequence of the two reactions, can then be written as:

$$Pb_{x+7y}S_{x+2y}Br_{10y} \rightarrow x\ PbS + y\ Pb_7S_2Br_{10} \rightarrow 5\ yPbBr_2 \uparrow + (x+2y)\ PbS$$

We determine y by the mass loss of the second step, since only $PbBr_2$ sublimates in this step. We then determine x, since we now know experimentally both y and the total mass of PbS left at the end of the second step. From x and y we then determine the stoichiometry of our initial NCs. This estimate was done on four separate TGA+XRD analyses, run on four different samples. The resulting stoichiometries are reported in the following table.

Table S7. Results of the TGA-based compositional analysis.

Measurement	Pb (at%)	S (at%)	Br (at%)
1	43.98	31.93	24.10
2	43.78	31.35	24.87
3	45.41	36.23	18.36
4	44.78	34.35	20.87
Average	44.49	33.46	22.05
St. dev.	0.75	2.26	3.01

h) Electron beam damage effects during high resolution HAADF-STEM image acquisition

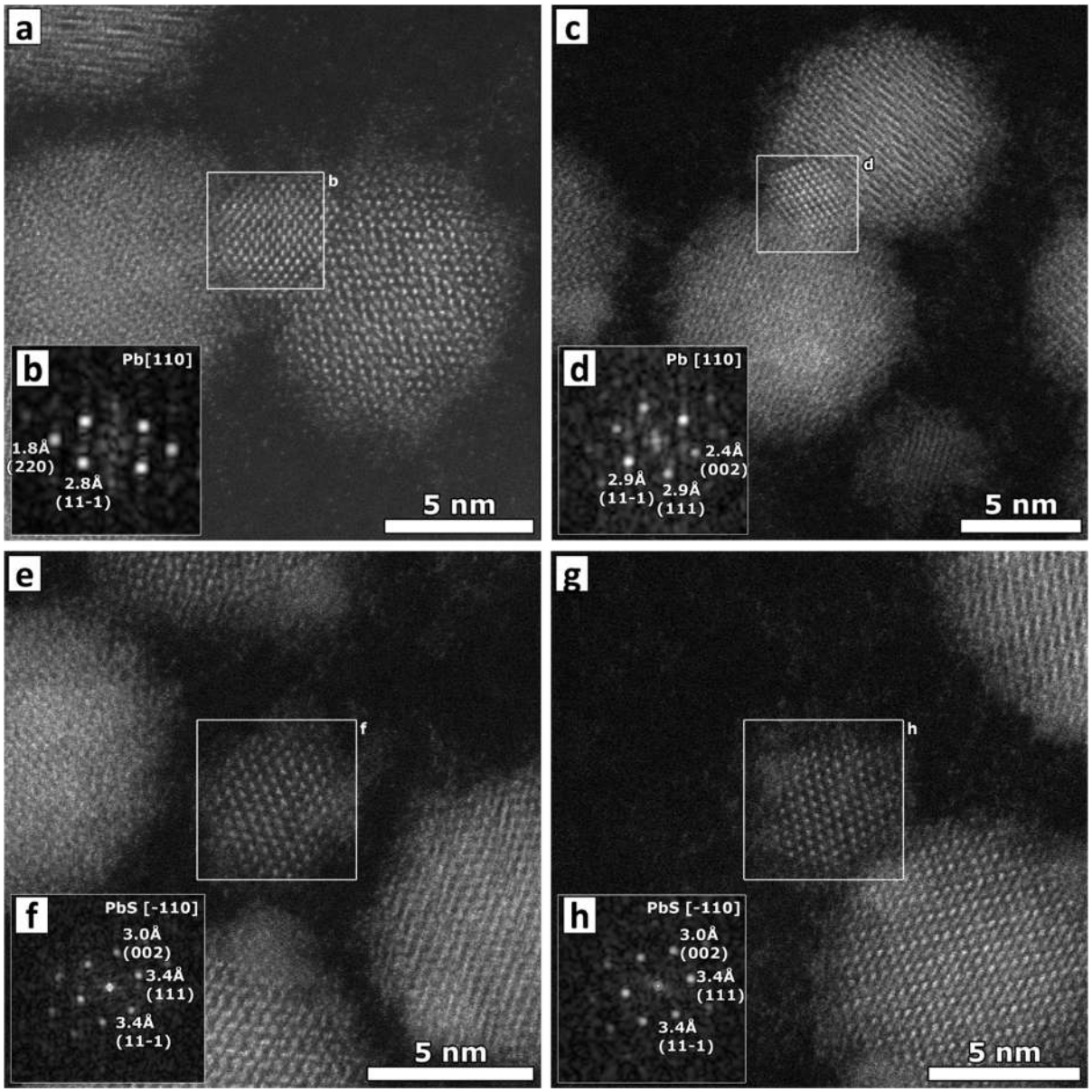

Figure S16. Beam damage during STEM images acquisition. STEM images of the $Pb_4S_3Br_2$ NC together with the Pb (a-c) and the PbS (e-g) NCs formed because of the electron beam-induced damage. The phase of the Pb and PbS NCs was determined *via* atomic lattice distance matching with the help of the calculated Fourier transforms (insets b-d-f-h).

i) *Ab initio* structure solution from 3D-ED data

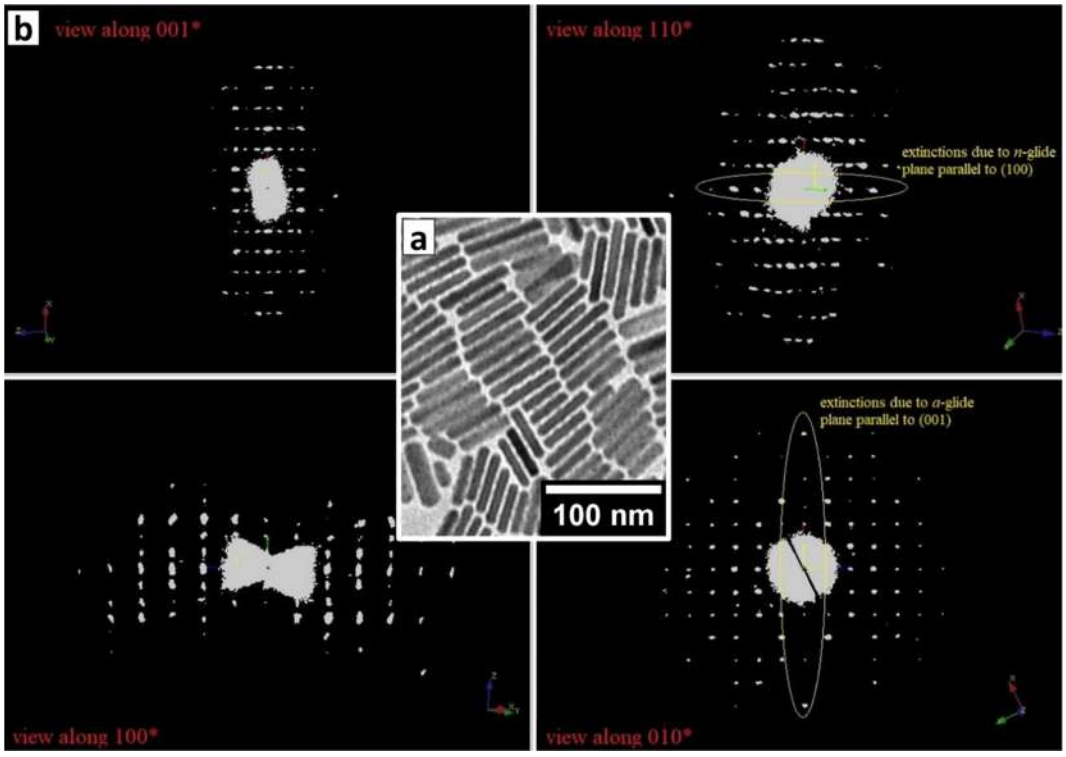

Figure S17. 3D-ED on $Pb_4S_3Br_2$ nanoplatelets. a) TEM image of the $Pb_4S_3Br_2$ nanoplatelets investigated via 3D-ED, together with b) the 3D reconstruction of the reciprocal space of a nanoplatelet viewed along four main reciprocal directions, showing the systematic extinctions exploited for the space group determination.

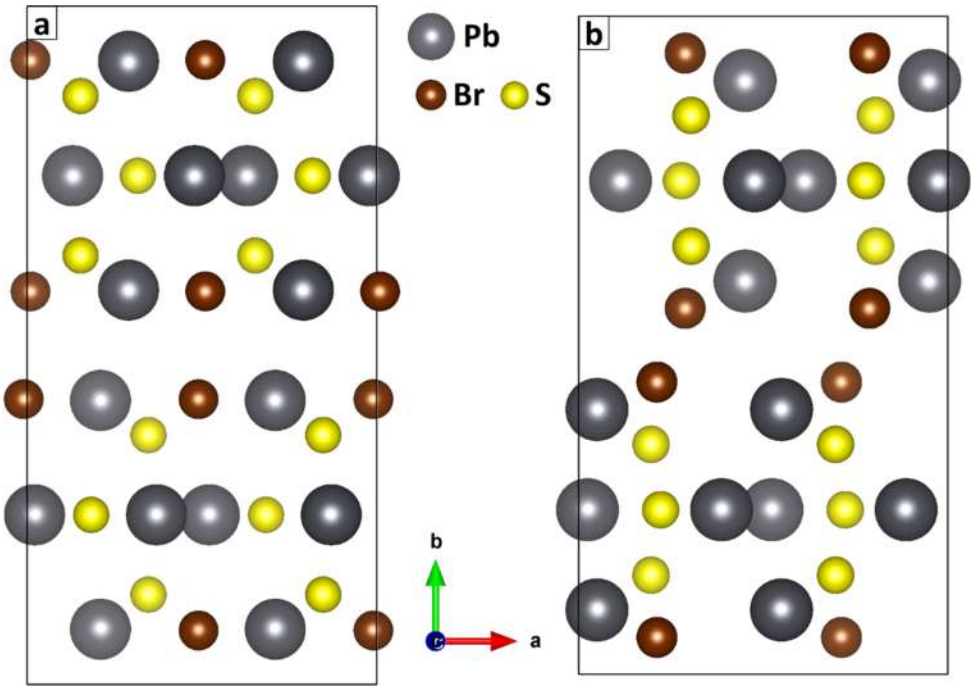

Figure S18. NC and nanoplatelet 3D-ED. A view along the *c* axis of the structural models obtained from the nanoplatelets (a) and from the pseudo-spherical NCs (b). The structures are shown without bonds because, due to the different interatomic distances, different bonds would have appeared, thus complicating the comparison. Due to the low-quality of the data collected on spherical NCs the atomic layout in cell b is unreliable, and the unit cell parameters only were considered. Still, a qualitative match can be recognized between the two structures.

Table S8. Experimental data and 3D-ED structure solution parameters for $Pb_4S_3Br_2$ nanoplatelets.

Crystallographic details	
Unit cell content	$Pb_4S_3Br_2$
Space group	*Pnma*
a, Å	8.0(2)
b, Å	15.5(3)
c, Å	7.9(2)
Cell volume, Å^3	980(40)

3D ED data collection	
Mode	Step-wise with precessing beam
Exposure, s	1.0
Tilt range, °	71.0
Tilt step, °	1.0
Precession angle, °	1.0

Ab initio structure determination in *Pnnn* (SIR2014)	
Data resolution, Å	0.9
N° sampled reflections	2030
N° independent reflections	470
Independent reflection coverage, %	65
R_{sym}, %	16.67
R_{SIR}, %	30.58

j) 3D-FT of the crystal structure extracted from the atomic-resolution tomography

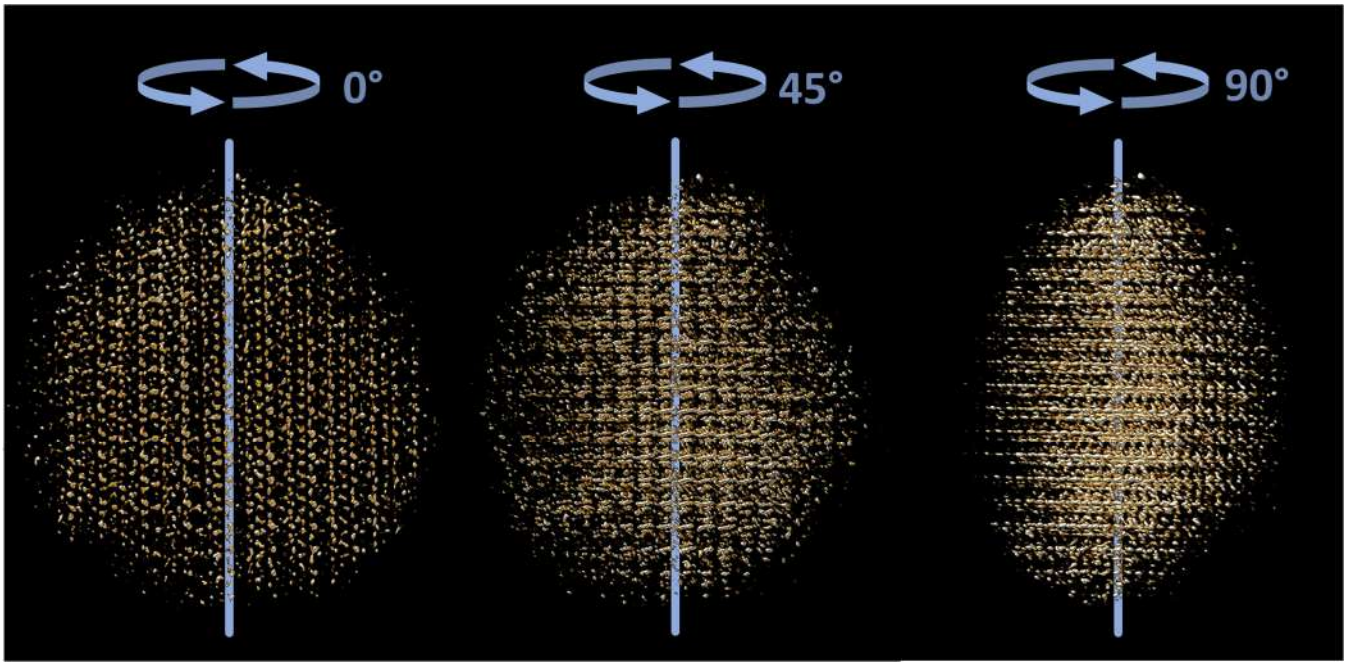

Figure S19. High resolution electron tomography of a NC. The 3D reconstruction of a NC is visualized along three different directions as also seen in Movie_S1. This reconstruction was used to calculate the 3D-FT shown in Movie_S2.

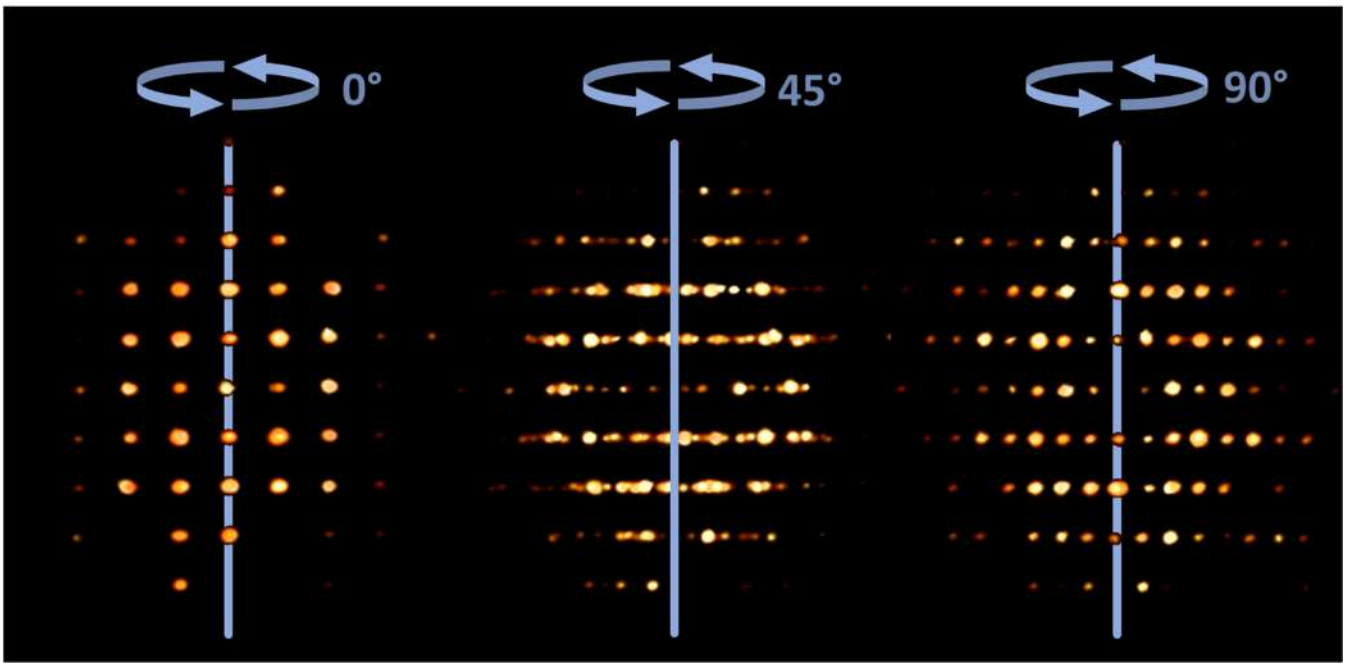

Figure S20. Masked 3D-FT. Starting from the direct-space 3D model shown in Movie_S1, we calculated the (raw) 3D-FT shown in Movie_S2. This data set was subsequently filtered to remove noise and interferences by applying a mask built with the help of the unit cell parameters measured by 3D-ED. The outcome of this procedure is shown in this figure and in Movie_S3.

The direct space electron tomography reconstruction of the NCs, its raw 3D-FT and the filtered version of the 3D-FT are available to the reader in the form of the Movie_S1, Movie_S2 and Movie_S3.*avi* video files.

k) *Ab initio* structure solution from XRPD data

Indexing.

The determination of the cell parameters, the first crucial step of the *ab initio* structure solution, was carried out by EXPO2014,[8] providing to the indexing program N-TREOR09[9] 28 observed peak positions in the 12°-89° 2θ range. Due to the large broadness of the experimental peaks and the consequently unavoidable low accuracy of peak positions, and in order to be able to find the correct cell among the possible ones, the indexing process was carried out in a non-default way by increasing the tolerance concerning the errors on peak positions and the maximum allowed number of unindexed lines. In a default indexing run of N-TREOR09 a plausible cell is characterized by a value of the M_{20} de Wolff figure of merit[10] and of the maximum number of unindexed lines (NIX) equal to or larger than 10 and not greater than one, respectively. In case of the NC powder diffraction pattern, the thresholds on the minimum allowed value of M_{20} and on the maximum tolerated value of NIX were set to 6 and 3, respectively. The less restrictive indexing criteria unavoidably increased the number of possible cells compatible with the experimental data and, at the same time, enabled to include also the correct one, an orthorhombic cell (cell parameters a=8.157862 Å, b=14.849445 Å and c=8.124080 Å), characterized by M_{20} and NIX values equal to 6 and 2, respectively. To recognize the correct cell among the set of candidate cells, the indexing results concerning the orthorhombic cell determined by the 3D electron diffraction study were taken into account.

Space group determination.

The space group determination process by EXPO2014 exploits the information on cell parameters, integrated intensities (extracted in the space group having the largest Laue symmetry and no extinction conditions, *i.e*., in *Pmmm*) and expected unit cell content, to carry out a statistical analysis on suitably weighted integrated intensities, in order to detect systematic absences and calculate a probability value associated to the different possible extinction symbols compatible with the identified crystal system[11–13]. Due to the broad and overlapping peaks in the NC powder pattern and, consequently, to the large errors on the integrated intensities estimates, the results of the statistical study were unreliable and prevented the correct identification of the space group. In case of the 3D-ED data, the greater accuracy of the integrated intensities enabled to detect the absence of:

i) The class of reflections (0 k l) with k+l odd (*i.e.,* the presence of a glide n normal to the a axis)

ii) The class of reflections (h k 0) with h odd (*i.e.,* the presence of a glide a normal to the c axis)

This led to the identification of the space group *Pnma*. This result, derived by the investigation based on 3D electron diffraction data, was actively used for the structure solution step by powder diffraction data.

Full pattern decomposition.

EXPO2014 estimates the integrated intensities of reflections by alternating the application of the Le Bail algorithm[14] to least-squares cycles minimizing the residual between observed and calculated profiles. The default profile function used to describe the peak shape is the Pearson VII. The refined variables are scale factor, background coefficients, 2θ-zero shift, peak asymmetry, FWHM parameters, the *m* parameter of the Pearson VII function and the unit cell parameters. Thanks to a useful property of the Le Bail algorithm, to improve the integrated intensities estimates EXPO2014 can fruitfully take advantage of some prior information[15], including the expected positivity of the Patterson function[16] that is particularly effective in case of structures with heavy atoms; for that reason, it was exploited in case of the NC powder diffraction pattern.

Structure solution and structure model optimization.

The default structure solution process by EXPO2014 is based on the application of Direct Methods (DM), providing 20 set of phases processed by the ALLTRIAL procedure[8], that, for each set of stored phases, automatically performs a preliminary refinement and structure model optimization by a Fourier recycling approach[17]; the corresponding 20 structure models were carefully analyzed by a graphical inspection. The structure model showing the most plausible chemical environment of the Pb atoms (in terms of heavy-atom coordination and interatomic distances, in agreement with the main crystallochemical rules) and the most plausible crystal packing (*i.e.*, that one characterized by the absence of unreliable voids in the cell or implausible large density of atoms, this last usually due to the presence of false atoms in the model) was selected and improved *via* the EXPO2014 graphic tools, allowing to correct some errors on atom labelling and optimize the position of the Br atom (*i.e.*, by deleting and relocating it *via* the calculation of an additional electron density map using $2F_o$-F_c coefficients, where F_o and F_c are the observed and calculated structure factor modulus, respectively). The asymmetric unit of the crystal structure determined by the *ab initio* structure solution from XRPD data (whose main details are provided in Table S9) and its local environment are shown in Figure S21a and S21b, respectively. The crystal structure reveals itself very similar to that one determined by 3D electron data (see Figure S22, showing a view of the overlay of the crystal structures determined by XRPD and 3D electron diffraction data, represented by red and blue rods respectively). A comparison of the two structure models reveals a root mean square deviation (RMSD) of 0.534 Å between them.

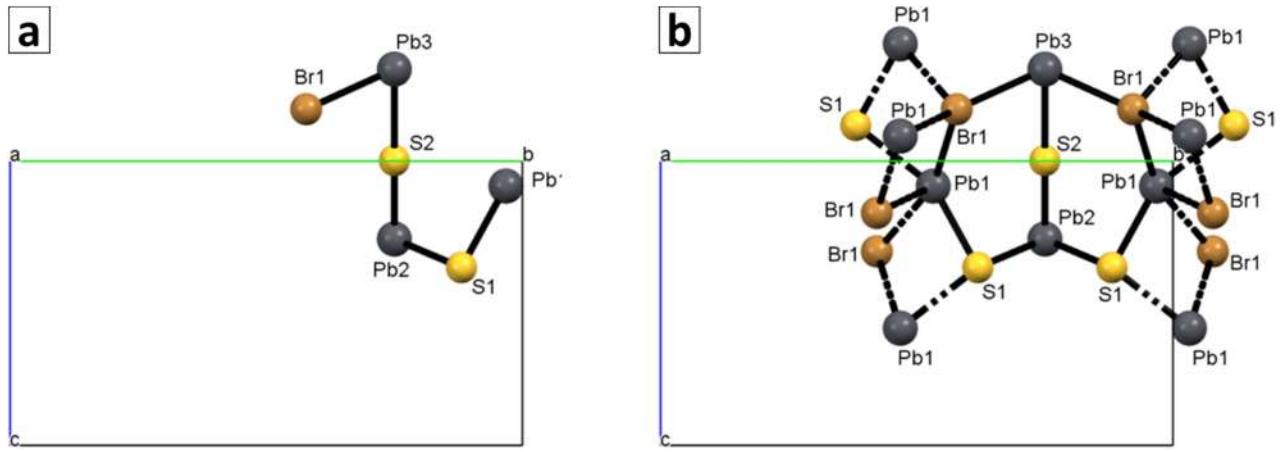

Figure S21. *Ab initio* structure solution from XRPD data. The asymmetric unit a) and its surroundings b) as obtained from the XRPD data-based *ab initio* structure solution.

Table S9. *Ab initio* structure solution from XRPD data. Main crystal data, Wyckoff sites, fractional atomic coordinates, isotropic displacement parameters and geometrical parameters for the XRPD-based *ab initio* structure solution.

Chemical formula	$Pb_4S_3Br_2$
M_r	1084.81
Crystal system, space group	Orthorhombic, *Pnma*
a, *b*, *c* (Å)	8.22592, 14.70843, 8.13988
V(Å^3)	984.847
Z	4
Wavelength (Å)	1.54056
Dx	7.316 mg m^{-3}

Wickoff site, fractional atomic coordinates and isotropic displacement parameters (Å^2)

Atom	*Wick. Site*	*x*	*y*	*z*	U_{iso}
Pb1	8*d*	0.7875	0.9678	0.0879	0.0319
Pb2	4*c*	0.9374	0.7500	0.2740	0.0319
Pb3	4*c*	0.6266	0.7500	−0.3232	0.0319
Br1	8*d*	0.5249	0.5780	−0.1824	0.0619
S1	8*d*	0.6930	0.8809	0.3744	0.0555
S2	4*c*	0.7844	0.7500	−0.0020	0.0025

Geometrical parameters (Å, º).

Pb2—S2	2.5751	S2—Pb3	2.9190
Pb2—S1	2.9011	S1—Pb1	2.7707
Pb2—Pb1	3.7520	Pb3—Br1	2.9006
S2—Pb2—S1	84.67	Pb2—S1—Pb1	82.80
S2—Pb2—Pb1	59.15	Pb2—Pb1—S1	50.10
Pb2—S2—Pb3	177.15	S2—Pb3—Br1	76.96
S1—Pb2—Pb1	47.11		
S1—Pb2—S2—Pb3	138.20	S2—Pb2—Pb1—S1	114.03
Pb1—Pb2—S2—Pb3	95.98	S1—Pb2—Pb1—S1	0.02
S2—Pb2—S1—Pb1	−51.95	Pb2—S2—Pb3—Br1	116.46
Pb1—Pb2—S1—Pb1	0.02	Pb2—S1—Pb1—Pb2	0.02

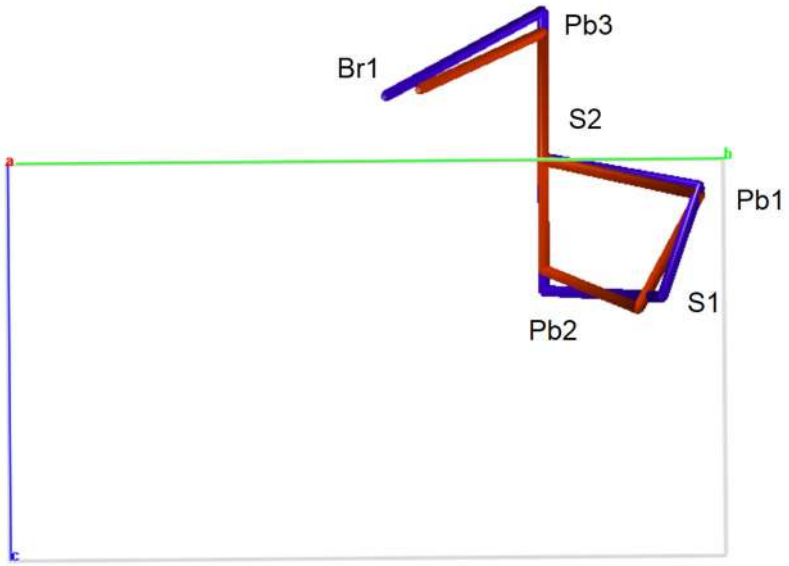

Figure S22. Visual assessment of matching between XRPD and 3D-ED models. Overlay of the asymmetric unities of the structure models obtained by 3D-ED (blue) and by XRPD (red) ab initio structure solution. The root mean square deviation (RMSD) for the two structure models was found to be 0.534 Å.

l) Crystal structures relaxed by DFT calculations

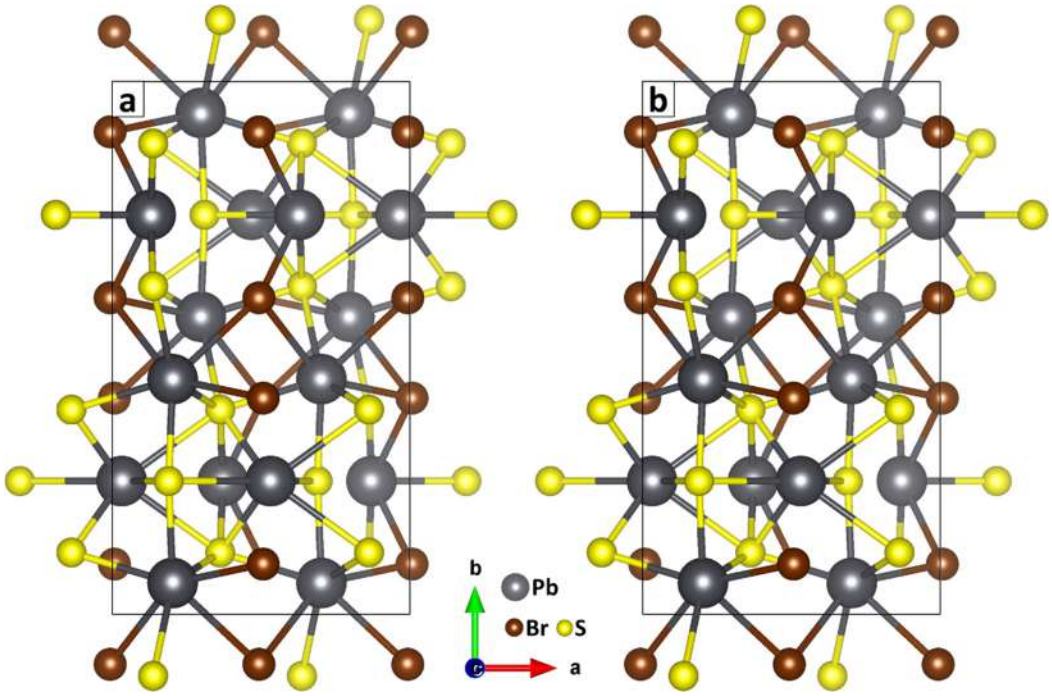

Figure S23. DFT-relaxed 3D-ED and XRPD based structures. Structures emerging from DFT calculations using the a) 3D-ED and b) XRPD based unit cells as input structures. The two structures were relaxed by keeping the unit cell parameters fixed (for both a = 8.22592 Å, b = 14.70843, c = 8.13988 Å). The two models converged to the same structure, based on the level of calculation tolerances.

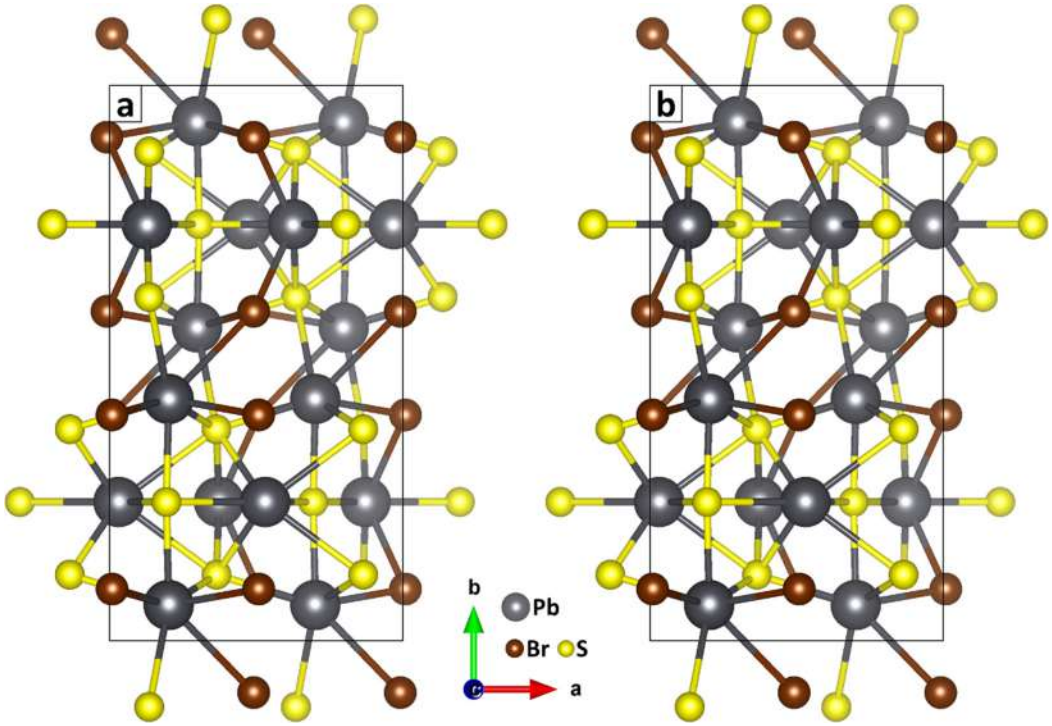

Figure S24. DFT-relaxed 3D-ED and XRPD based structures. Structures emerging from DFT/PBE calculations using the a) 3D-ED and b) XRPD based unit cells as input structures. The two structures were relaxed by letting the unit cell parameters free to vary. The two models converged to the same structure, based on the level of calculation tolerances, and, remarkably, the unit cell parameters converged to values (for both a = 8.14556 Å, b = 15.41923, c = 8.08130 Å) compatible with those measured for nanoplatelets by 3D-ED.

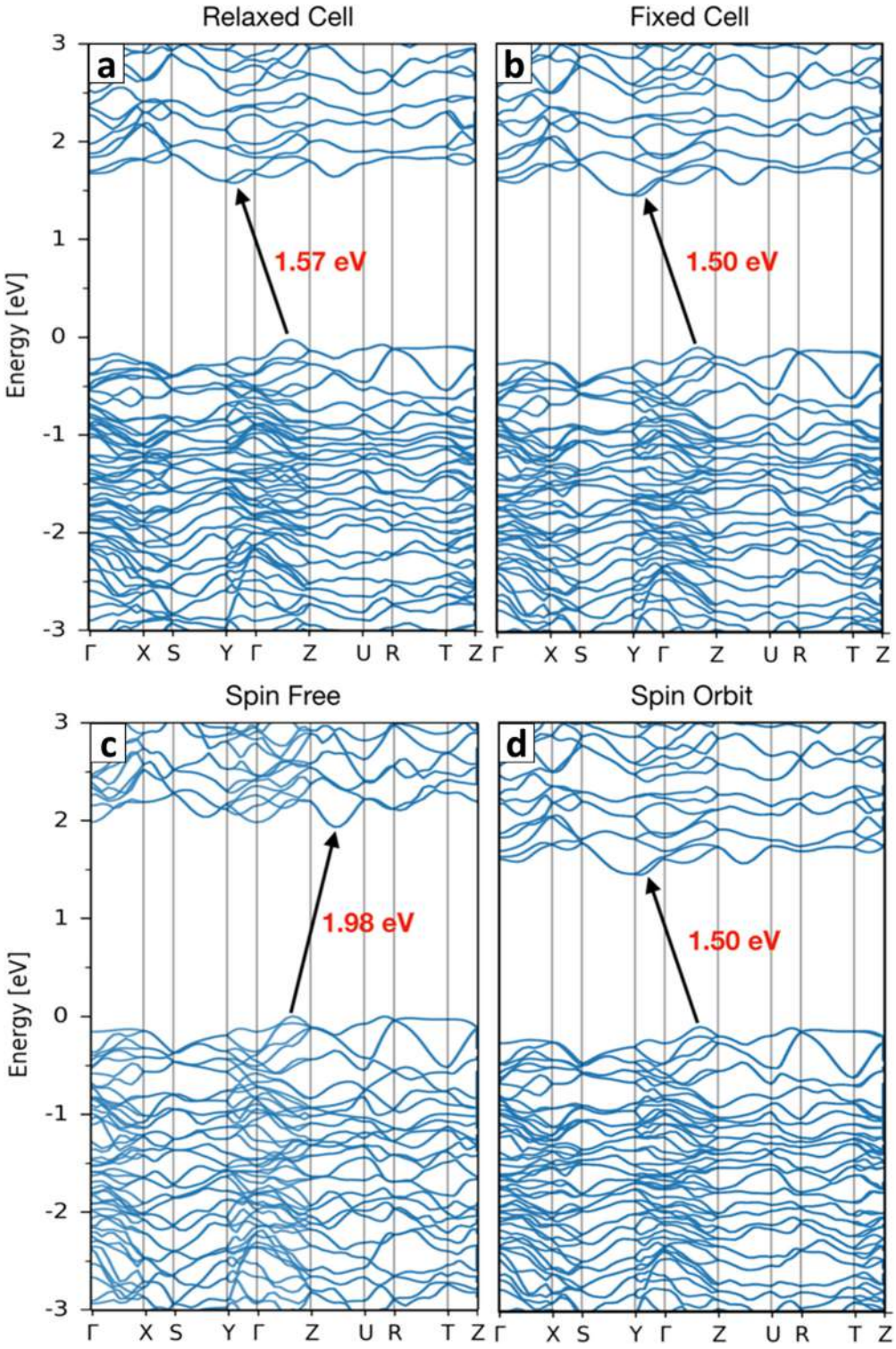

Figure S25. Calculated band structures for $Pb_4S_3Br_2$. Top: band structures computed on the unit cells with relaxed parameters (which converged to a = 8.14 Å, b = 15.42Å, c= 8.08 Å, corresponding to nanoplatelets, panel a and Figure S24) and with fixed parameters (a = 8.226 Å, b = 14.708 Å, c = 8.140 Å, corresponding to pseudospherical NCs, panel b and Figure S23). The composition of the band states remains similar with only a slight widening of the gap from the constrained (fixed) to the unconstrained (relaxed) cell. Bottom: band structures of the unit cell with fixed parameters computed excluding (c) and including (d) spin orbit coupling. In both cases the gap is indirect, however the spin free case shows a different k-point at the bottom of the conduction band; the band gap also increases up to about 2 eV. All band structures have been computed at the DFT/PBE level of theory.

m) Comparison between the proposed structures for $Pb_4S_3I_2$, $Pb_4S_3Br_2$ and $Pb_3S_2Cl_2$ NCs.

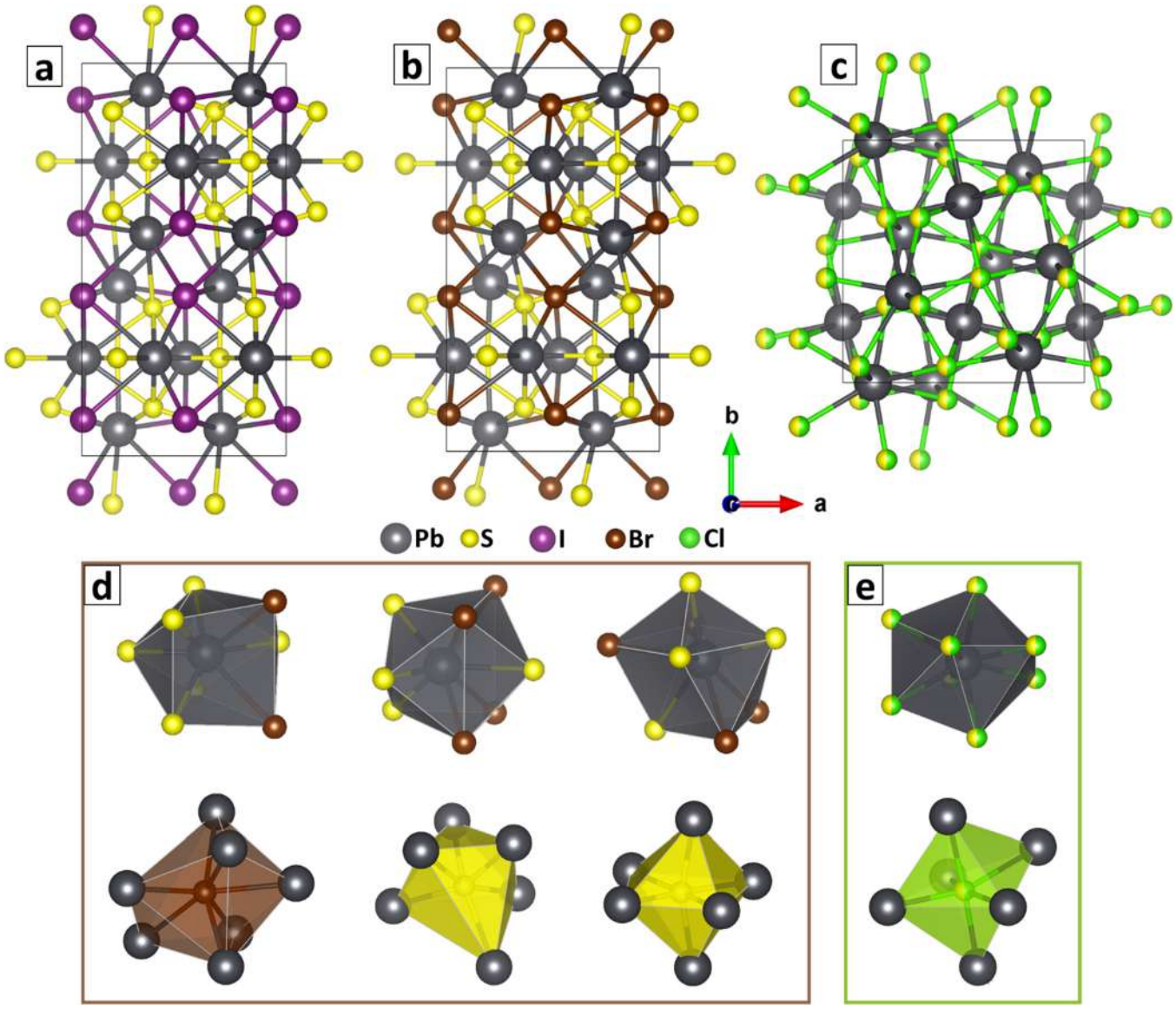

Figure S26. $Pb_4S_3I_2$, $Pb_4S_3Br_2$ and $Pb_3S_2Cl_2$ crystal structures and coordination polyhedra. The crystal structures proposed for NCs of $Pb_4S_3I_2$ **(a), $Pb_4S_3Br_2$ (b) and $Pb_3S_2Cl_2$ (c). Iodide- and bromide-based NCs are clearly isostructural, while $Pb_3S_2Cl_2$ shows no resemblance** to the other two structures **at a first sight. However, the coordination polyhedra for** all three structures are very similar.

n) Rietveld refinement of the $Pb_4S_3Br_2$ structure

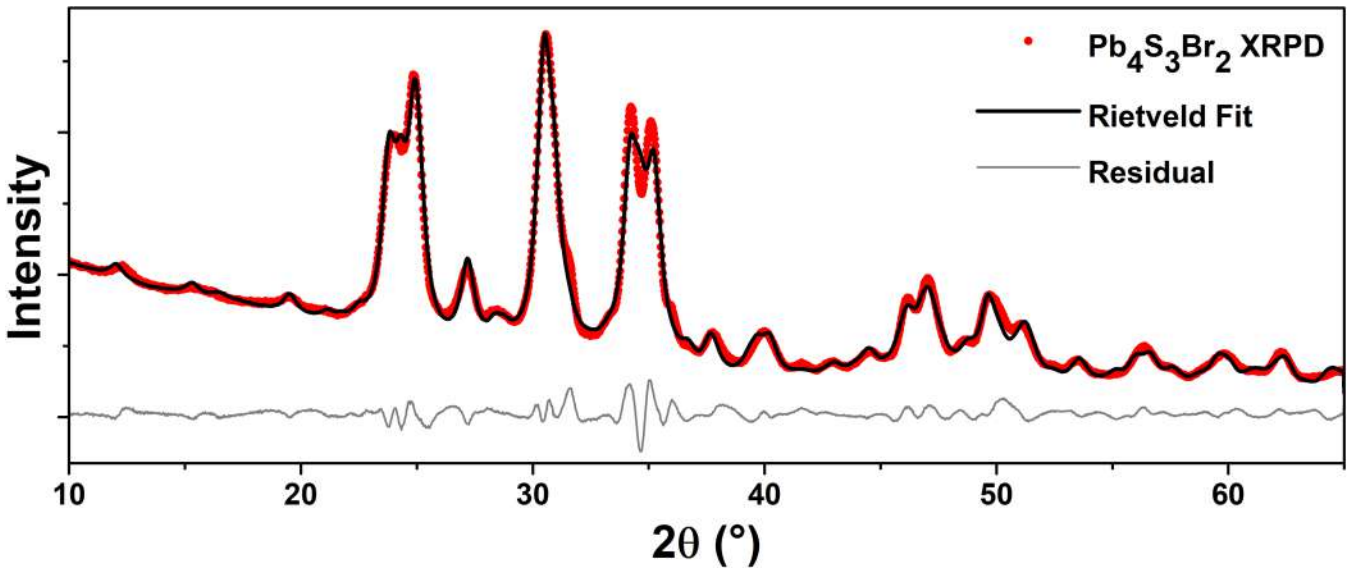

Figure S27. $Pb_4S_3Br_2$ XRPD. Rietveld refinement of the $Pb_4S_3Br_2$ NCs structural model shown in Figure 4d.

The Rietveld refinement of the structural model originally obtained from the DFT/PBE relaxation was performed by fitting an XRPD pattern measured on ~15 nm particles. The refined parameters were (listed according to the refinement order):

- Unit cell parameters
- Atomic coordinates
- Isotropic size parameter
- Anisotropic thermal factors (only positive or null parameters were accepted)
- Refinable-points linear interpolation background

The outcome of the refinement is summarized in the table below.

Table S10. $Pb_4S_3Br_2$ Rietveld Refinement. Outcome of the Rietveld refinement on the $Pb_4S_3Br_2$ structural model.

Space group	Pnma (no. 62)					
Unit cell parameters	**a (Å)**		**b (Å)**		**c (Å)**	
	8.202		14.707		8.165	
	α (°)		**β (°)**		**γ (°)**	
	90		90		90	
Atomic coordinates	**x**		**y**		**z**	
Pb 1	0.134		0.750		0.168	
Pb 2	0.464		0.750		0.810	
Pb 3	0.7918		0.944		0.985	
S 1	0.774		0.750		0.006	
S 2	0.673		0.871		0.619	
Br 1	0.477		0907		0.169	
Anisotropic Thermal Factors / Form Factors	**B11**	**B22**	**B33**	**B12**	**B13**	**B23**
Pb 1	0.02609	0.13468	0	0	0.02761	0
Pb 2	0.04174	0.09132	0.01543	0	0	0
Pb 3	0.12421	0.01533	0.12751	0.01001	0	0.02785
S 1	0	0	0	0	0	0
S 2	0.07355	0	0	0.04823	0	0.02516
Br 1	0.0652	0.03762	0	0	0.05184	0.04434
Goodness of Fit	8.3					

Notes on the fit: refining the anisotropic thermal factors was needed in order to reach a good match between the data and the calculated profile. Only null or positive values were allowed.

The following crystal structures are available to the reader in the form of .CIF files;

- DFT-relaxed structure as shown in Figure 4d: Pb4S3Br2_DFT.cif
- Rietveld-refined structure: Pb4S3Br2_Rietveld.cif

o) Temporal stability assessment for $Pb_4S_3Br_2$ NCs

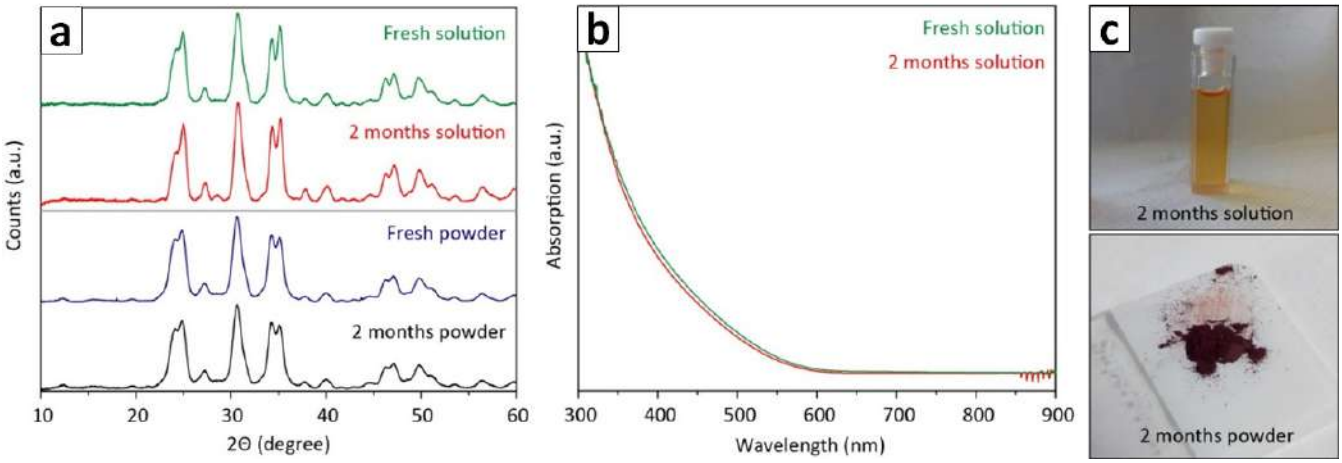

Figure S28. Temporal stability of $Pb_4S_3Br_2$ NCs. a) XRPD patterns of the same $Pb_4S_3Br_2$ NC colloidal suspension / dry powder as-prepared and after 2 months of aging in a dry and dark environment. b) Absorption spectra of the solution before and after aging. c) Photographs of the two samples after 2 months of aging. No differences are visible when compared with a freshly prepared sample.

p) Complementary characterization for the photodetectors and solar cells.

Figure S29a shows the I-V characteristics in dark and light of the photodetector made from SCN-exchanged $Pb_4S_3Br_2$ NC film. Regarding the solar cell, Figure S29b-c show a representative SEM image of the film together with the stability tests of the cell carried out during storage in air and dark conditions (data averaged from 3 different devices).

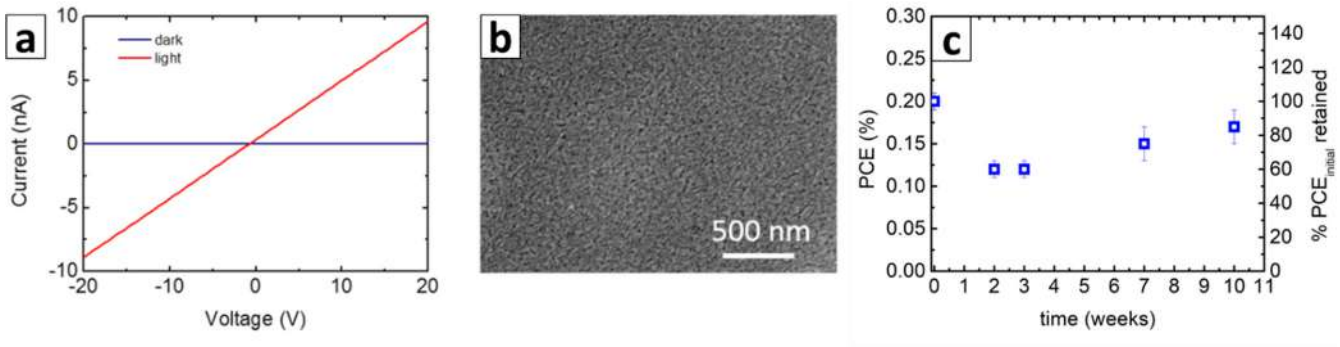

Figure S29. Complementary characterization for the photodetectors and solar cells. a) I−V characteristics of the $Pb_4S_3Br_2$ NC-based photodetector with Ti/Au interdigitated bottom contacts (gap of 1μm) in dark and under white LED light (400−750nm, 100 mW cm^{-2}). b) Representative SEM image of the $Pb_4S_3Br_2$ NC film used in the solar cell stack. c) Time evolution of the PCE of the solar cells stored in the dark under ambient conditions. Values shown are the average results from the monitoring of 3 different devices.

Figure S30 shows the Noise Power Spectra Density of a time trace acquired from the photodetector in the dark, in the same experimental condition of the light response measurements (Fig. 6a-c of the main text). From this spectrum, the noise figures of merit were calculated.

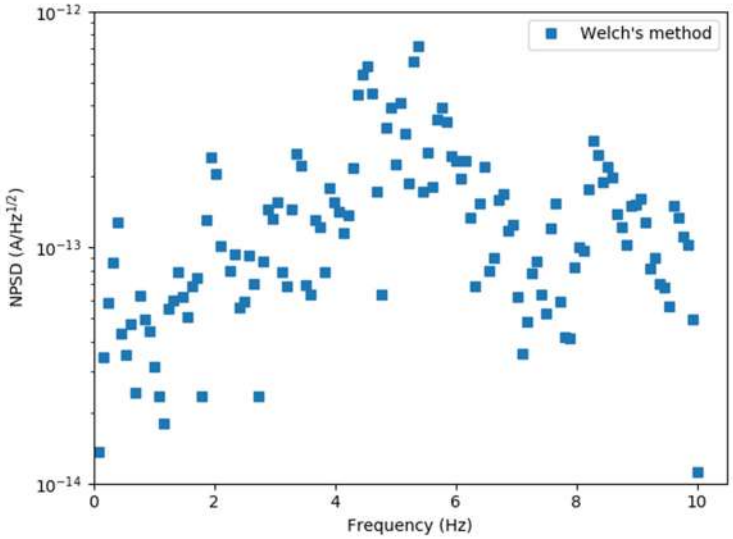

Figure S30. Noise Power Spectra Density calculated from the Fourier Transform (using the Welch's method)[18], of time trace in the dark, after removing a constant background.

q) XPS and UPS analyses on ligand-exchanged $Pb_4S_3Br_2$ NCs.

As reported in the main text, to make a film of $Pb_4S_3Br_2$ NCs conductive and use it as active layer in a photovoltaic device, we performed a solid-ligand exchange with 1-ethyl-3-methylimidazolium iodide (EMII, see details in the main manuscript). The effectiveness of the ligand replacement as well as the suitability of the energy level alignment from the ligand exchange in the layered stack were investigated via XPS and UPS. Figure S31 shows the comparison of the wide scans collected on the pristine sample and on the sample after ligand exchange. The surface of the starting sample contained carbon and oxygen species due to the original organic ligands used in the colloidal synthesis (see O 1s and C 1s peaks at approx. 530 eV and 285 eV, respectively, in the wide scan shown in the top panel of Fig. S31). After ligand exchange, the intensity of those signals was strongly reduced, indicating the effective removal of the ligands; at the same time, signals due to the presence of iodine appeared. The position of the main I 3d peak at (619.5 ± 0.2) eV indicates that iodine is present as iodide, in agreement with literature,[7] and further corroborating the effectiveness of the ligand exchange procedure.

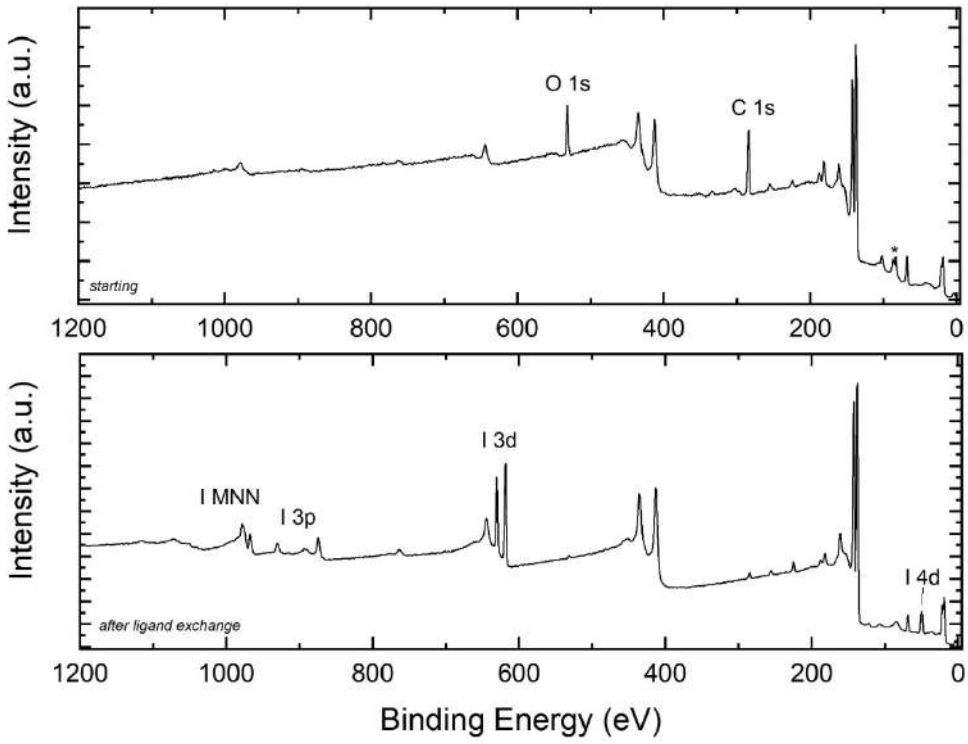

Figure S31. XPS analysis on ligand-exchanged $Pb_4S_3Br_2$ NCs for solar cell tests. XPS data collected on as synthesized $Pb_4S_3Br_2$ NCs (top panel) and on those after the ligand exchange (bottom panel). The ligand exchange induced a drastic reduction of the surface carbon and oxygen species, as evidenced by the decrease of the intensities of the O 1s and C 1s peaks, confirming the effective removal of the starting ligands. At the same time, signals due to iodine species appeared, due to the surface passivation with iodide ions of EMII. Note: in the top panel, at approx. 84 eV, the signals due to the gold substrate are visible.

We further studied the ligand-exchanged sample *via* UPS, to extract its work function and the valence band maximum (VBM) position. The results are reported in Figure S32, together with the linear extrapolation of the high and low binding energy onsets. The high binding energy onset is directly correlated with the work function (WF) of the material. With the measured onset at 16.9 eV, we calculated the WF as difference between the He I photon energy and the onset value itself. The resulting WF is 4.30 ± 0.05 eV. The low binding energy onset relates instead with the distance between the top of the valence band (VBM) and the Fermi level (E_F), assumed as zero of the binding energy scale. As shown in the figure, the position of the valence band maximum is at 1.6 ± 0.1 eV below E_F. The position of VBM with respect to the vacuum level is therefore -5.9 ± 0.12 eV.

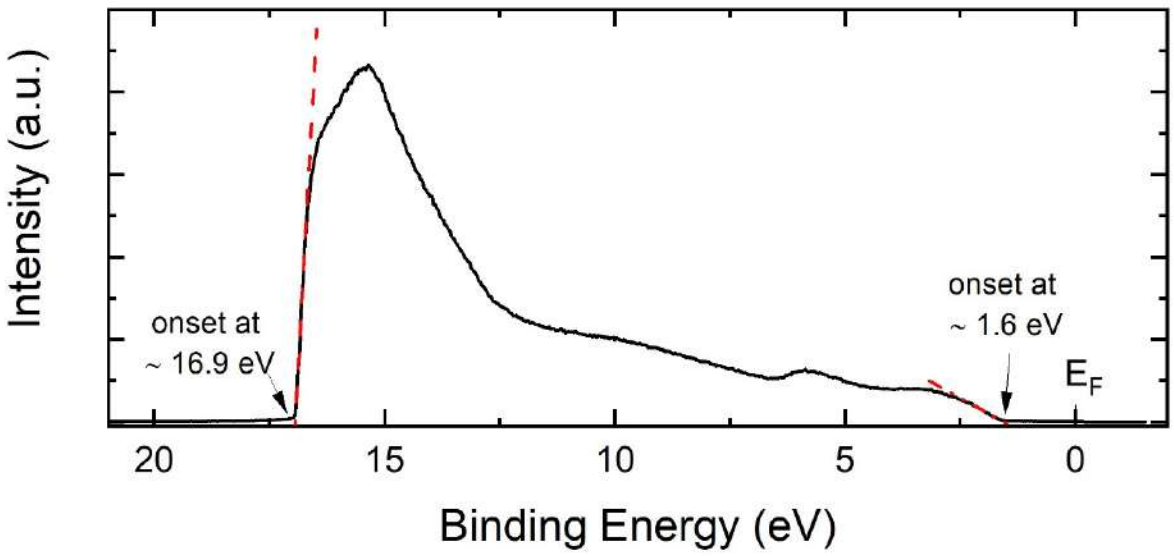

Figure S32. UPS analysis on ligand-exchanged $Pb_4S_3Br_2$ NCs for solar cell tests. UPS data collected on the $Pb_4S_3Br_2$ nanocrystals after the ligand exchange procedure. The high and low binding energy onsets, as obtained via linear extrapolation, are marked.

As a further evidence of the possibility to tune the energy levels of the $Pb_4S_3Br_2$ NCs, we also carried out UPS analysis of the sample that had been ligand-exchanged with NH_4SCN and used for the fabrication of the photodetectors (see procedure in the main text). The results are reported in Figure S33, together with the data collected on starting organic capped-NCs. Similarly to what done on the sample that had been ligand-exchanged with EMII, we obtained the WF and VBM position on these two samples via linear extrapolation of high and low binding energy onsets. For the pristine sample, before ligand exchange, the resulting WF is 4.10 ± 0.05 eV and the VBM is at 1.1 ± 0.1 eV below E_F. The position of VBM with respect to the vacuum level is therefore -5.20 ± 0.11 eV. In the case of the SCN-exchanged sample, instead, the WF is 4.60 ± 0.05 eV and the VBM is at 0.9 ± 0.1 eV below E_F, corresponding to a

position with respect to the vacuum level of -5.20 ± 0.11 eV. These data therefore confirm that, as reported in literature for other colloidal NCs,[19,20] the energy levels of our $Pb_4S_3Br_2$ NCs could be tuned by a proper choice of the surface ligands.

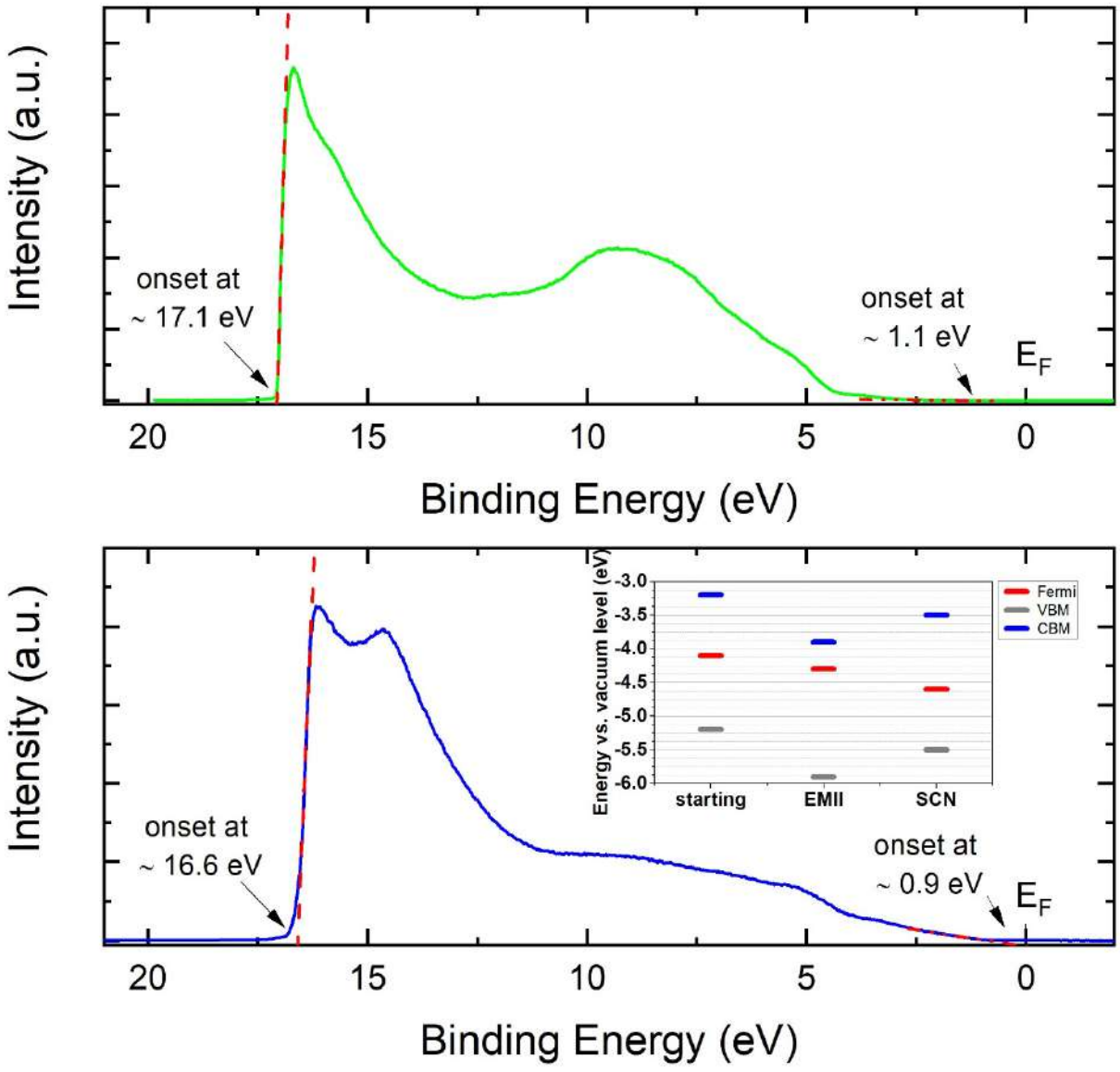

Figure S33. UPS analysis on starting and SCN- ligand-exchanged $Pb_4S_3Br_2$ NCs. UPS data collected on the $Pb_4S_3Br_2$ NCs before (top) and after the ligand exchange procedure with NH_4SCN (bottom). The high and low binding energy onsets, as obtained via linear extrapolation, are marked. Inset in bottom panel shows the energy level diagrams of the $Pb_4S_3Br_2$ NCs with the ligands used in this work. The position of the conduction band minimum (CBM) has been obtained by adding the optical bandgap (approx. 2 eV) to the position of the VBM.

r) DFT band structure calculations for $Pb_4S_3I_2$ and $Pb_3S_2Cl_2$

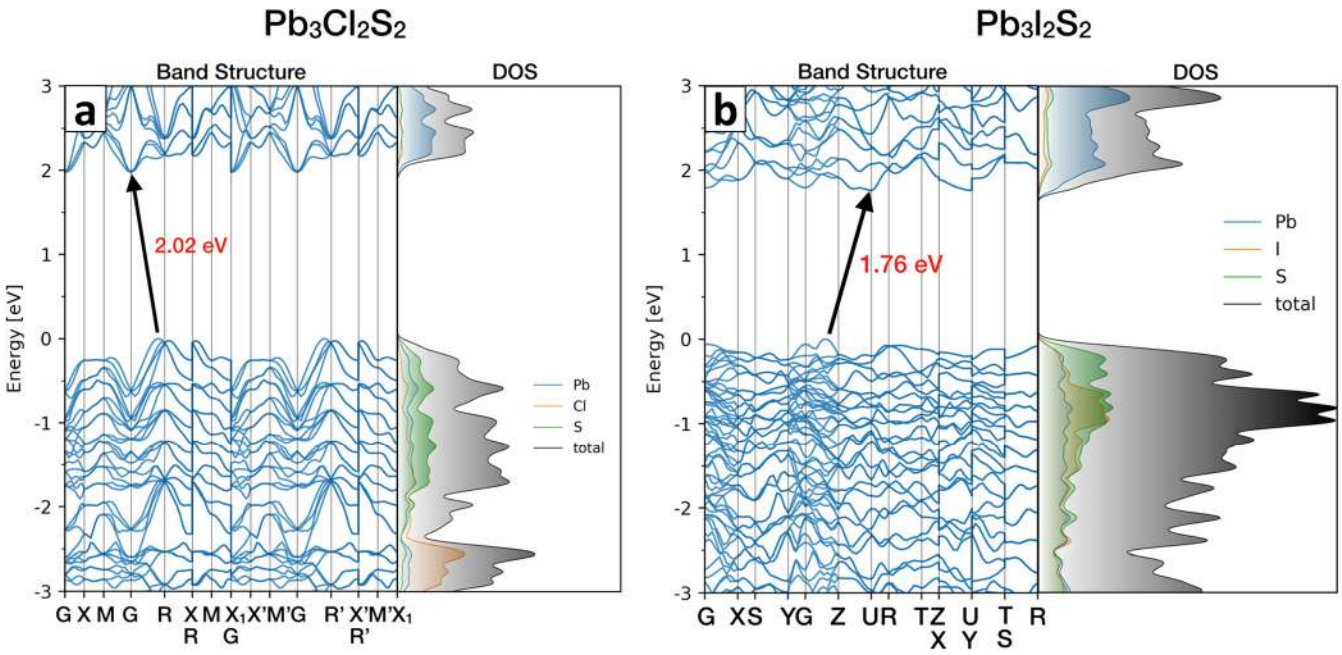

Figure S34. Calculated band structures for $Pb_3S_2Cl_2$ and $Pb_4S_3I_2$, based on the structures published by Ni *et. al.*[4,6] The calculations were performed starting from the models obtained by Rietveld fit as reported in sections S.c,d, after relaxing the unit cell content while keeping the cell parameters fixed. Since Cl and S atoms in $Pb_3S_2Cl_2$ share randomly the same Wyckoff sites, a stoichiometric cell with random distribution of the two elements was considered. Calculations were performed without including spin orbit coupling (SOC) to better estimate the bandgap.

s) FTIR characterization of $Pb_4S_3Br_2$ NCs and devices.

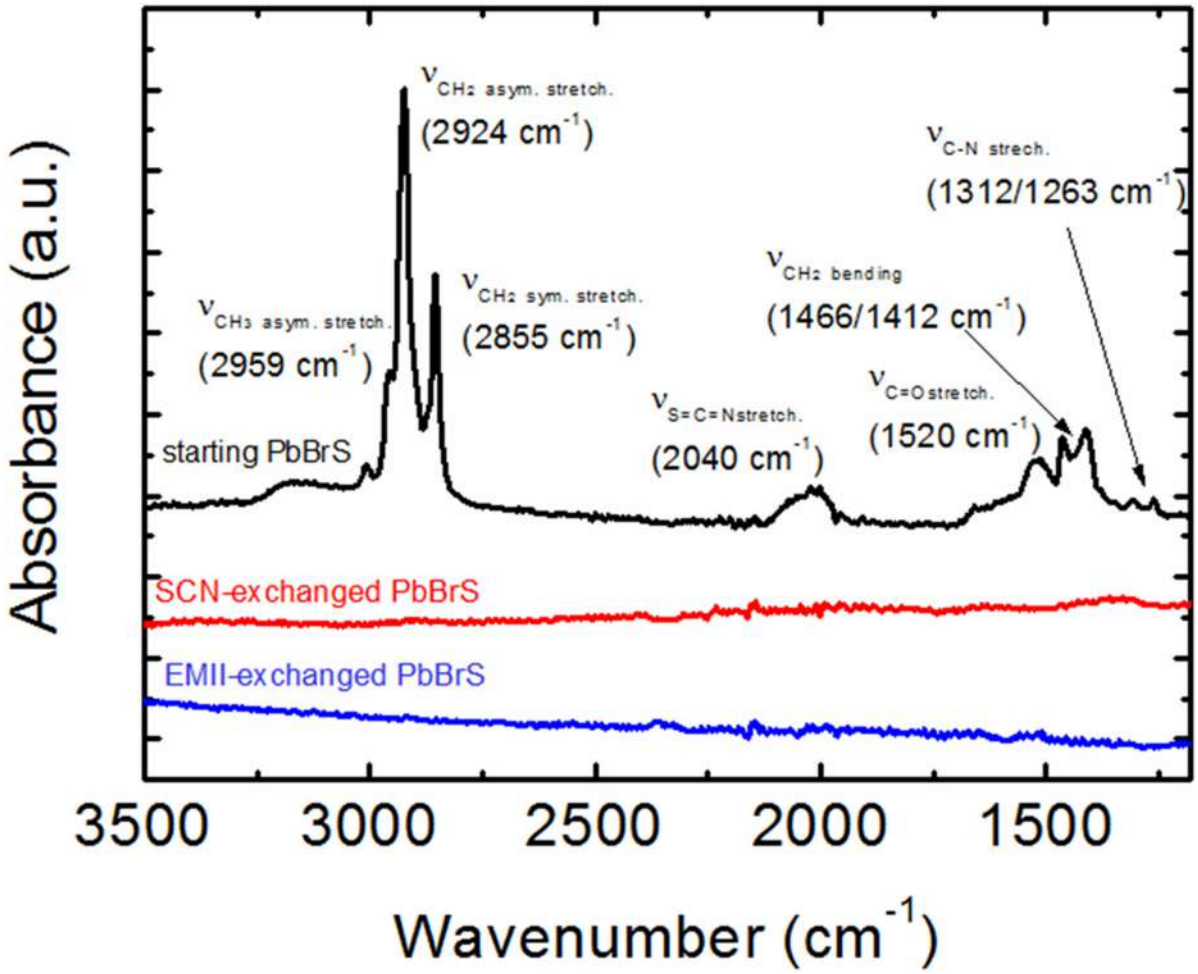

Figure S35. FTIR characterization of films of $Pb_4S_3Br_2$ NCs before and after ligand exchange. FTIR spectra of the as-synthesized $Pb_4S_3Br_2$ NCs, showing the characteristic signal of organic ligands (*black*) compared with that of NCs after being exchanged with SCN and EMII (*red, blue*). After the treatments, the original organic ligands have been quantitatively removed.

References

1. Akkerman, Q. A. *et al.* Ultrathin Orthorhombic PbS nanosheets. *Chem. Mater.* (2019) doi:10.1021/acs.chemmater.9b02914.
2. Wang, R. *et al.* PbI2 Nanosheets for Photodetectors via the Facile Cooling Thermal Supersaturation Solution Method. *J. Phys. Chem. C* **123**, 9609–9616 (2019).
3. Lin, D. Y., Guo, B. C., Dai, Z. Y., Lin, C. F. & Hsu, H. P. Pbi2 single crystal growth and its optical property study. *Crystals* **9**, 589 (2019).
4. Ni, D., Guo, S., Yang, Z. S., Powderly, K. M. & Cava, R. J. Pb 4 S 3 I 2 –A high-pressure phase in the PbS-PbI 2 system. *Solid State Sci.* **91**, 49–53 (2019).
5. Rabenau, A. & Rau, H. Über Sulfidhalogenide des Bleis und das Pb4SeBr6. *ZAAC - J. Inorg. Gen. Chem.* **369**, 295–305 (1969).
6. Ni, D., Guo, S., Powderly, K. M., Zhong, R. & Cava, R. J. A high-pressure phase with a non-centrosymmetric crystal structure in the PbSe–PbBr2 system. *J. Solid State Chem.* **280**, (2019).
7. NIST X-ray Photoelectron Spectroscopy (XPS) Database, Version 4.1. *National Institute of Standards and Technology, Gaithersburg* https://srdata.nist.gov/xps/ (2012).
8. Altomare, A. *et al.* EXPO2013: A kit of tools for phasing crystal structures from powder data. *J. Appl. Crystallogr.* **46**, 1231–1235 (2013).
9. Altomare, A. *et al.* Advances in powder diffraction pattern indexing: N-TREOR09. *J. Appl. Crystallogr.* **42**, 768–775 (2009).
10. de Wolff, P. M. A simplified criterion for the reliability of a powder pattern indexing. *J. Appl. Crystallogr.* **1**, 108–113 (1968).
11. Altomare, A. *et al.* Space-group determination from powder diffraction data: A probabilistic approach. *J. Appl. Crystallogr.* **37**, 957–966 (2004).
12. Altomare, A. *et al.* Space group determination: Improvements in EXPO2004. *J. Appl. Crystallogr.* **38**, 760–767 (2005).
13. Altomare, A. *et al.* Advances in space-group determination from powder diffraction data. *J. Appl. Crystallogr.* **40**, 743–748 (2007).
14. Le Bail, A., Duroy, H. & Fourquet, J. L. Ab-initio structure determination of LiSbWO6 by X-ray powder diffraction. *Mater. Res. Bull.* **23**, 447–452 (1988).
15. Altomare, A. *et al.* Solving Crystal Structures from Powder Data. I. The Role of the Prior Information in the Two-Stage Method. *J. Appl. Crystallogr.* **29 PART 6**, 667–673 (1996).
16. Altomare, A. *et al.* Solving Crystal Structures from Powder Data. IV. The Use of Patterson Information for Estimating the |F|'s. *J. Appl. Crystallogr.* **31**, 74–77 (1998).
17. Altomare, A., Cuocci, C., Giacovazzo, C., Giuseppina Moliterni, A. G. & Rizzi, R. Powder diffraction: The new automatic least-squares Fourier recycling procedure in EXPO2005. *J. Appl. Crystallogr.* **39**, 558–562 (2006).
18. Welch, P. D. The Use of Fast Fourier Transform for the Estimation of Power Spectra: A Method Based on Time Averaging Over Short, Modified Periodograms. *IEEE Trans. Audio Electroacoust.* **15**, 70–73 (1967).
19. Brown, P. R. *et al.* Energy level modification in lead sulfide quantum dot thin films through ligand exchange. *ACS Nano* **8**, 5863–5872 (2014).
20. Rastogi, P., Palazon, F., Prato, M., Di Stasio, F. & Krahne, R. Enhancing the Performance of CdSe/CdS Dot-in-Rod Light-Emitting Diodes via Surface Ligand Modification. *ACS Appl. Mater. Interfaces* **10**, 5665–5672 (2018).